SPATIAL AND TEMPORAL VARIANCE IN ROCK DOME EXFOLIATION AND WEATHERING NEAR TWAIN HARTE, CALIFORNIA, USA

by

Faye Lynn Moser

A thesis submitted to the faculty of
The University of North Carolina at Charlotte
in partial fulfillment of the requirements
for the degree of Master of Science in
Earth Science

Charlotte

2017

Approved by:

____
Dr. Martha Cary Eppes

____
Dr. Andy Bobyarchick

____
Dr. Brian Magi

©2017
Faye Lynn Moser
ALL RIGHTS RESERVED

ABSTRACT

FAYE LYNN MOSER. Spatial and temporal variance in rock dome exfoliation and weathering near Twain Harte, California, USA. (Under the direction of DR. MARTHA CARY EPPES).

Large-scale exfoliation cracks and associated domes can strongly influence regional landscape evolution, hydrology and hazards, but their formation mechanism(s) and long-term evolution are poorly understood. Beginning in August 2014, in Twain Harte, California, several rare, highly-rapid, exfoliation cracking events were observed and filmed, providing a unique opportunity to study the short (10^1 yr.)- and long (10^5 yr.)-term evolution of a rock dome. To do so, detailed mapping and morphologic and weathering characterization of exfoliation slabs was conducted at Twain Harte and 15 other nearby sites. In addition, previously collected data was analyzed at the Twain Harte site including the monitoring of cracking at the Twain Harte dome for 7 months using acoustic emission (AE) sensors, near-surface temperatures and light intensities at the same locations, and crack meters at the Twain Harte dome to measure post-event deformation. Mapping revealed 2-4 generations of exfoliation joints at all sites, manifested as stacked slabs with characteristic thicknesses of ~ 20 – 30 cm. Slabs exhibit statistically different weathering characteristics including compressive strength, crack length, and spalling height, with older slabs generally exhibiting greater degrees of weathering. Observed chronofunctions of weathering features provide evidence of a recurrence interval of slab formation that may be similar through time. Ongoing macroscale cracking appears limited to summer months suggesting a thermal trigger for observed events. Together, these data provide evidence of both spatial and temporal continuity in exfoliation processes, and could be used to test hypotheses of exfoliation slab and dome formation mechanisms.

ACKNOWLEDGEMENTS

This research project would not have been possible without the contributions of the following, for whom I am ceaselessly grateful.

- Dr. Martha Cary Eppes for, quite literally, everything. Without her guidance, intelligence and patience, none of this would have been possible in the first place.
- Drs. Andy Bobyarchick and Brian Magi for their valuable time in serving on my thesis committee.
- Dr. Brian Collins with the USGS and Dr. Greg Stock with the NPS for their tremendous contributions and co-authoring this research.
- The Geological Society of America for selecting this project to receive the Graduate Student Research Grant in 2015 and 2016, as well as the On to the Future Scholarship in 2016.
- Ephrum Asburry III Schwartz-Laubhann for her impossible helpfulness in field data collection and resilience through nightmares of me yelling numbers at her.
- Suzanne Ching for her tremendous patience in preliminary sensor data processing.
- The Sugar Pine RV Park in Twain Harte, California for accommodating a broke graduate student and her assistant for a whole month.
- The Twain Harte Lake Association for providing us unlimited access to The Rock.
- Dick and Ome Stark for their hospitable accommodations in Twain Harte for Dr. Eppes, Ephrum and me.
- Condor Earth Technologies, Inc. for their contributions to this research and their management of the repair of the Twain Harte Dam.
- My mom, Linda, because she’s always been supportive and is the best mom ever.

TABLE OF CONTENTS

LIST OF TABLES

LIST OF FIGURES

INTRODUCTION

Exfoliation domes and their associated surface-parallel exfoliation cracks (also known as sheeting joints or exfoliation joints) manifest all over the world (Figure 1). They influence landscape evolution, groundwater hydrology and hazard mitigation (review in Martel, 2006), yet the exact mechanism(s) and temporal evolution of their formation is still debated (e.g. Leith, 2014; Ziegler et al., 2013, 2014; Martel, 2006, 2011; Stock et al., 2012; Bahat et al., 1999). Overall, very little data exists regarding the morphology or rates of exfoliation in any locality, despite the fact that such data could provide key insight into the viability of these competing hypotheses.

Figure 1: **Examples of exfoliation domes worldwide.** A: Diamond Rock and Paarl Rock, South Africa. Photo by Dr. John Diemer, UNC Charlotte. B: Half Dome, Yosemite National Park, CA. Photo by David Iliff, License: CC-BY-SA 3.0. C: Corcovado Mountain, Rio de Janeiro, Brazil. Photo by Companhia da Escalada, <www.companhia daescalada.com.br>. D: Stone Mountain, GA, USA. Photo by Patricia Ann, <s-media-cache-ak0.pinimg.com/>.

In August 2014, in Twain Harte, California, a rare, highly rapid major exfoliation cracking event was filmed (Dotysan, 2014) (Figure 2). This event and subsequently documented cracking provide a unique opportunity to study the short (10 yr.)- and long (10^5 yr.)-term evolution from an exfoliation dome whose cracking timeline and characteristics are exactly known and well-documented.

Figure 2: **Stills from Twain Harte Rock exfoliation recording.** Stills from the 2014 YouTube video by username Dotysan. The full recording is available here: youtu.be/yAZ1V_DJKV8.

The exfoliation cracking events at Twain Harte also resulted in a dam fissure (Figure 3), of which the expense to repair cost the Twain Harte Lake Association approximately $900,000 (THLA, 2016). Similar dam structures exist throughout the Sierra Nevada range (California Division of Safety of Dams, 2015), therefore, such cracking has the potential to result in flooding, loss of tourism and economic revenue, erosion and deposition of sediment and reduction or contamination of drinking water supply. Understanding the morphology (e.g. depth of sheet joints as a function of dome geometry), evaluation and recurrence interval of exfoliation events such as that of Twain Harte presents an opportunity to provide critical data to inform dam failure mitigation and prediction.

Figure 3: **Image of Twain Harte dam rupture [2014].** From Condor Earth Technologies, Inc.

The objective of this study is to conduct a field- and sensor-based survey of cracking and dome weathering properties with respect to quantifying exfoliation periodicity and drivers at Twain Harte and other nearby comparable domes. Ultimately, the intent is to produce a comprehensive data set documenting age-proxy rock characteristics to better understand the mechanics of exfoliation. No other data set of this nature exists, and, thus, very little is known about exfoliation as a rock weathering process. Existing exfoliation hypotheses will be substantiated or eliminated based on the collected data to provide new insights into the morphology, evolution, spatial distribution and origins of exfoliation cracking and its associated landforms.

PREVIOUS STUDIES OF EXFOLIATION AND EXFOLIATION DOMES

The focus of this project is on rock domes, which are geologic landforms found worldwide (Figure 1). Per many introductory geology textbooks (i.e. Plummer et al., 2016; Tarbuck et al., 2016; Fossen, 2016; Jain, 2013), structural domes are symmetrical anticlines that dip in every direction away from a summit. For a landform to be a dome, it is necessary that the structure be round- or oval-shaped in map view and raised above the surrounding elevation. Their formation is typically attributed to overburden unloading and pressure release, which is discussed in more detail later in this section (Figure 4). It is important to understand that a specific type of geologic dome is known as an exfoliation dome, by which the rock erodes by surface-parallel cracking that detaches tabular sheets (a.k.a. slabs) from the overall rock body. These sheets are often compared to the layers of an onion, that can range in thickness from millimeters to meters (Jain, 2013). The breaks, or cracks, themselves are often referred to as exfoliation joints or sheeting joints, terms that will be used interchangeably throughout this paper.

The mechanics of exfoliation joints have been a long-debated and perplexing topic for geomorphologists. Gilbert (1904) presented initial observations of exfoliation domes in the Sierra Nevada region. He identified that exfoliation joints most commonly form subparallel to surfaces where topography is convex. He distinguished these sheet joints from other rock fractures due to their distinct curvature associated with specific landforms (i.e. domes). Gilbert (1904) attributed exfoliation joints to thermal events such as insolation or, especially, forest fires, where rapid expansion of the outermost surface relative to the cool interior of the rock might cause cracking. He named “weathering” as a secondary mechanism of production of exfoliation joints – processes that he differentiated from thermal weathering that includes chemical weathering, crystallization of material in rock fissures and frost-wedging. Further, Gilbert's third hypothesis comprised unloading from overburden – the temporal diminishing of compressive stresses causes granitic expansive stresses to become operative. All of these processes are identified by Gilbert as requiring further examination (as of 1904), and he does suggest that one is probably dominant, even though not enough data exists to make the selection of which.

One of the most referenced and extensive studies of sheet structure morphology and sheet joint mechanics was conducted by Holzhausen (1989). He defines exfoliation as:

> "[…] formed by thin cracks, or sheet fractures, that divide massive, relatively homogenous rock into lenses, plates or 'sheets' near the ground surface […] most widespread in granitic rock and gneisses […]"

Following a review of previous literature on similar joint studies, in addition to assessment of exfoliation joints (which he refers to as sheets) in three locations (Norway, California and Massachusetts), Holzhausen (1989) came to several comprehensive conclusions that have been drawn upon in many subsequent studies. In addition to providing a clear overall definition of exfoliation sheeting, other typical morphological features were identified, including:

1. Terminations (or endings) of fractures are gradational. Holzhausen (1989) observed the ends of fractures (in profile) would "feather out," gradually becoming less distinct until extinction.
2. Most exfoliation sheets are observably parallel to the orientations of microcracks. Granites have planes over which the rock may split or cleave more easily. The

review material in Holzhausen's 1989 paper provides observations of a strong correlation of the orientation of microcracks along these exfoliation planes. He interprets these planes as representing weaknesses in the rock mass, and therefore, the exfoliation joints also follow these planes and share a parallel orientation with microcracking.

3. The formation of new exfoliation sheets is still currently occurring. Holzhausen (1989) suggests the best evidence of ongoing fracturing is in granite quarries, with the spalling of thin slabs and sheeting observable near quarry floors.

Holzhausen (1989) also characterized the stresses of rocks displaying exfoliation joints, such as:

1. Most sheeted rocks are under high in-situ compression parallel to the surrounding topography. Holzhausen (1989) states that the observable quality of granites suggesting high compression are a manifestation of rockbursts and spontaneous expansions in quarries.
2. He hypothesized that such high differential stresses associated with surface-parallel compression is critical for exfoliation sheet formation.
3. The production of the essential stress needed for exfoliation could be from multiple sources, including tectonic forces, surface unloading and thermal fluctuations. These natural agents aid in the creation of the surface-parallel compression necessary to induce sheet fracturing. For example, he references the aforementioned work of Gilbert (1904) about unloading due to the removal of overburden.

More recent work has built on the foundational observations of Holzhausen (1989) and Gilbert (1904). The formation of exfoliation domes is most commonly attributed to unloading in virtually all introductory geology textbooks (i.e. Fossen, 2016; Jain, 2013), whereby previously-confined rock is exposed via uplift or overburden removal, causing pressures to release and the rock to expand (Figure 4). Leith et al. (2014) builds on this classically accepted mechanism for the formation of exfoliation joints and emphasizes the influence of the elastic response of exhumed bedrock with reduction of compressional stresses. For instance, if rapid unloading occurs (as in deglaciation), the removal of that load leads to surficial rebound. This rebound leads to an excess of the equilibrium microcrack initiation threshold and the formation and lengthening of fractures via subcritical crack growth (the slow, steady growth of fractures due to stresses lower in magnitude than that of their critical strength, as defined by parameters such as tensile strength or fracture toughness).

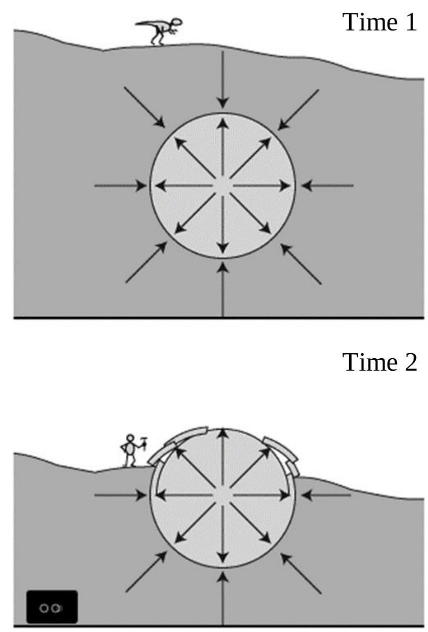

Figure 4: **Example of classical exfoliation dome formation processes.** Time 1: An intrusion lithifies in a pressure equilibrium state with surrounding bedrock. Time 2: Erosion exposes the intrusion and outward pressure exceed equilibrium state, causing exfoliation to occur. Photo source: www.geol.umd.edu/~jmerck/.

However, other recent research suggests that it is unclear if unloading is necessary for dome exfoliation. Martel (2006, 2011) proposes that exfoliation jointing can occur because of tectonic shortening of a curved surface without unloading. He analyzed exfoliation joint structures in the context of surface-parallel compression stress along curved surfaces, focusing on the influence of the geometry of the surface itself in producing the joints. In other words, he investigated how compressive stress combined with surface topography curvature results in the development of exfoliation joints. He rejects the widely accepted hypothesis that exfoliation joints are caused by erosion of overburden through observable inconsistencies, such as their absence in exhumed rock from great depths and their presence in rocks that were never deeply buried (Martel, 2011).

Using equilibrium equations, Martel quantitatively evaluated near-surface stresses. His model predicts that, in convex slopes, where the magnitude of curvature is largest, surface parallel fractures could form as long as compressive stress exceeds the static equilibrium (all forces equal) associated with the surface curvature (Martel, 2006). Martel (2011) studied the aspect, topography, curvature values (length and width) and in-situ compressive stress for nine different locations. He concluded that a rock mass that can build up sufficient tensile stresses to produce exfoliation joints must also be able to withstand high compressive stresses (Figure 5). This proposition explains the presence of exfoliation joints in strong rocks (i.e. granites, granodiorites) that are found in the Sierra Nevada region (Martel, 2006).

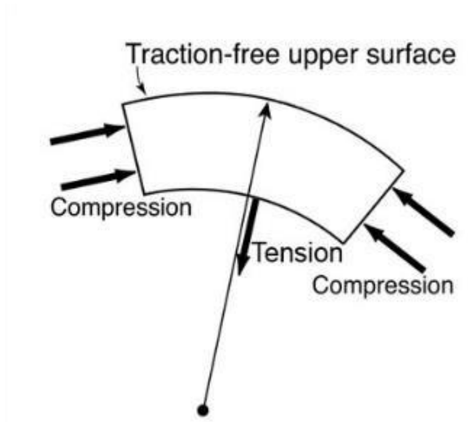

Figure 5: **Visualization of Martel's curvature jointing theory.** Per Martel (2011), if surface-parallel compression stresses exceed tension stresses, fractures can occur.

Building on Martel's geometric exfoliation work, a granitic cliff in Yosemite Valley, California was monitored for fifteen months to assess spatial and temporal patterns of rock fall sheeting (Stock et al., 2012). It was found that time-dependent mechanical weathering on rock faces (i.e. the subcritical growth of cracks) can lead to structural instability and failure. Although this study focuses on vertical cliffs, which have the added complexity of gravitational stress on the exfoliating slab, insights gained from these studies remain valuable for more "classical" domes. This is because their results suggest the geometry between exfoliation joints is a main mechanism to the concentration of stresses that drive exfoliation. This geometry is referred to by Stock et al. (2012) as "buckling," wherein orientations of intersecting microcrack fans lead to an internal separation of the exfoliation slab from the rest of the rock body. This relief of stresses causes the slab to "buckle" away from the surface because the ends of the slab remain intact or pinned (Figure 6) – creating a curved surface now experiencing similar stresses to that described by Martel (2011) in Figure 5.

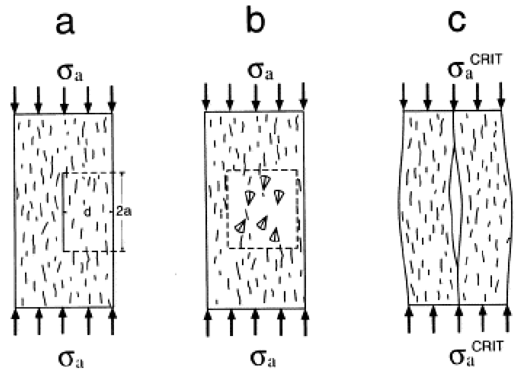

Figure 6: **Illustration of slab buckling mechanics per Stock et al. (2012).** a: Microfractures propagating from uniaxial applied stresses on rock. b: Microfractures coalesce into fans due to preferred orientations. c: Slab splits and buckles away from rock body.

To further understand the exfoliation mechanics of granitic rock in Yosemite National Park, Bahat (1998) analyzed fracture surface morphology including critical flaws, initial flaws, and fracture propagation. Findings of this study emphasized the significance of subcritical fracture influence in the exfoliation. The fracture process is identified as follows: if 1) sub-critical fracture growth occurs before overall sheet failure, then 2) fracture occurs to reduce overburden pressure and 3) sub-critical crack growth continues as the slab re-equilibrates. This was deduced from the analysis of two large, vertical granite faces that displayed a coalescence of exfoliation along planes where early microcracks were present. These cracks consist of vertical fans parallel to the cliffs –

similar to the microfracture parallelism observed by Holzhausen (1989) – and suggest the efficacy of low stresses for the development of microcracks in exfoliation settings (Bahat, 1998).

Regardless of the stress-inducing mechanism, there is consensus in the literature that large-scale exfoliation cracking is strongly influenced by small-scale subcritical crack growth (Leith et al., 2014; Holzhausen, 1989; Bahat, 1998; Stock et al., 2012). Eppes et al. (2016) and Warren et al. (2013) employ acoustic emission sensors to monitor the subcritical propagation of cracks on boulders and the relationship of those cracking events to thermal stresses. Acoustic emission data are collected in this context because they represent a sudden release of strain energy and, therefore, a cracking event. Results of monitoring this boulder resulted in an observable correlation between cracking events and temporal peaks in thermal cycles (i.e. mid-day and sunset; summer and winter) (Figure 7).

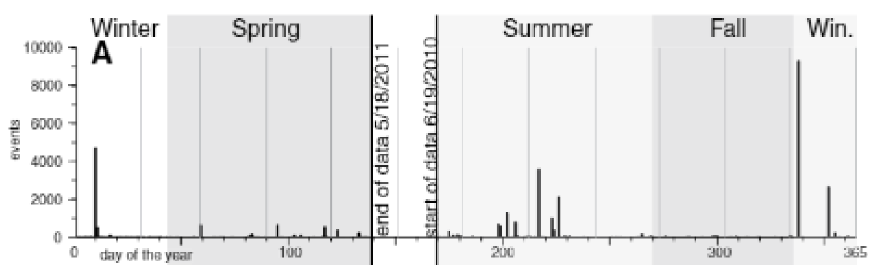

Figure 7: **Annual cracking activity trends.** From Eppes et al. (2016), cracking activity increases in summer and winter, which are annual temperature "extremes."

This relationship is also supported by the results of Collins and Stock (2016), who similarly attributed cliff face deformation and fracturing peaks, measured by crack meters, to be coincident with incoming solar radiation peaks (Figure 8). Collectively, these results support the hypothesis that background thermal-induced stresses contribute to cracking events, potentially regardless of the loading stress that ultimately triggers macro-fracture (Eppes et al., 2016). Acoustic emission techniques were also used in a study by Girard (2012) to monitor frost cracking, which assesses thermal freeze cycles and the effects of them on the deterioration of rock surfaces. It was found that both freezing and thawed conditions generated acoustic emission activity, and that rock expansion/contraction correlated to these acoustic emission "events" leads to fracture propagation (Girard, 2012). These thermal deformation studies suggest that exfoliation may be at least in part driven or influenced by subcritical crack growth due to thermal cycling.

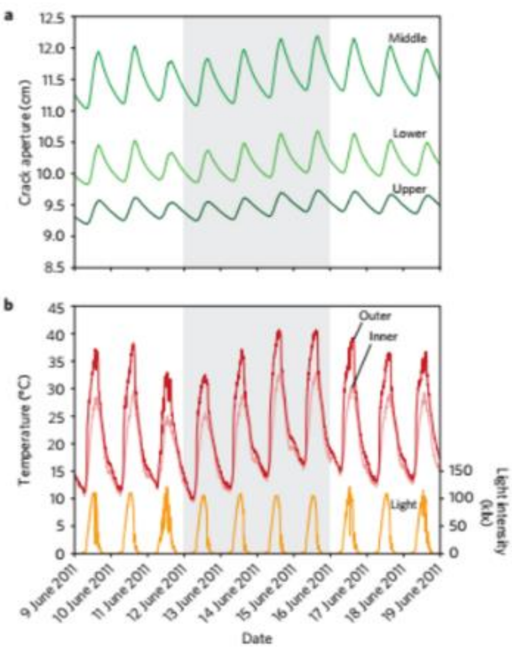

Figure 8: **Relationship between crack deformation and daily thermal cycling.** From Collins and Stock (2016), crack deformation activity (a) is fluctuating with temperature (b; red) and light (b; yellow) cycles.

Another possible contribution to the 2014 exfoliation at Twain Harte may be unloading driven by water table drawdown from the recent drought. In California, vertical motion of the Earth's surface is elastic response to additions and subtraction of water: it subsides with the loading of water/snow and uplifts when these loads are depleted (Argus et al., 2014). Borsa et al. (2014) and Argus et al. (2014) employed the use of global positioning system (GPS) stations to record surficial vertical displacement in the western United States. These data allowed for estimations of water mass loss, and indicated a median uplift of the region of 5 mm over 11 years. Comparatively, California's mountains have regionally experienced a median uplift of 15 mm during the same period A lowering of the water table as a product of the drought will induce sudden vertical and horizontal displacements from elastic deformation (Figure 9) that could be sufficient to produce exfoliation cracking. The results of this study showed a maximum vertical crustal displacement in the central Sierra Nevada equivalent to a fifty-centimeter water mass loss (Borsa et al., 2014). This rapid and substantial unloading of stresses from groundwater pumping and extreme drought may be a trigger for the observed exfoliation events at Twain Harte (Greg Stock, pers. comm.) following the model of Leith (2014). However, to date, no studies have related California's drought to the observed exfoliation events.

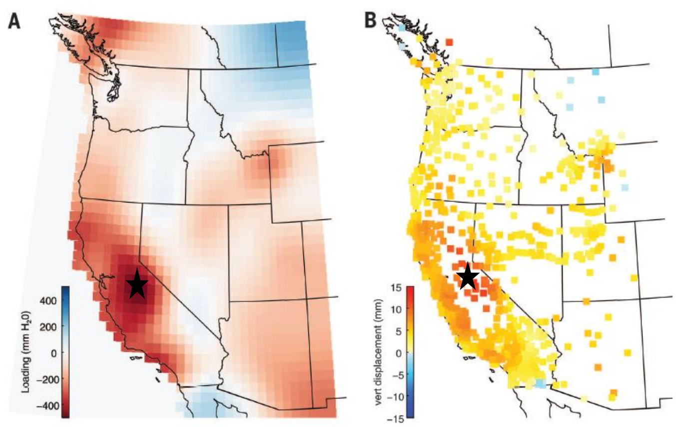

Figure 9: **Water mass loss and vertical displacement in the western US.** From Borsa (2014), A displays the water loading in millimeters, where red is deficit and blue is surplus. B displays the projected surficial displacement because of the water mass loss (as of 2014). Notice the approximate location of Twain Harte, the black star, in the most extreme location.

TESTABLE HYPOTHESES FROM PREVIOUS STUDIES

As is evident from a range of studies on exfoliation reviewed in the above sections (Gilbert, 1904; Holzhausen, 1989; Leith et al., 2014; Martel, 2005; Martel, 2011; Stock et al., 2012; Bahat, 1998; Eppes et al., 2016; Warren et al., 2013; Collins and Stock, 2016; Girard, 2012; Argus et al., 2012; Borsa et al., 2014), the driving factors that induce sheet joints and their associated exfoliation slabs are still ambiguous and require further investigation. Several untested predictions arise from existing models:

1. Dome curvature should correlate with exfoliation slab thickness (Martel, 2011).
2. Cracking rates over short timescales should decrease following an exfoliation event (Stock et al., 2012), but, over long (Quaternary) timescales, may be predictably periodic (Martel, 2005, 2011).
3. Crack deformation should occur coincidentally with annual and/or daily temperature cycling (Eppes et al., 2016; Collins and Stock, 2016).
4. If crustal unloading (via either deglaciation or water-table lowering) triggered cracking, other such events should be evident regionally.

Little (if any) data currently exists regarding the morphologic properties of exfoliation cracks – which could address some of these existing competing hypotheses (Wakasa et al., 2006). The purpose of this study is to collect, for the first time, detailed exfoliation slab morphology and relative age data that will be used to directly explore potential mechanistic links between exfoliation processes and their forcing mechanisms. For example, if measured exfoliation slabs are consistent in their thicknesses and recurrence through time, then the results would be at odds with unloading-related exfoliation triggered by glacial erosion, which should be reducing though time (Ziegler et al., 2013). Or, measured recurrence intervals that vary with time or in proportion to exfoliation slab thickness would imply forcing mechanisms that similarly changed in magnitude and/or timing (Wakasa et al., 2006), such as curvature-influenced tectonic stresses (Martel, 2006), or changing thermal stresses due to climate change (Eppes et al, 2016). Thus, through field-based observations of exfoliation slabs, this study will be providing some of the first documentation of the spatial and temporal evolution of sheet-joint cracking processes.

STUDY AREA

Twain Harte is in the western foothills of the Sierra Nevada geomorphic province in central California (38.0385° N, 120.2296° W) (Figure 10A). The town skirts the border of Stanislaus National Forest in Tuolumne County. The Sierra Nevada mountain range on the eastern face of this geomorphic province gives way westerly to gentle slopes, which can be seen in Figure 10B. Twain Harte is central to the transition from the high, rugged scarp to the western Great Valley province (CGS, 2002).

Figure 10: **Location of study area: Twain Harte, California, USA.**
A: Photo from Sperling's BestPlaces.
B: Google Earth image with geomorphic province boundary overlay (represented by bold black lines). Overlay from the California Geological Survey.

The exfoliation dome in Twain Harte is locally known as "The Rock," and is a focal point of the small town. Built into The Rock is a 99-meter multiple-arch dam with a recreational reservoir behind it (Figure 11). Twain Harte Lake is of constantly variable depths due to drought conditions (supplementary climate data available in Figure 12), but surface water usually covers

Figure 11: **Aerial drone photo of Twain Harte Rock, Dam, and Lake.** From a drone video created by Craig Mullins. www.youtube.com/watch?v=_E-uARaWa9M

about 12 acres and the lake has a maximum capacity of 176,000 cubic meters (THLA, 2016).

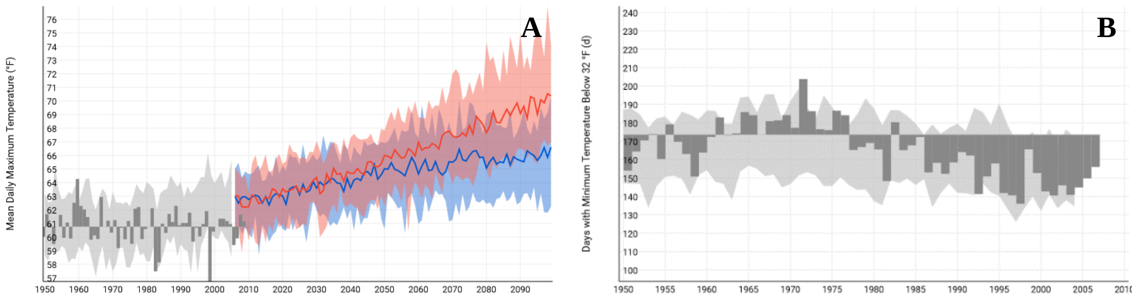

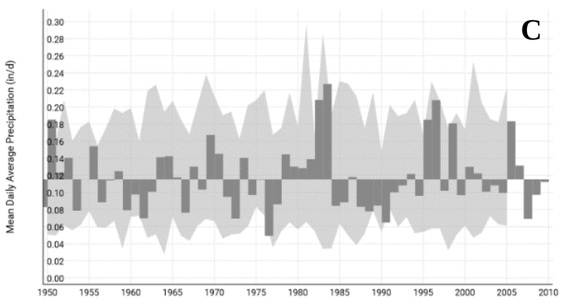

Figure 12: **Tuolumne County climate data annual averages – 1950 – 2004.** Graphs generated by the U.S. Climate Resilience Toolkit (toolkit.climate.gov). Grey bars are measured seasonal averages surrounded by the grey shading – which is what the climate model projection was at the time. A: Mean daily maximum temperature. Blue is projected temperature if global emissions do not change. Red is projected temperature if global emissions increase. B: Number of days below freezing, annual averages. C: Daily precipitation, annual averages.

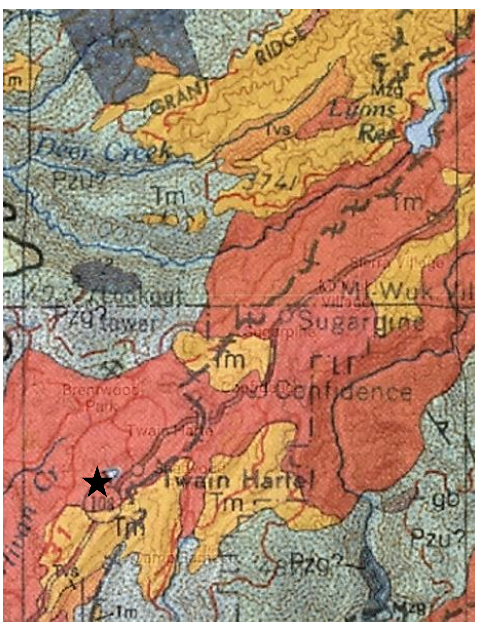

Figure 13: **Expanded view of Twain Harte area bedrock geology.** From the 1981 California Geological Survey's 1:250,000 map of the Sacramento area. The full map is available in Appendix A. The location of Twain Harte Rock is indicated by the black star.

Per the California Geological Survey's 1981 Geologic Map of the Sacramento Quadrangle (see Appendix A for complete map), the country rock around Twain Harte is an interfingering of three similar rock types. The primary bedrock is Mesozoic age granite or diorite (red units in Figure 13) – both "silicate-rich igneous intrusive basement rock" (Shlemon et al., 2000). The other unit present (orange unit in Figure 13) is the Pliocene/Miocene age Mehrten Formation – a "sandstone, laminated siltstone, conglomerate, and tuff breccia composed almost entirely of andesitic material" (Shlemon et al., 2000). The composition of Twain Harte Rock and other regionally mapped domes were consistently of the granodioritic unit.

Given the potential importance of compressional stresses in leading to the formation of the Twain Harte exfoliation (e.g. Martel, 2006, 2011), it is important to understand the regional tectonic stresses around Twain Harte to begin to interpret exfoliation stress environments. Based on the 2016 World Stress Map database, which is a "global compilation of information on the crustal present-day stress field" (Heidbach et al., 2016), the immediate region of Twain Harte is not experiencing any *documented* crustal stresses (Figure 14). That is, within the scale of the region as defined by this project – within 10^2 km

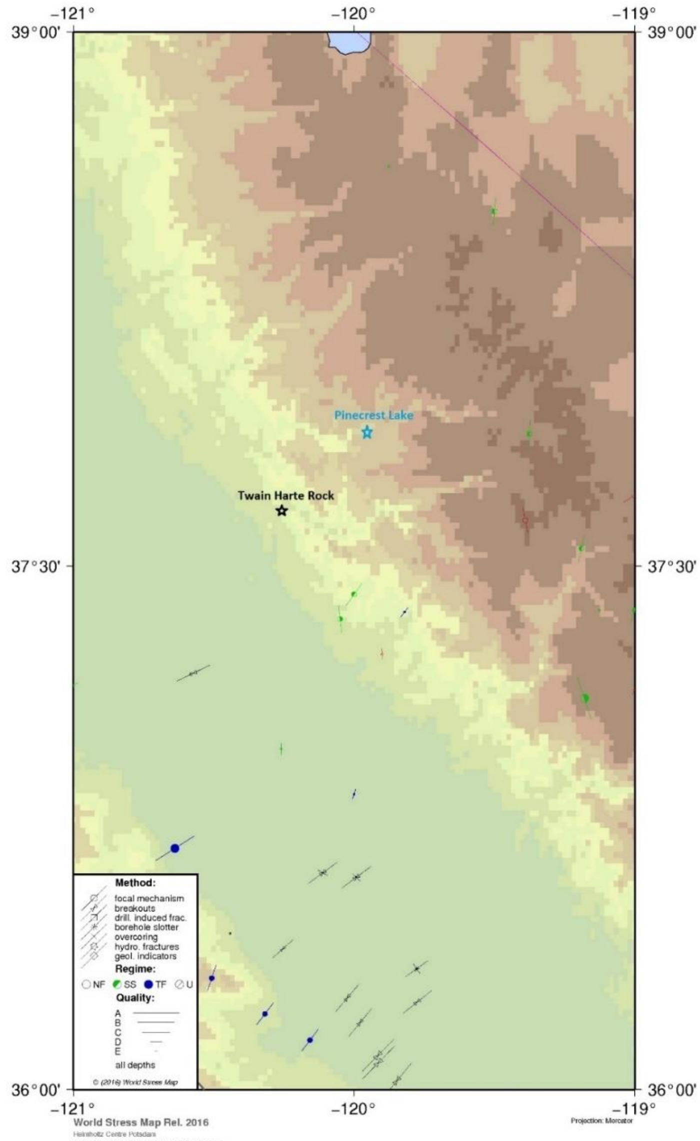

Figure 14: **Documented crustal stresses compiled by the World Stress Map Database.** This data was pulled from the latest iteration of the database (2016). As can be seen, there is no documented crustal stress information for the study area. The closest documented stresses are 1970s earthquake foci 60 km to the south (in the green).

of Twain Harte Rock, and three additional sites 40 km to the northeast around Pinecrest Lake. The closest measured tectonic stresses are approximately 60-100 km away from the study area – and show a range of motion (compression and shear). The absence of any crustal stress is highly unlikely, however, the lack of pertinent stress map data near the subject precludes drawing sound conclusions.

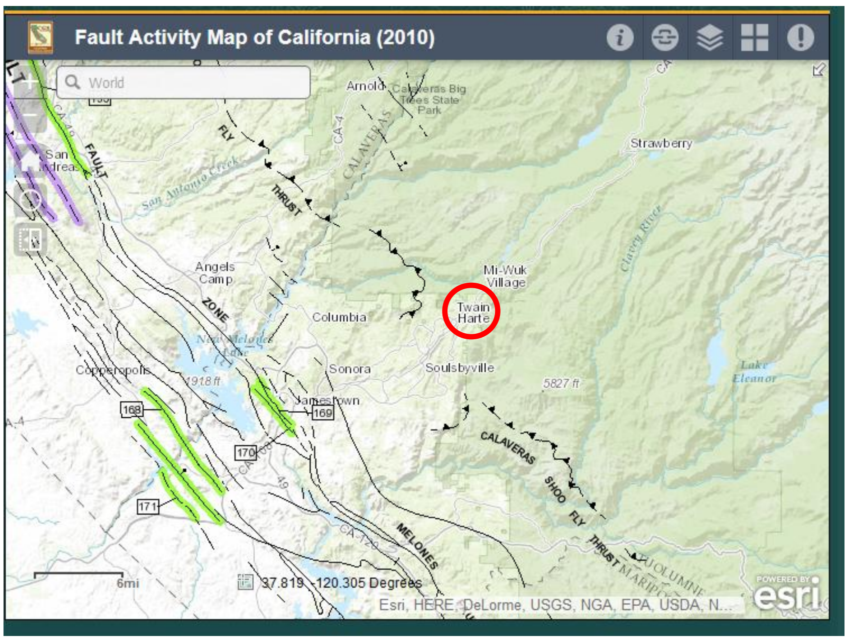

Figure 15: **California Geological Survey's Fault Activity Map of the Twain Harte, CA region.** Zoomed out so that it is possible to observe the behavior of the Calaveras-Shoo Fly Thrust, and its absence from the study area. Most likely, this thrust zone does not have crustal stress effects on Twain Harte Rock and the other nearby study sites. The red circle indicates the location of Twain Harte. The green lines are Late Quaternary fault displacements (during the past 700,000 years) and the purple lines are Quaternary faults of undifferentiated age.

The California Geological Survey's 2010 Fault Activity Map (Figure 15) was also consulted to quantify any tectonic stress around Twain Harte. It was discovered that Calaveras-Shoo Fly Thrust Fault passes near Twain Harte, but not through. Upon further research into this crosscutting of the fault, a map was found in the 1985 dissertation of Charles Merguerian showing that Twain Harte is positioned on the eastern side of the Standard Pluton, which forcefully intruded into this thrust zone and overturned the Calaveras-Shoo Fly Thrust in the Middle-Jurassic (Figure 16). This geologic history of the thrust deformation shows that the thrust has not been active since before it was truncated by the Standard Pluton, and therefore likely does not contribute to a quantifiable tectonic stress that can be used in the surface curvature models of Martel (2006, 2011).

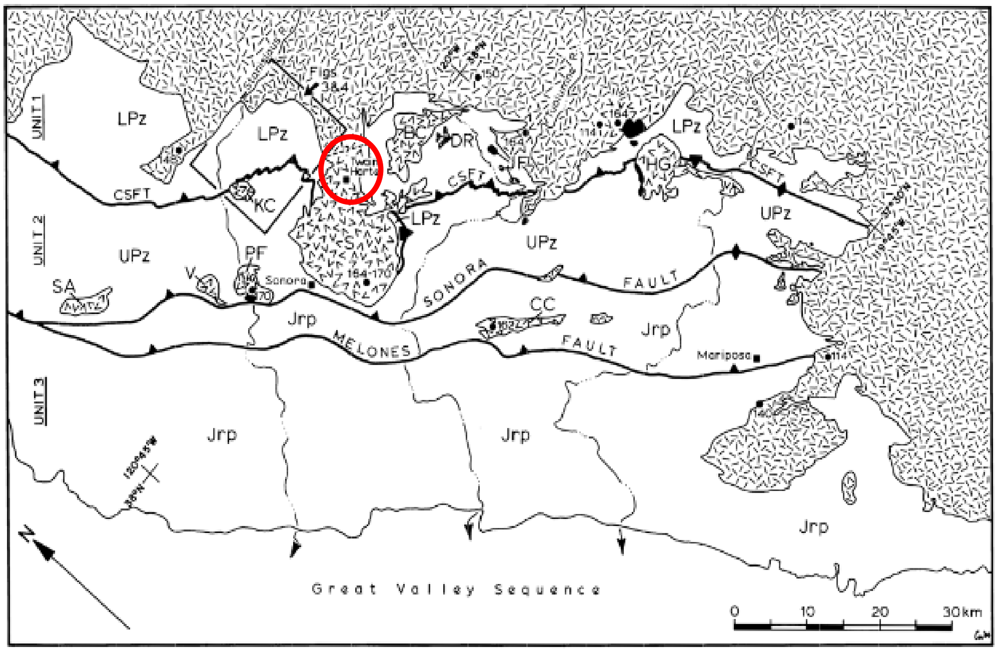

Figure 16: **"Geologic map of the southern end of the foothills metamorphic belt in Calaveras, Tuolumne, and Mariposa Counties, California" from Merguerian, 1985.** The red circle indicates the location of Twain Harte on the Standard Pluton.

METHODS

Overview

When conducting a preliminary field assessment of The Rock's surface, it became apparent that there were multiple layers of exfoliation. These manifested as stratigraphically differentiated slabs (colored boundaries in Figure 17), whose characteristics became of key interest to this study.

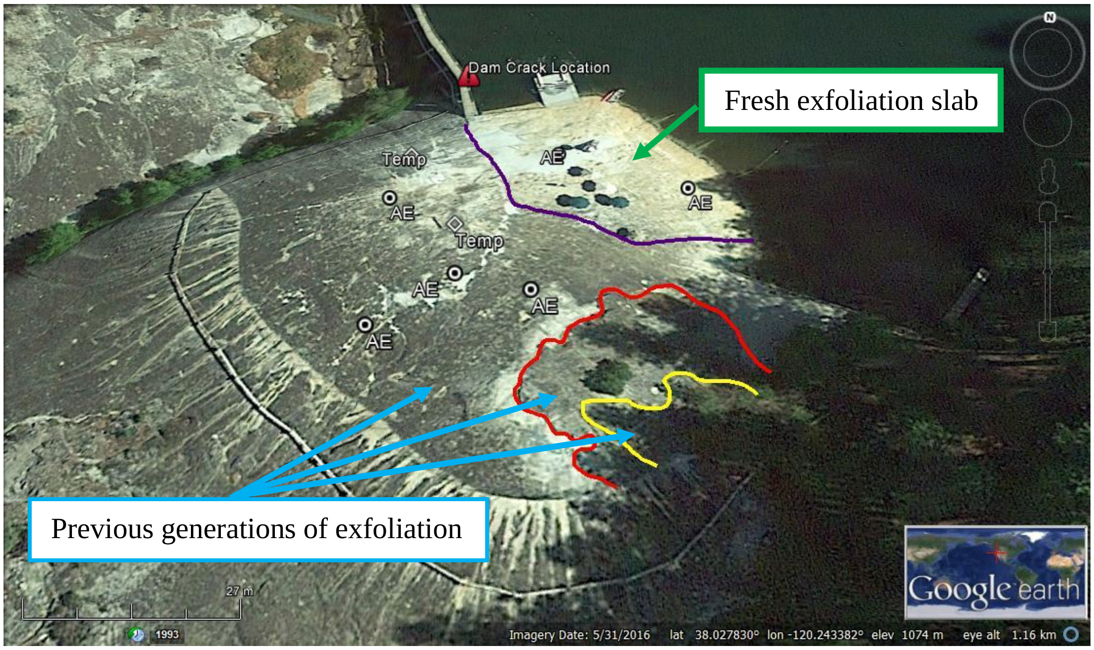

Figure 17: **Twain Harte Rock: Preliminary surficial assessment and sensor locations.** This figure displays the locations of the six acoustic emission sensors, temperature sensors, and the four identifiable exfoliation slab boundaries. Also, displays relative dam fissure location. Image generated in Google Earth.

These preliminary discoveries prompted a formulation of research questions and methodology necessary to address the existing hypotheses mentioned on page 13 of this document.

1) What are 'typical' exfoliation slab and cracking characteristics and do they change through time and space? This question is relevant in the context of short-term evolution (10^{-1} yr.) of cracking that has occurred since the Twain

Harte exfoliation event, as well as in the context of long-term evolution (10^5 yr.) via examination of the visible generations of exfoliation.

2) Are similar exfoliation events occurring regionally? If so, are the characteristics of domes/slabs consistent with others in the area?

To address these questions, observable characteristics were collected from each of the stratigraphically manifested exfoliation slabs. In addition to slab morphology, slab weathering characteristics were also observed as a proxy for relative age, because the degree of rock weathering increases with exposure age (e.g. Birkeland, 1999). These weathering and slab morphology characteristics were then employed to understand the spatial and temporal evolution of exfoliation in and around Twain Harte.

Field Methods

The first portion of this study identified other domes around Twain Harte that exhibited similar characteristics to that of Twain Harte Rock – primarily via the granodioritic composition and the apparent presence of the stacked exfoliation slabs. After field reconnaissance, access was gained to fifteen other sites on exfoliation domes in the region (Figure 18). The domes were centralized around Twain Harte Rock (Figure 18A) and Pinecrest Lake, to the northeast (Figure 18B). Each site was assigned a respective number for identification purposes.

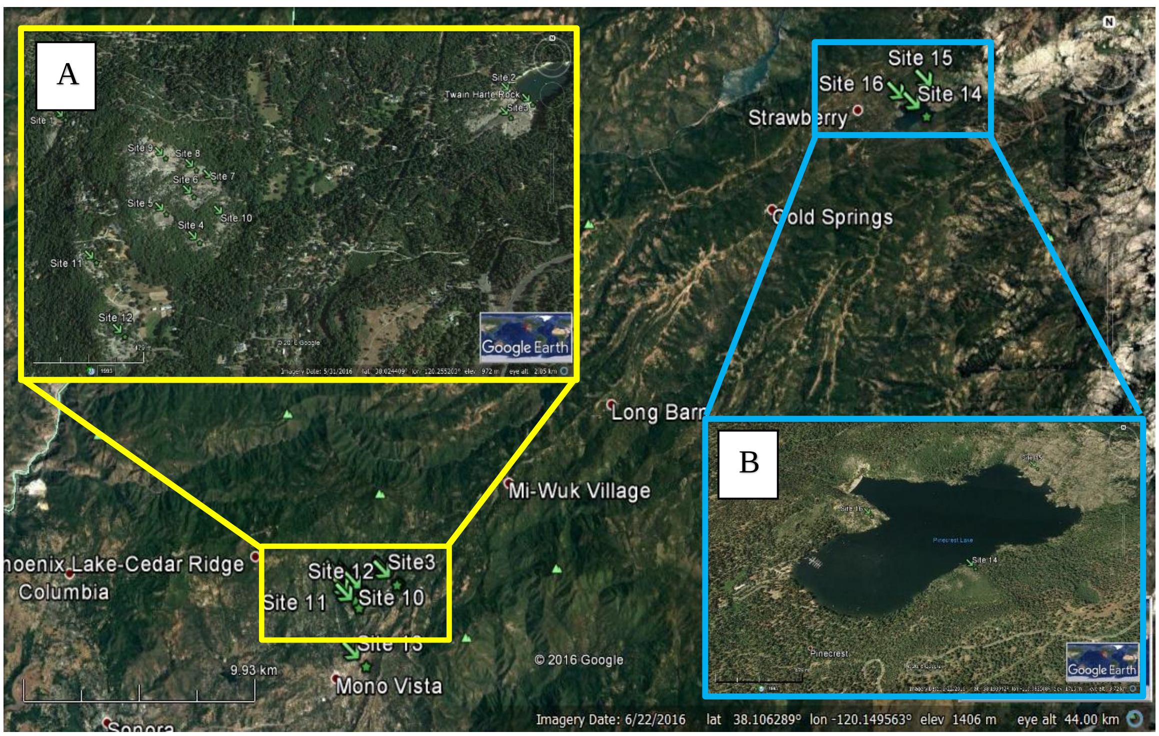

Figure 18: **Site locations around study area.** A: Zoom in locations in the Twain Harte area. B: Zoomed in locations in the Pinecrest Lake area. Images generated in Google Earth.

Detailed topographic surveying and slab mapping was conducted at each of the 15 sites (Appendix B). To capture the overall surface topography and relative exfoliation slab stratigraphic relationships, two perpendicular transects were made across each site.

Transects were not always perfectly perpendicular, because steep topography or adjacency to cliff faces made data collection difficult or hazardous (particularly at Sites 14 and 15). Topographic profiles were mapped in the field by recording the distance between two points where a change in slope was observed, then recording the vertical change using a Brunton compass inclinometer. The latter was executed by spotting a predetermined eye-level point between the person with the compass and another person standing at the point where a slope change occurred. Appendix C is a compilation of all the collected dome topographic profiles.

The following general observations of slab surfaces were also made for each mapped exfoliation slab at each site:

- Surface lichen percent coverage was estimated using the "Comparison Chart for Estimating Percentage Composition" from Terry and Chilingar (1955).
- Percent vegetation coverage was similarly quantified with the Terry and Chilingar (1955) method, and attempts were made to divide that percentage into types (i.e. grasses, shrubs, trees).
- If a preferred surface orientation was apparent, the facing aspect of the slab was collected using a Brunton compass.
- Overall surface relief range was estimated by identifying the average vertical difference between depressions and elevations on the surface.
- A minimum of three surface slope measurements were collected using a Brunton compass inclinometer. Each slope measurement was accompanied by a slab thickness measurement whenever possible.

- Utilizing the Terry and Chilingar (1955) method once again, an estimation was made of the surface percentage that displayed granular disintegration – where grains have become loose from the solid rock surface.
- A scale was developed to quantify the presence of spalls on the surface of the slab. A spall is an onion-like exfoliation sheet feature, like the slabs, but on a smaller scale (Figure 19). This scale categorized spalls into length buckets (fine (F; 1 – 10 cm), medium (M; 10 – 30 cm), coarse (C; 30+ cm)) and designated a number system to estimate their density in a representative ½ x ½ meter square. The scale was weighted to account for the fact that coarse spalls covered more surface area than fine spalls, even though fine spalls were more predominant (Table 1). For example, one coarse spall (over 30 cm long) may cover the same surface area as three fine spalls (1 to 10 cm long each).
- A semi-quantitative index was developed to characterize the morphology of surface dissection of each slab (0 – 4, see Figure 20) and to quantify its density (A: rare, B: occasional, C: abundant).

Table 1: **Spalling density estimation method**

ID	*QUANTITY OF SPALLS IN SQUARE*		
	Fine Spall (1 – 10 cm)	*Medium Spall (10 – 30 cm)*	*Coarse Spall (30+ cm)*
0	None	None	None
1	1 – 4	1 – 2	1
2	5 – 10	3 – 4	2
3	> 10	> 4	> 2

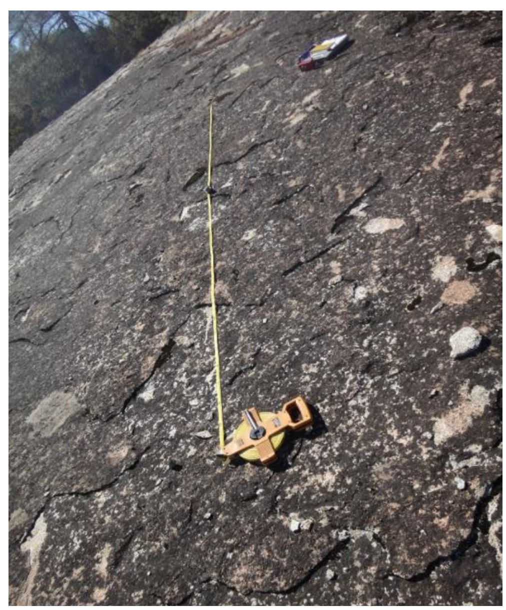

Figure 19: **Example of spalls from Site #5.**
Photo by Ephrum Schwartz-Laubhann, 2015.

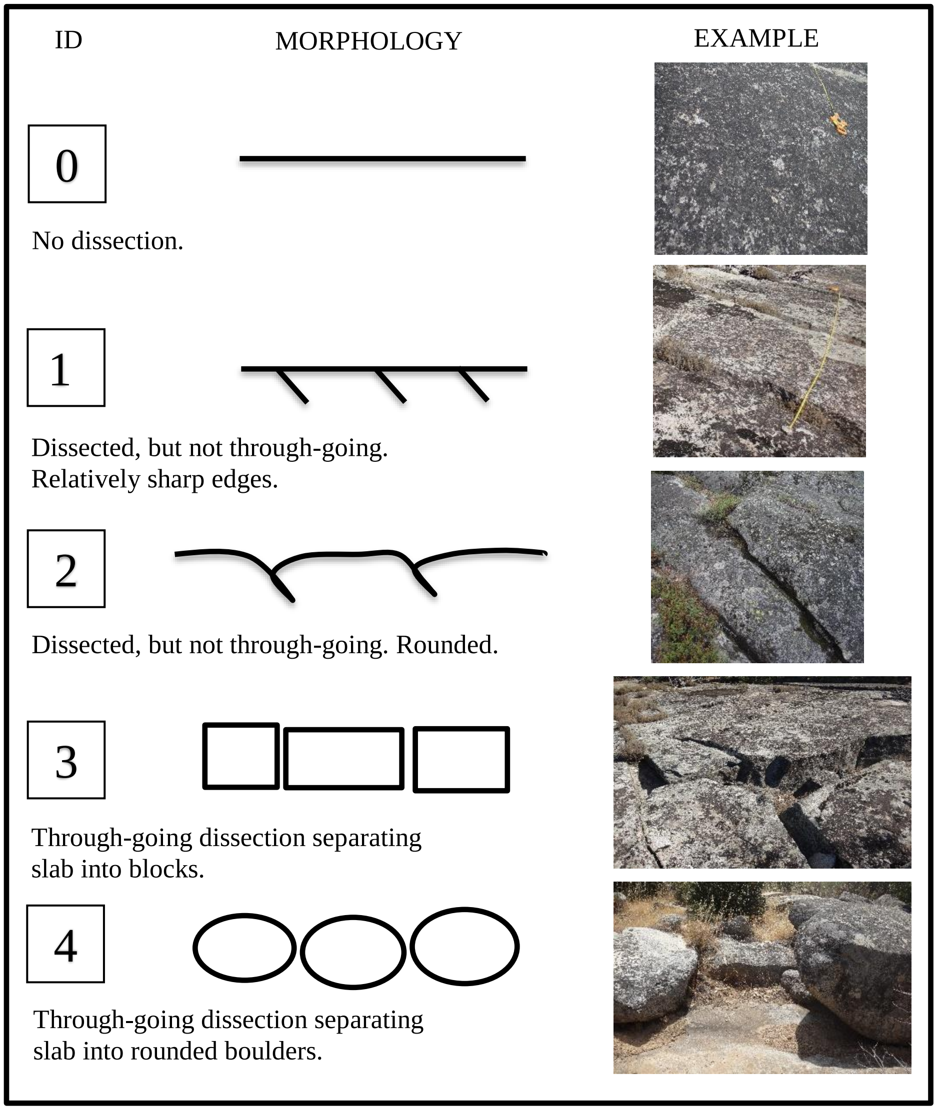

Figure 20: **Depiction of dissection scale.** A semi-quantitate index to document slab dissection. All photos by Ephrum Schwartz-Laubhann, 2015.

Occasionally, designated slabs would manifest in multiple locations at the same site, in which case this entire data set would be collected in both places (i.e. Slab 3A and Slab 3B).

Using a random stratified sampling scheme, another transect was positioned on each slab at eight of the sixteen sites. These transects were of variable lengths and meant to be representative of all observed morphological features on the slab (example in Figure 21). The intent here was to collect data pertaining to slab surface microtopography and characteristics of every linear void greater than two centimeters long (see Appendix D for a sample field data sheet). Each slab at the eight sites had one of these transects, for which the following was collected.

Figure 21: **Example of a micro-topography slab transect.** This transect is located along “Slab 2” on Twain Harte Rock. Generated in Google Earth.

- A directional bearing of the transect using a Brunton compass.
- Microtopography along the transect by:
    1. Identifying where slope changes occurred.
    2. Placing a flat object on the surface of the slab between each point where slope changes.
    3. Collecting the strike and dip of the flat object using the right-hand-rule method and Brunton compass as a proxy for the surface.
- For every linear void greater than two centimeters in length (henceforth referred to as a crack), a consecutive numerical identifier was assigned. The subsequent characteristics were evaluated for each crack.

1. The distance from the start of the transect that the crack intersected the tape measure identifying the transect position.
2. A general assessment of crack geometry relative to the rock surface. Cracks could be assigned as parallel to the surface (S), parallel to the rock fabric (F) (i.e. joints, bedding), parallel to some other rock feature (O), or parallel to none of these.
3. A measurement of the total length of the crack, end to end, until the crack tips were no longer visible. Crack length is defined as the length of the long side of the plane defining the crack. Seamstress tape was used along the entire exposed length of each crack to collect this measurement.
4. If present, a measurement of “crack height” (also referred to in this document as spalling thickness/height), which would be the difference between the heights of the rock surfaces on either side of the crack. This measurement was collected using digital calipers.
5. Whenever possible, a strike and dip measurement of the void. To collect this, a flat surface was used to project the crack orientation plane, which was subsequently measured using a Brunton compass with the right-hand-rule method.
6. If the crack was adjacent to an exposed edge face, the aspect of that edge was collected using a Brunton compass (similar to the strike of a cliff face).
7. In the immediate of the vicinity of the crack, it was noted whether granular disintegration, micro-spalls, and/or micro-cracks (less than two centimeters in length) were present.

8. A weathering index was assigned to each crack to approximate the overall extent of weathering. This weathering index scale is as follows (and is illustrated in Appendix H):
   - 0: fresh crack, no signs of oxidation or weathering.
   - 1: fresh crack with less than 50% of the face oxidized.
   - 2: fresh crack with greater than 50% of the face oxidized.
   - 3: sharp-edged crack, fully oxidized.
   - 4: round-edged crack, fully oxidized.
   - 5: round-edged crack, sealed (i.e. lichen, loose sediment).
   - 6: no void present, but obvious paleo-crack location. Identified via a drastic change in surface relief.

Further, a minimum of 100 Schmidt hammer rebound (R) values were collected equidistantly along each micro-topographic transect to measure rock strength, no more than ten centimeters to the right or left of the transect tape. The Schmidt hammer is a non-intrusive tool that measures compressive strength by quantifying the rebound of a spring-loaded hammer off a surface (Figure 22). Many previous geomorphological studies have utilized the Schmidt hammer R-value as a relative

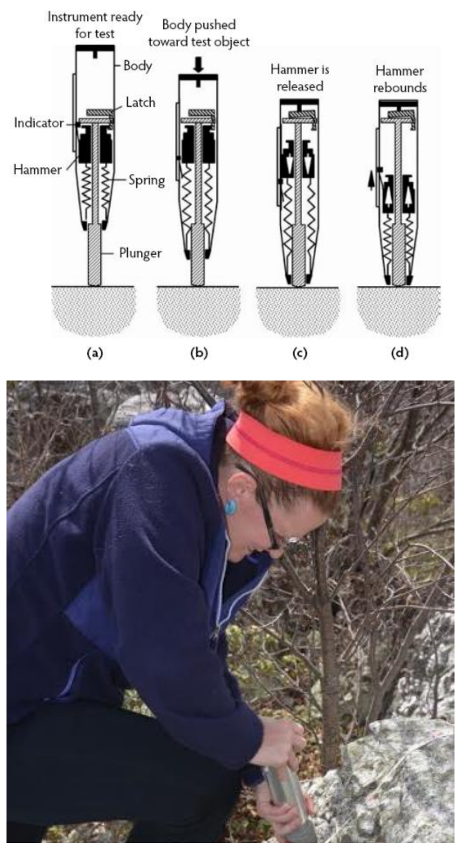

Figure 22: **Schmidt hammer schematic and field testing use.** Schmidt hammer schematic image from Nawry, Edward G. Concrete Construction Engineering Handbook, 2nd edition. Photo of field testing with the Schmidt hammer by Dr. Martha Cary Eppes, 2015.

age-dating technique (reviewed in Moses et al., 2014 – Table 2), because rock strength decreases as weathering influences increase. As that Schmidt hammer readings are negatively affected by increased surface roughness (Moses et al., 2014), it was necessary to collect readings from relatively smooth areas of the surface, which may have introduced some sampling bias. An approximate total of 5500 R-values were collected from the exfoliation slabs.

Additionally, a fist-sized rock hand sample was collected from each slab where micro-transect data were collected. These samples were dislodged using a rock hammer, and were collected no closer than fifty centimeters to any slab edge, to have the most representative sample of in situ weathering and avoid accelerated weathering properties characteristic of rock edges. The hand samples from all slabs at four sites were subsequently mailed to National Petrographic Service, Inc. to be prepared as thin sections for future petrographic analysis. Blue epoxy was added to the samples to highlight micro-porosity. Orientation was retained using a notching system to indicate which direction on the thin section was stratigraphic “up.” While not included in this analysis, future work will analyze the thin sections for the total proportion of minerals (quartz, plagioclase feldspar, orthoclase feldspar, micas, chlorite and amphibole), whether or not those minerals appeared to have experienced alteration and pore space.

Sensor and Meter Methods

Following the 2014 exfoliation events at Twain Harte, six acoustic emission (AE) sensors and two temperature sensors were deployed by Dr. Martha Cary Eppes to monitor rock surface activity (approximate locations mapped in Figure 17). These sensors continuously recorded data for seven consecutive months, except for instances of equipment failure or people disturbing the surface. These time spans are not included in the analysis herein. The AE sensors (PK151, manufactured by Physical Acoustics Corporation) were employed to monitor cracking activity, as in previous rock fracture experimentation by Warren et al. (2013), Girard et al. (2013), and Eppes et al. (2016). AE sensors serve to detect elastic waves that are generated by a release of strain energy in a solid material. As reviewed by Eppes et al. (2016), thorough laboratory research has been conducted on AE detection as a proxy for crack propagation in brittle materials, including rock. Near-surface temperatures and light intensity sensors (HOBO Pendant ® Temperature/Light Data Loggers) were also deployed by Drs. Gregory Stock (National Park Service) and Brian Collins (United States Geological Survey) on the dome for the same time span.

Finally, post-event deformation was monitored using a deployment of crack meters and subsurface extensometer instrumentation installed under the freshly exfoliated slab by Drs. Stock and Collins. The crack meter data was utilized herein as a proxy for crack opening to compare to the other sensor data, including temperature, light and acoustic emission hits.

RESULTS

Detailed mapping of all sites revealed two to four generations of exfoliation, manifested as stratigraphically stacked slabs with distinctly different degrees of weathering. As a convention, numerical identifiers were assigned to these slabs observed in the field (Figure 23), where the lowest slab is “1”, etc. It was clear that these slabs demarcated exfoliation events that had occurred and broken away part of the dome.

Figure 23: **Example field observation of slab stratigraphic differentiation.** Numbers are an example of the slab identifiers. Photo by Ephrum Schwartz-Laubhann, 2015.

Twain Harte Rock and adjacent sites on the same dome were the only sites to exhibit four generations of exfoliation slabs. This was due to the presence of the lowest slab exposed by the 2014 cracking event. The majority (nearly 70%) of all other sites had three generations of slabs (Figure 24). 12% of the sites only had two, from which the data was not included in the following analysis due to the ambiguity of slab identification. There was no immediate way to know how the age of those slabs at other sites related to the four generations at Twain Harte.

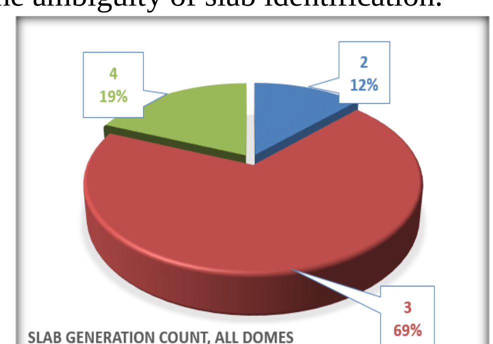

Figure 24: **Slab generation distribution.**

Section 1: Summary statistics across all slabs

A standard statistical analysis was completed for the general slab surface characteristics, including Schmidt hammer rebound values, observed for all mapped slabs (Table 2). A more detailed analysis of the Schmidt hammer data can be found in subsection 1D.

Table 2: **Statistics calculated for general observations of all slabs at all sites.**

	N	*Mean*	*Std Dev*	*Min*	*Max*
Lichen (%)	58	61.6	31.7	0	100
Vegetation (%)	58	9.7	16.2	0	80
Granular Disintegration (%)	58	23.9	31.7	0	90
Relief (cm)	58	4.9	4.1	1	20
Slope (◦)	58	16.3	7.5	2.7	45
Schmidt (R)	58	28.8	8.8	13.9	55.3
Thickness (cm)	41	31.4	28.4	7.2	110.2

A multivariate correlation was compiled in JMP ® 10 software to quantify the relationships between these different variables for each slab. Table 3 is a summary of the computed strength of linear relationships between two variables by evaluating the Pearson correlation coefficient (r) using the following equation:

Equation 1: **Pearson correlation coefficient (*r*)**

$$r = \frac{\sum (x-x)(y-y)}{\sqrt{\sum (x-\bar{x})^2}\sqrt{\sum (y-\bar{y})^2}}$$

If the linear relationship is exactly 1:1, the *r* value is either 1 (positively correlated) or -1 (negatively correlated). If no correlation exists, the *r* value will be closer to 0. Relationships will be considered significant with r values between -0.9 - -0.5 and 0.5 – 0.9.

Table 3: **Pearson correlation coefficient ® values for general slab surface characteristics.** Positively correlated *r* values are in blue gradient scale and negatively correlated values are in red – with color intensity increasing with correlation strength.

	Slab #	Lichen (%)	Vegetation (%)	Granular Distintigration (%)	Relief (cm)	Aspect (°)	Slope (°)	Schmidt (R)	Thickness (cm)
Slab #	1.0000	0.2836	0.4438	0.6290	0.0773	0.0314	-0.1436	-0.8141	0.2192
Lichen (%)	0.2836	1.0000	0.0231	0.1040	-0.0809	0.0792	-0.1698	-0.3160	0.2136
Vegetation (%)	0.4438	0.0231	1.0000	0.4737	0.0871	-0.1030	-0.0168	-0.4540	0.0506
Granular Distintigration (%)	0.6290	0.1040	0.4737	1.0000	0.1464	0.0658	-0.2007	-0.7373	-0.0433
Relief (cm)	0.0773	-0.0809	0.0871	0.1464	1.0000	0.1266	-0.2556	-0.1077	0.3675
Aspect (°)	0.0314	0.0792	-0.1030	0.0658	0.1266	1.0000	-0.2739	-0.0729	0.0965
Slope (°)	-0.1436	-0.1698	-0.0168	-0.2007	-0.2556	-0.2739	1.0000	0.1540	0.0751
Schmidt (R)	-0.8141	-0.3160	-0.4540	-0.7373	-0.1077	-0.0729	0.1540	1.0000	-0.2380
Thickness (cm)	0.2192	0.2136	0.0506	-0.0433	0.3675	0.0965	0.0751	-0.2380	1.0000

1A: Vegetation

In-field vegetation identification was limited to simple categorical buckets. Observed vegetation types included mosses, grasses, shrubs (young and mature), ferns, succulents, and trees (young and mature). As can be seen in Table 3, percent vegetation coverage has a positive correlation with slab number (i.e. Slab 4 would have the highest percentage of coverage). Slab 1 at all sites did not possess any vegetation. Slab 2 had vegetation coverage between 5 – 10% at only three sites that included primarily grasses and succulents, with one anomalous site having 5% mature tree coverage. Vegetation percentage and variability increased significantly for Slab 3 and Slab 4 at all sites (Figure 25), with grasses and mature shrubs being the dominant type.

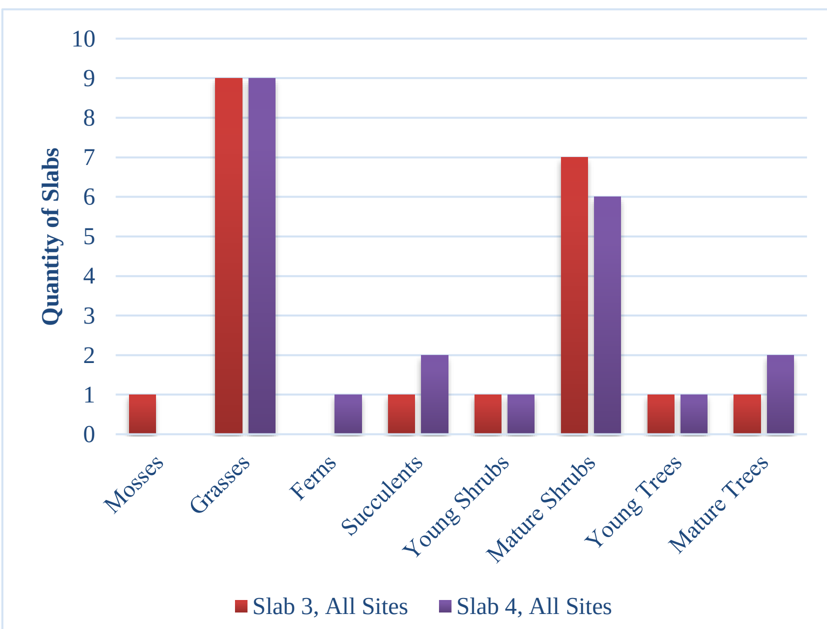

Figure 25: **Distribution of vegetation across Slabs 3 and 4 at all study sites.** It should be noted here that some sites were counted more than once because they exhibited multiple types of vegetation.

1B: Aspect

Slab aspects were plotted using Oriana® 4 (Kovach Computing Services), with the intent of later correlating orientation to incoming sunlight. Direction data is reported in azimuths (0 - 360°) and plotted uniaxially (Figure 26).

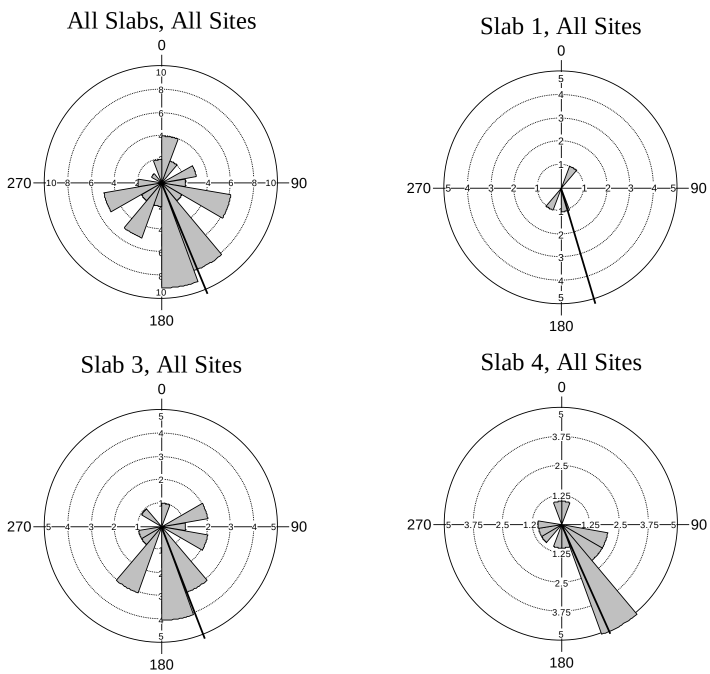

Figure 26: **Uniaxial azimuth plots of slab aspects.** The bold, black lines show the mean azimuth for each graph. There is a confident trend to the southeast in all slabs (138 - 168◦).

1C: Slab Thickness

A standard statistical analysis was completed on the entire slab thickness (cm) population as well as each slab division (2 – 4) (Table 4).

Table 4: **Standard statistical analyses of slab thickness (cm).**

	Slabs 2 - 4, All Sites	*Slab 2, All Sites*	*Slab 3, All Sites*	*Slab 4, All Sites*
Mean	36	45	36	34
Median	25	22	26	25
Mode	30	124	30	28
Std Dev	37	45	37	34
Range	183	122	174	182
Minimum	2	2	3	3
Maximum	185	124	177	185
Count	134	17	65	52

The thickness of these slabs has a wide range distribution, as noted in Table 4. However, Slabs 2 – 4 at all sites exhibited a characteristic thickness most frequently within the range of 20 – 30 centimeters (Figure 27).

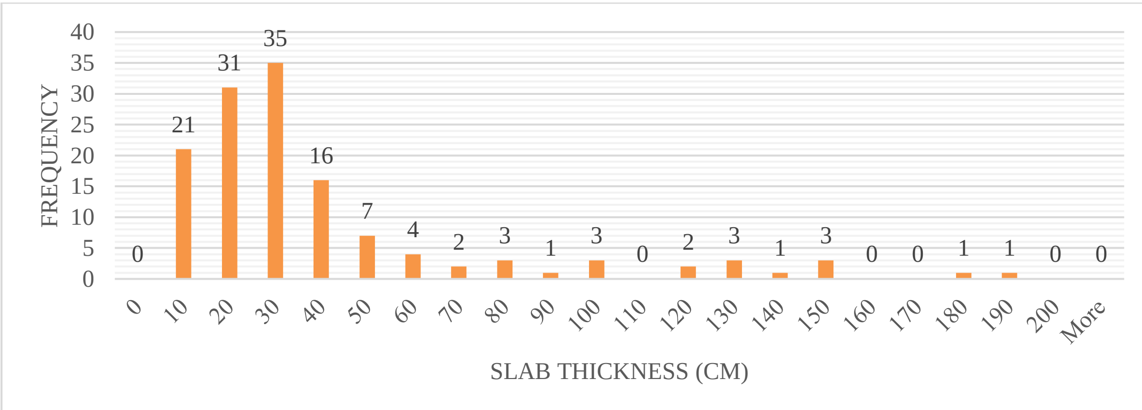

Figure 27: **Slab thickness frequency.** This histogram displays all thickness measurements of Slabs 2 - 4 at all sites (n = 41). Slab 1 thickness could not be measured.

Further analysis was performed on the slab thickness data to address whether each slab population was statistically different via a single factor one-way analysis of variance (ANOVA) and a Student's t-test. The single factor ANOVA tests the null hypothesis that the difference between the means of multiple populations are statistically the same using the following equation:

Equation 2: **Single factor ANOVA test**

$$H_0: \mu_1 = \mu_2 = \mu_3 = \cdots = \mu_k$$

Where:

μ = population mean k = number of populations

This function was executed in Microsoft Excel ® 2013 to generate a P-value, by which a value less than 0.05 implies that the populations are statistically different. Slab 2, Slab 3, and Slab 4 thicknesses were evaluated and produced an overall P-value of 0.582. Therefore, the null hypothesis was accepted, showing that the populations means are statistically the same (see Appendix E for complete ANOVA table). To find out if all population means were statistically equal or just select populations, Student's t-tests were performed to assess all relationships between means. All slab data populations were deemed as unpaired due to different sample sizes, and variance was evaluated in two different conditions: unequal (different variances) and equal (same/very similar variances). Also, statistical significance was evaluated in both one-tailed and two-tailed distribution scenarios. Under these assumptions, the statistic is calculated with the following set of equations:

Equation 3: **Equal variance Student's t-test**

$$t = \frac{(\bar{x} - \bar{y}) - (\mu_x - \mu_y)}{s\sqrt{\frac{1}{n_x} + \frac{1}{n_y}}}$$

has distribution $T(n_x + n_y - 2)$ where

$$s^2 = \frac{(n_x - 1)s_x^2 + (n_y - 1)s_y^2}{(n_x - 1) + (n_y - 1)}$$

Equation 4: **Unequal variance Student's t-test**

$$t = \frac{(\bar{x} - \bar{y}) - (\mu_x - \mu_y)}{\sqrt{\frac{s_x^2}{n_x} + \frac{s_y^2}{n_y}}}$$

has distribution $T(m)$ where

$$m = \frac{\left(\frac{s_x^2}{n_x} + \frac{s_y^2}{n_y}\right)^2}{\frac{\left(\frac{s_x^2}{n_x}\right)^2}{n_x - 1} + \frac{\left(\frac{s_y^2}{n_y}\right)^2}{n_y - 1}}$$

Where:

x bar = sample 1 mean	y bar = sample 2 mean	s^2_1 = sample 1 variance
s^2_2 = sample 2 variance	μ_1 = sample 1 size	μ_2 = sample 2 size

This function was also executed in Microsoft Excel ® 2013 to generate a ρ-value, by which a value less than 0.05 implies that the populations are statistically different. As that this equation is only functional for two populations, it was repeated until all slabs had been compared to one another. This showed that all slab thickness populations have p-values greater than 0.05 (Table 5) and, therefore, all population means are statistically equal (see Appendix E for complete t-test tables).

Table 5: **Summary Student's t-test results for slab thickness comparisons.**

	Distribution	p-value
Slab 2 : Slab 3		
Equal Variances	One Tailed	0.1882
	Two Tailed	0.3764
Unequal Variances	One Tailed	0.2181
	Two Tailed	0.4362
Slab 2 : Slab 4		
Equal Variances	One Tailed	0.1563
	Two Tailed	0.3125
Unequal Variances	One Tailed	0.1933
	Two Tailed	0.3866
Slab 3 : Slab 4		
Equal Variances	One Tailed	0.4336
	Two Tailed	0.8672
Unequal Variances	One Tailed	0.4330
	Two Tailed	0.8660

1D: Schmidt Hammer

Schmidt hammer rebound values were analyzed for each slab (Table 6).

Table 6: **Standard statistical analyses of all Schmidt hammer rebound values.**

	All Slabs, All Sites	*Slab 1, All Sites*	*Slab 2, All Sites*	*Slab 3, All Sites*	*Slab 4, All Sites*
Mean	28.48	49.63	34.00	28.03	19.17
Median	27	52	34	28	18
Mode	18	52	38	18	18
Std Dev	12.53	10.81	10.84	10.64	7.46
Range	60	57	54	50	40
Minimum	7	10	10	10	10
Maximum	67	67	64	60	50
Count	5505	298	1707	1906	1594

Further, single factor ANOVA (Equation 2) and Student's t-tests (Equations 3 and 4) were performed on the per-slab populations of R-values, again in Microsoft Excel ®

2013. When analyzing all slabs as a group, the single factor ANOVA produced an interesting result of P = 0, which would indicate that at least two of the Schmidt hammer R-value populations are significantly statistically different. The Student's t-tests were run to assess each statistical slab relationship to identify where these differences are. With all p-values being less than 0.05, all Schmidt hammer R-values for all slab relationships are statistically very different. The results of these tests are included in Table 7 (in depth statistical tables included in Appendix E).

Table 7: **Summary Student's t-test results for Schmidt hammer R-value populations.**

	Distribution	p-value		Distribution	p-value
Slab 1 : Slab 2			**Slab 2 : Slab 3**		
Equal Variances	One Tail	4.2E-104	Equal Variances	One Tail	1.24E-60
	Two Tail	8.4E-104		Two Tail	2.49E-60
Unequal Variances	One Tail	5.13E-76	Unequal Variances	One Tail	1.77E-60
	Two Tail	1.03E-75		Two Tail	3.54E-60
Slab 1 : Slab 3			**Slab 2 : Slab 4**		
Equal Variances	One Tail	3.9E-190	Equal Variances	One Tail	0
	Two Tail	7.9E-190		Two Tail	0
Unequal Variances	One Tail	3.3E-112	Unequal Variances	One Tail	0
	Two Tail	6.6E-112		Two Tail	0
Slab 1 : Slab 4			**Slab 3 : Slab 4**		
Equal Variances	One Tail	0	Equal Variances	One Tail	4.4E-156
	Two Tail	0		Two Tail	8.7E-156
Unequal Variances	One Tail	6.2E-153	Unequal Variances	One Tail	2.7E-164
	Two Tail	1.2E-152		Two Tail	5.3E-164

For all slabs at all sites, Schmidt hammer rebound values were, generally, highest at the stratigraphically-lowest slab (Slab 1), and lowest at the stratigraphic-highest slab (Slab 4). Figure 28 shows the frequency distribution of Schmidt hammer R-values that were retrieved from all slab at all sites.

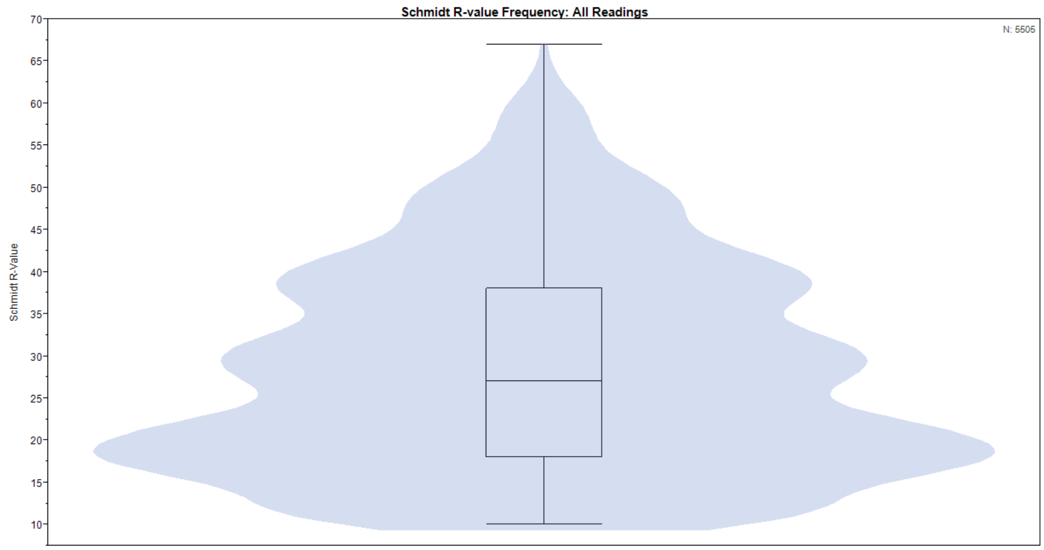

Figure 28: **Schmidt hammer R-value frequency - all slabs, all sites.**

Results may be slightly skewed in that there were significantly less “Slab 1” or fresh slabs than older generations of exfoliation. To address this, frequency analyses were divided by their slab identification number (i.e. 1 – 4) (Figure 29).

1E: Slope and Bearing

For each surface that a transect was collected, a slope of that surface was also collected. These slopes were plotted in slab groups to identify any observable correlation between slope and slab age. This plot is included in Appendix K. As can be seen at all sites, slope is constant except for some outliers on Surfaces 2 - 4. This may be a potential source of bias, in that transects were not possible to complete on overly-steep surfaces.

In this context, the bearings of the transects were plotted to see if directional bias was introduced when collecting transect data. These diagrams are included in Appendix L. Transect direction is seemingly random on all slabs at all sites, except for a slight trend to the southwest on Surface 2.

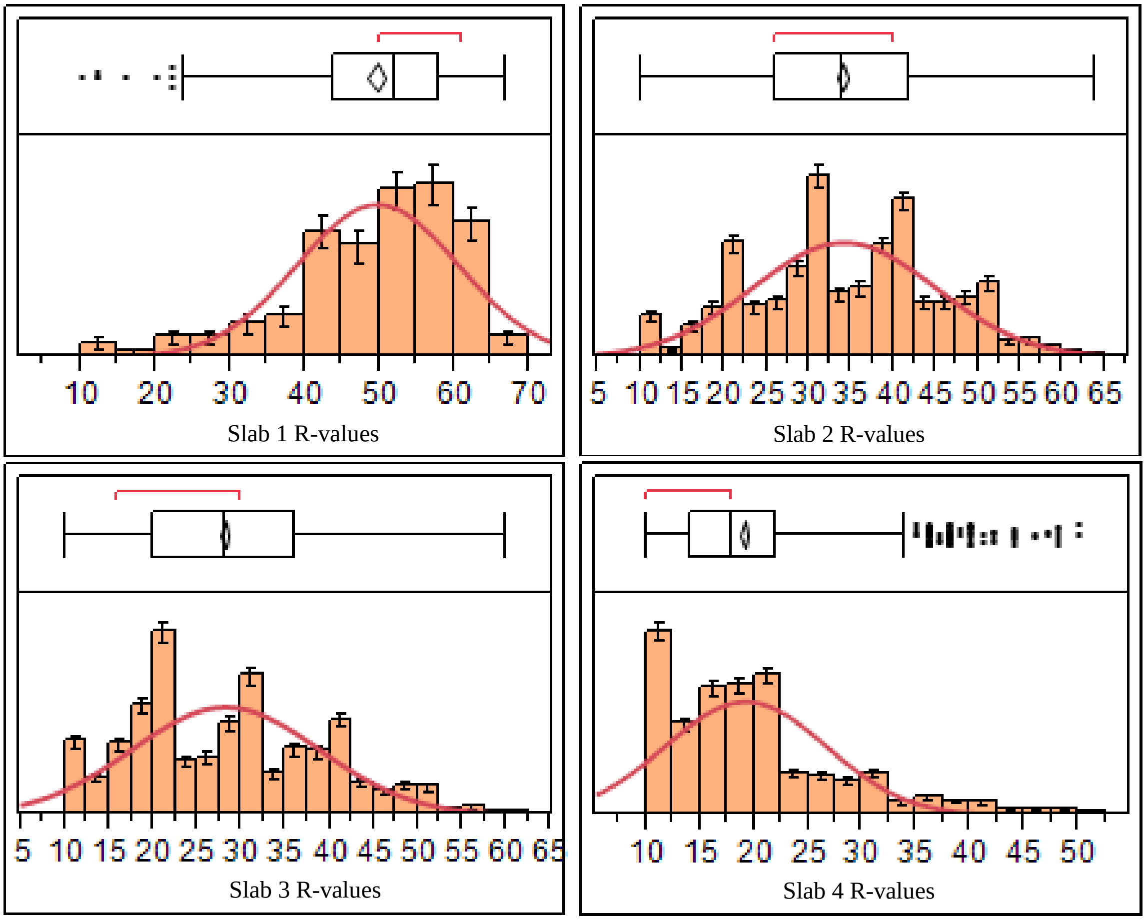

Figure 29: **Schmidt hammer R-value frequency distributions, separated by slab identification.** Histograms show frequency of value readings, standard distribution curves, medians, and outliers.

Section 2: Microtransect Variables

2A: Crack Face Aspects

Crack face aspects (as in the direction the exfoliated crack edge faced) were plotted into rose diagrams using Oriana® 4 (Kovach Computing Services), with the intent of later correlating orientation to incident sunlight. Direction data is reported in azimuths (0 - 360°) and plotted uniaxially. Figure 30 shows the azimuths of all cracks at all sites, as well as all cracks at all sites divided up into slabs. A diagram was also created for each slab at each site, and those diagrams can be found in Appendix F.

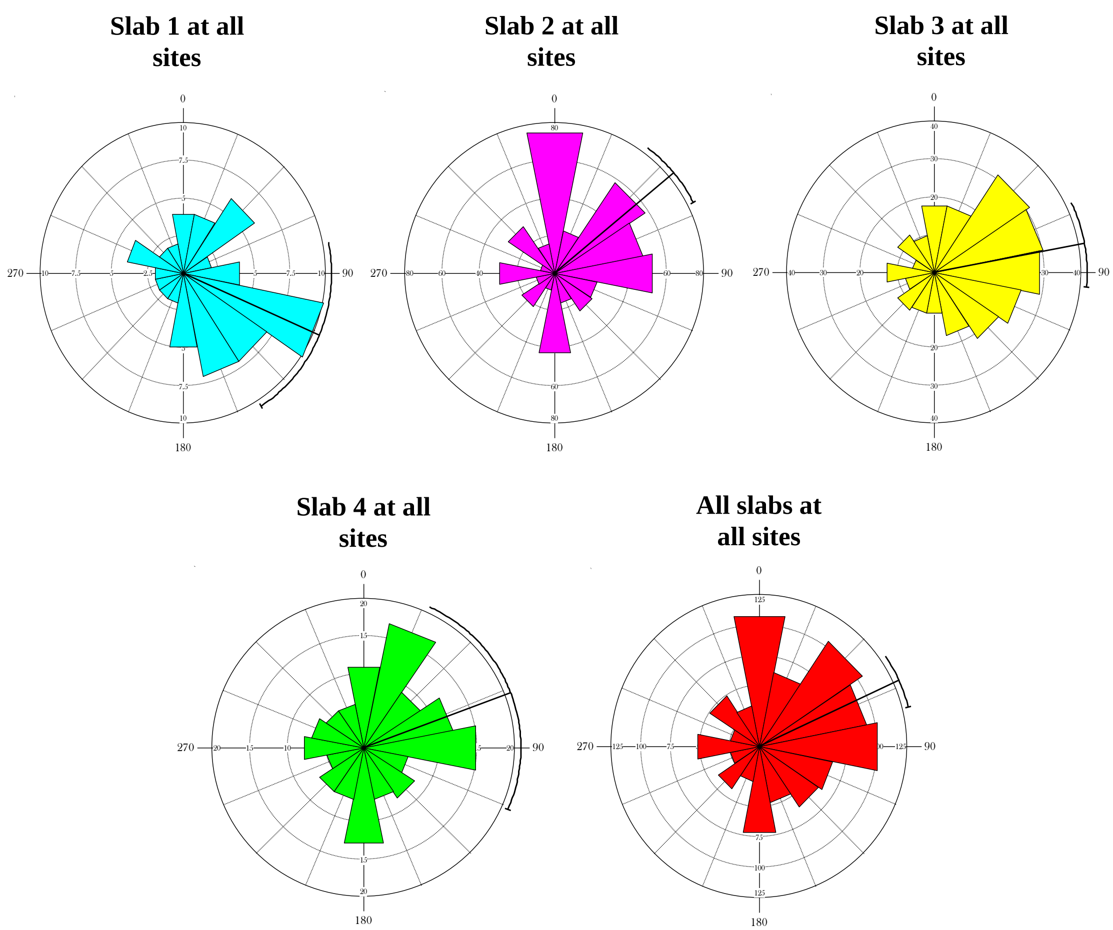

Figure 30: **Uniaxial azimuth plots of crack face aspects.** The bold, black lines show the mean azimuth for each graph. Most of the groups display a trend towards the northeast.

2B: Crack Length

A standard statistical analysis was completed on the collected lengths of every linear void longer than 2 centimeters. The data set was evaluated as a total population and divided up by slab (1 – 4) (Table 8).

Table 8: **Summary statistics for crack (all > 2 cm) lengths (millimeters).**

	All Slabs, All Sites	*Slab 1, All Sites*	*Slab 2, All Sites*	*Slab 3, All Sites*	*Slab 4, All Sites*
Mean	253.90	200.18	260.87	269.87	226.18
Median	62.00	46.00	76.00	52.00	61.00
Mode	42.00	38.00	42.00	27.00	22.00
Std Dev	734.67	539.86	692.02	905.68	590.62
Range	7996.50	3849.80	7991.30	7166.50	4842.50
Minimum	3.50	20.20	8.70	3.50	7.50
Maximum	8000.00	3870.00	8000.00	7170.00	4850.00
Count	1049.00	67.00	522.00	291.00	169.00

Further, single factor ANOVA (Equation 2) and Student's t-tests (Equations 3 and 4) were performed on the per-slab populations of crack length, again in Microsoft Excel ® 2013. When analyzing all slabs as a group, the single factor ANOVA produced a result of P = 0.853811, which would indicate that at least two of the crack length populations are statistically equal. The Student's t-tests were run to assess each statistical slab relationship to identify where these similarities are. With all p-values being greater than 0.05, all the crack length populations are statistically the same. The results of these tests are included in Table 9 (in depth statistical tables included in Appendix E).

Table 9: **Summary Student's t-test results for crack length (millimeters) populations.**

	Distribution	**p-value**
Slab 1 : Slab 2		
Equal Variances	One Tail	0.244875
	Two Tail	0.489749
Unequal Variances	One Tail	0.202564
	Two Tail	0.405128

Slab 1 : Slab 3		
Equal Variances	One Tail	0.272724
	Two Tail	0.545449
Unequal Variances	One Tail	0.205825
	Two Tail	0.411649
Slab 1 : Slab 4		
Equal Variances	One Tail	0.377588
	Two Tail	0.755176
Unequal Variances	One Tail	0.373008
	Two Tail	0.746017
Slab 2 : Slab 3		
Equal Variances	One Tail	0.436959
	Two Tail	0.873917
Unequal Variances	One Tail	0.441486
	Two Tail	0.882972
Slab 2 : Slab 4		
Equal Variances	One Tail	0.278969
	Two Tail	0.557937
Unequal Variances	One Tail	0.262814
	Two Tail	0.525628
Slab 3 : Slab 4		
Equal Variances	One Tail	0.28735
	Two Tail	0.574699
Unequal Variances	One Tail	0.266038
	Two Tail	0.532077

Crack length values were plotted in a bivariate correlation to understand the strength of the relationship between slab number and crack length (Figure 31). The R^2 value (which quantifies the statistical relationship between two variables) is very close to 0,

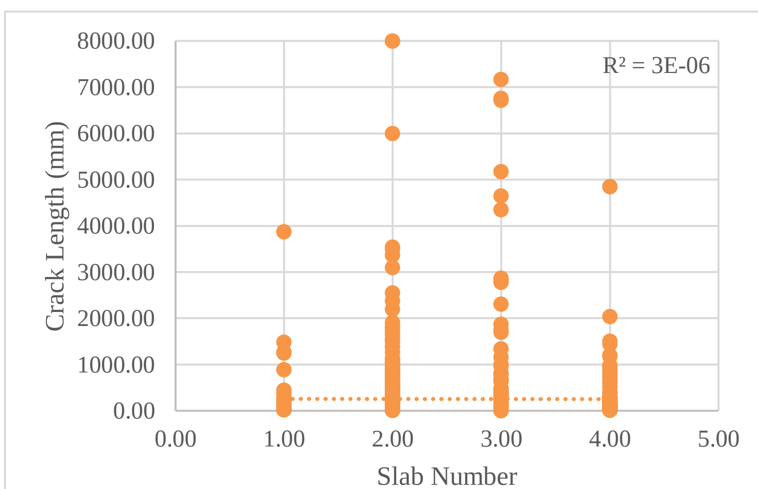

Figure 31: **Bivariate correlation plot relating slab identification to crack length (mm).**

indicating that slab number and crack length are not correlated. These values were also plotted in histograms to visualize the distribution of lengths found in each slab at all sites (Figure 32). Being that all crack length populations are statistically equal, it is not unexpected that all of these populations display a characteristic length range of approximately 40 – 80 millimeters.

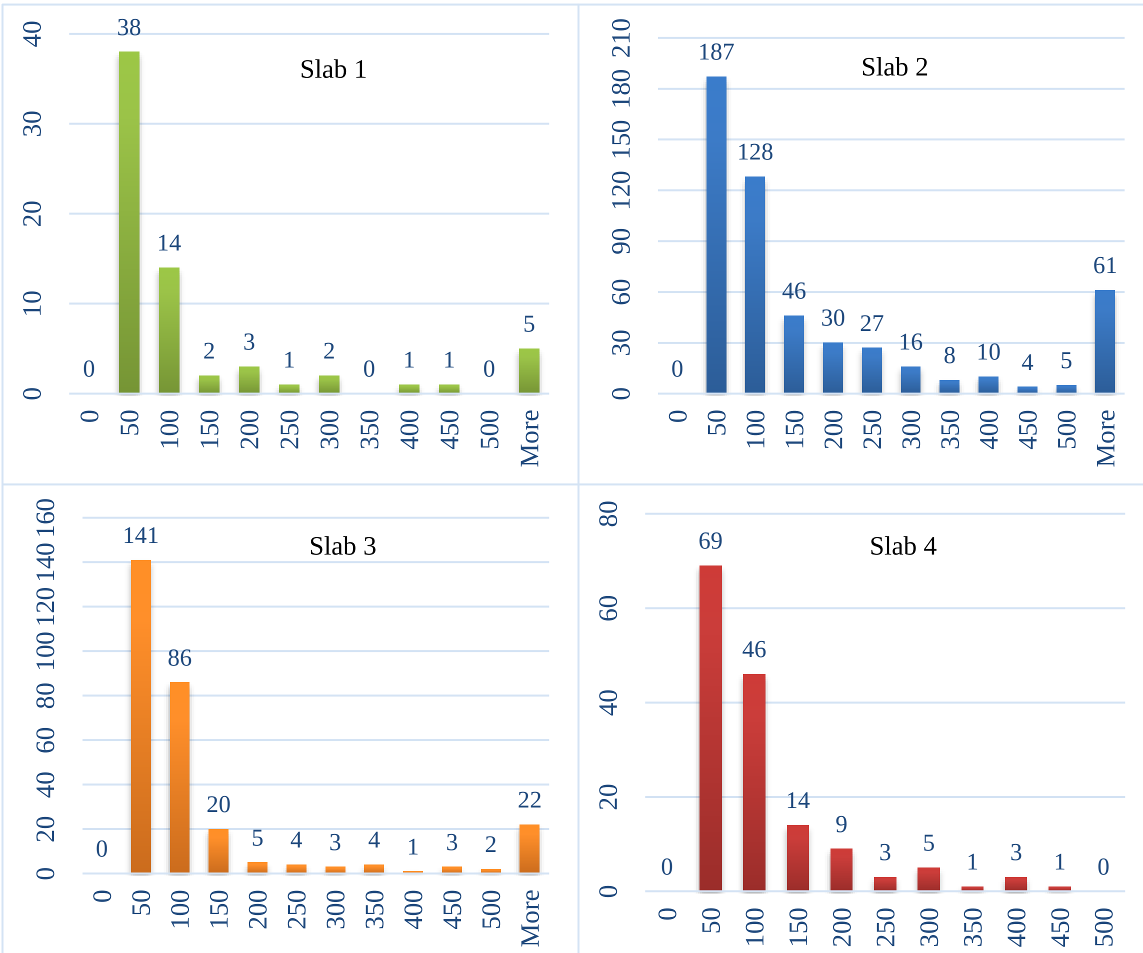

Figure 32: **Crack length distribution per slab.** In these histograms, the y-axis is frequency and the x-axis is crack length in millimeters.

Finally, all measured crack lengths were summed and then divided by the length of the transect. This produced a unit-less estimation of crack density for each slab, per site. The results of this are reported in Appendix I.

2C: Crack Height / Spall Thickness

Crack height, in this case, is synonymous with spalling thicknesses, and these terms will be used interchangeably throughout the rest of this document. A standard statistical analysis was completed on the collected heights of every linear void longer than 2 centimeters, if a "height" was present. The data set was evaluated as a total population and divided up by slab (1 – 4) (Table 10).

Table 10: **Summary statistics for microtransect spall thicknesses / crack heights (millimeters).**

	All Slabs, All Sites	*Slab 1, All Sites*	*Slab 2, All Sites*	*Slab 3, All Sites*	*Slab 4, All Sites*
Mean	11.0	5.5	8.8	8.0	25.4
Median	5.5	3.8	5.7	4.7	7.8
Mode	0.0	3.5	5.0	0.0	0.0
Std Dev	34.9	6.2	13.2	18.4	78.8
Range	915.0	39.0	120.0	265.0	915.0
Minimum	0.0	0.0	0.0	0.0	0.0
Maximum	915.0	39.0	120.0	265.0	915.0
Count	1049.0	67.0	522.0	291.0	169.0

Further, single factor ANOVA (Equation 2) and Student's t-tests (Equations 3 and 4) were performed on the per-slab populations of spalling thicknesses, again in Microsoft Excel ® 2013. When analyzing all slabs as a group, the single factor ANOVA produced a P-value of 0.000000113, which would indicate that at least two of the spalling thickness populations are significantly statistically different. The Student's t-tests were run to assess each statistical slab relationship to identify where these differences are. These results were varied. The spalling thickness of Slabs 1 and 4 appear to be distinct from each other and from Slabs 2 and 3, which are similar to each other. The results of these tests are included in Table 11 (in depth statistical tables included in Appendix E).

Table 11: **Summary Student's t-test results for crack height / spall thickness (millimeters) populations.**

	Distribution	p-value
Slab 1 : Slab 2		
Equal Variances	One Tail	0.021505
	Two Tail	0.043009
Unequal Variances	One Tail	0.000312
	Two Tail	0.000624
Slab 1 : Slab 3		
Equal Variances	One Tail	0.132858
	Two Tail	0.265717
Unequal Variances	One Tail	0.027359
	Two Tail	0.054717
Slab 1 : Slab 4		
Equal Variances	One Tail	0.020001
	Two Tail	0.040002
Unequal Variances	One Tail	0.000664
	Two Tail	0.001329
Slab 2 : Slab 3		
Equal Variances	One Tail	0.241307
	Two Tail	0.482614
Unequal Variances	One Tail	0.260773
	Two Tail	0.521547
Slab 2 : Slab 4		
Equal Variances	One Tail	2.25E-06
	Two Tail	4.5E-06
Unequal Variances	One Tail	0.003528
	Two Tail	0.007057
Slab 3 : Slab 4		
Equal Variances	One Tail	0.000175
	Two Tail	0.00035
Unequal Variances	One Tail	0.002635
	Two Tail	0.00527

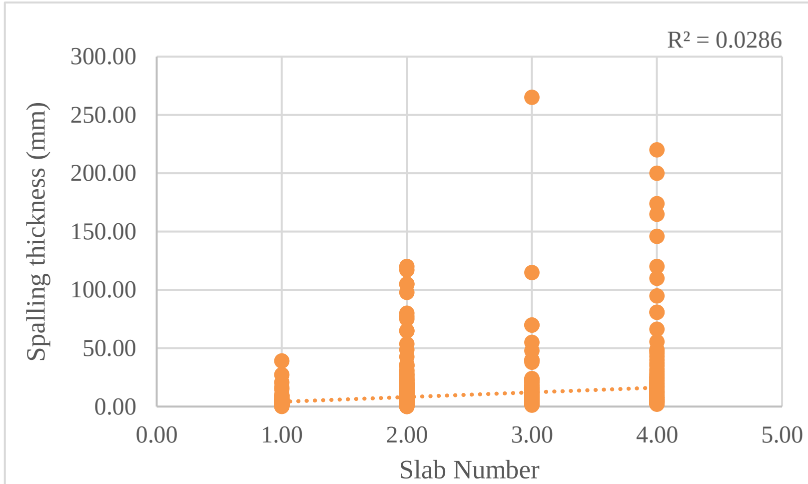

Figure 33: **Bivariate correlation plot relating slab identification to crack height (mm).**

Crack height values were plotted in a bivariate correlation to understand the strength of the relationship between slab number and crack height (Figure 33). The R^2 value (0.0286) indicates a slight positive correlation between that slab number and crack height. These values were also plotted in histograms to visualize the distribution of

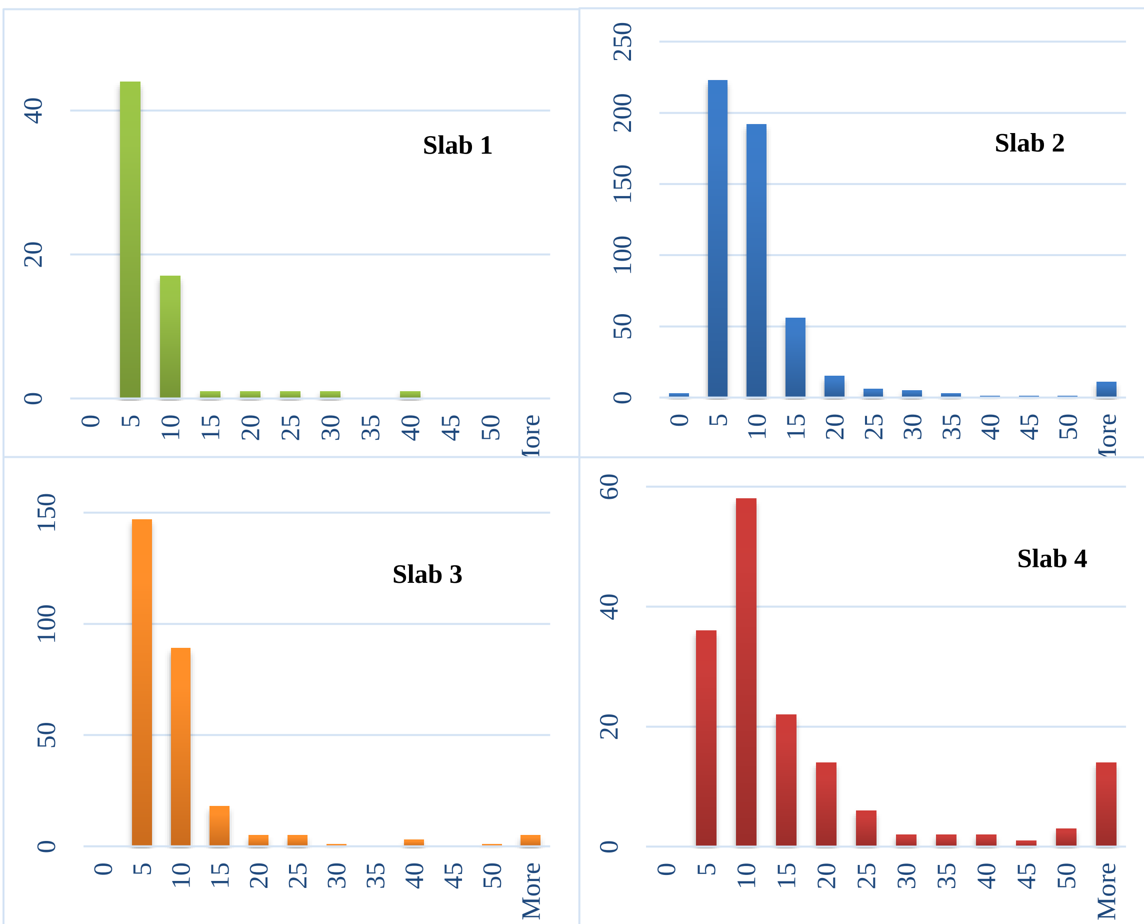

Figure 34: **Crack height distribution per slab.** In these histograms, the y-axis is frequency and the x-axis is crack height in millimeters.

heights found in each slab at all sites (Figure 34). Although most of the populations are statistically different, spalling thicknesses display a characteristic 5 – 10 millimeters.

2D: Evidence of other cracking

As stated earlier, in the immediate of the vicinity of each crack, it was noted whether granular disintegration, micro-spalls, and/or micro-cracks (less than two centimeters in length) were present. All cracks were grouped together per-slab to find a percentage of each variables' presence (Figure 35).

SLAB 1 **SLAB 2** **SLAB 3** **SLAB 4**

Presence of linear voids < 2 cm long ("microcracks"):

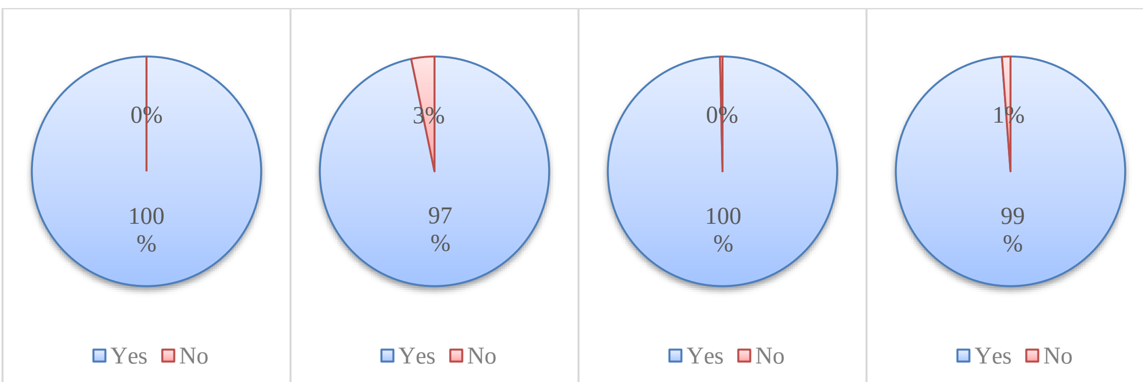

Presence of granular disintegration:

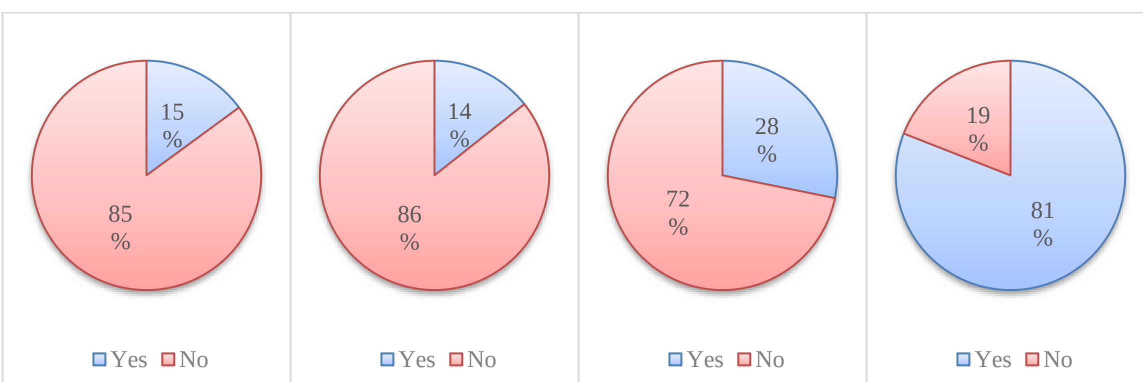

Presence of microspalling:

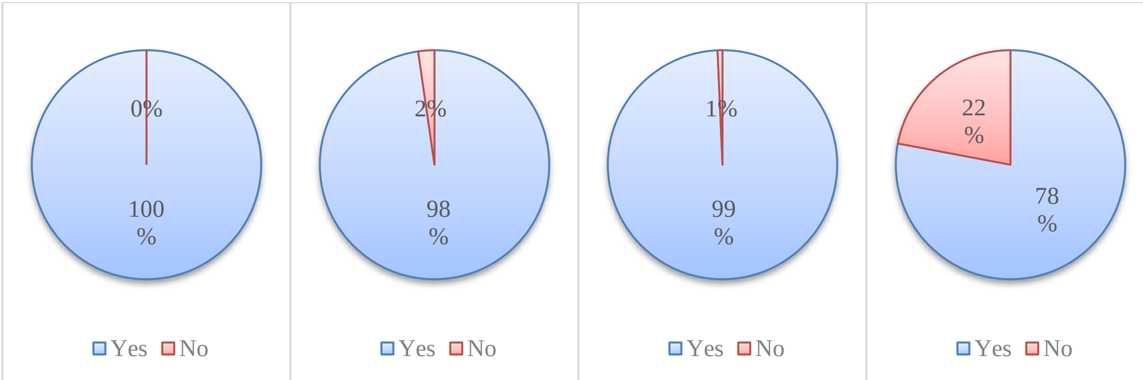

Figure 35: **Percent of observed weathering variables.** Noted weathering characteristics near every measured crack in the microtransect. Grouped by slab.

2E: Weathering Index

A standard statistical analysis was completed on the collective assigned weathering indices of every linear void longer than two centimeters. Occasionally, the cracks would manifest as a range of weathering indices. In those situations, the weathering index values were averaged for the crack. The data set was evaluated as a total population and divided up by slab (1 – 4) (Table 12).

Table 12: **Summary statistics for assigned crack weathering index.**

	All Slabs, All Sites	*Slab 1, All Sites*	*Slab 2, All Sites*	*Slab 3, All Sites*	*Slab 4, All Sites*
Mean	4.62166	4.265152	4.70977	4.591379	4.541176
Median	4.5	4	5	4.5	4.5
Mode	4	4	4	4	4
Std Dev	0.925206	0.924952	0.97402	0.840844	0.871005
Range	5	4	5	3	3
Minimum	1	2	1	3	3
Maximum	6	6	6	6	6
Count	1048	66	522	290	170

Further, single factor ANOVA (Equation 2) and Student's t-tests (Equations 3 and 4) were performed on the per-slab populations of weathering index averages, again in

Microsoft Excel ® 2013. When analyzing all slabs as a group, the single factor ANOVA produced a P-value of 0.001023, which would indicate that at least two of the spalling thickness populations are statistically different. The Student's t-tests were run to assess each statistical slab relationship to identify where these differences are. Most of the relationships produced a p-value of less than 0.05, indicating that they were statistically different, except for Slab 2 and Slab 3 (like the results of the t-tests performed on spalling thicknesses). The results of these tests are included in Table 13 (in depth statistical tables included in Appendix E).

Table 13: **Summary Student's t-test results for weathering index populations.**

	Distribution	p-value
Slab 1 : Slab 2		
Equal Variances	One Tail	0.000238
	Two Tail	0.000477
Unequal Variances	One Tail	0.000222
	Two Tail	0.000444
Slab 1 : Slab 3		
Equal Variances	One Tail	0.002766
	Two Tail	0.005531
Unequal Variances	One Tail	0.00503
	Two Tail	0.01006
Slab 1 : Slab 4		
Equal Variances	One Tail	0.016398
	Two Tail	0.032795
Unequal Variances	One Tail	0.019394
	Two Tail	0.038788
Slab 2 : Slab 3		
Equal Variances	One Tail	0.041066
	Two Tail	0.082133
Unequal Variances	One Tail	0.034995
	Two Tail	0.069989
Slab 2 : Slab 4		
Equal Variances	One Tail	0.022408
	Two Tail	0.044815
Unequal Variances	One Tail	0.017076
	Two Tail	0.034153

Slab 3 : Slab 4		
Equal Variances	One Tail	0.271104
	Two Tail	0.542207
Unequal Variances	One Tail	0.273007
	Two Tail	0.546014

Weathering index density was plotted in a bivariate correlation between slab number and weathering index average to better understand the relationship between these two variables (Figure 36).

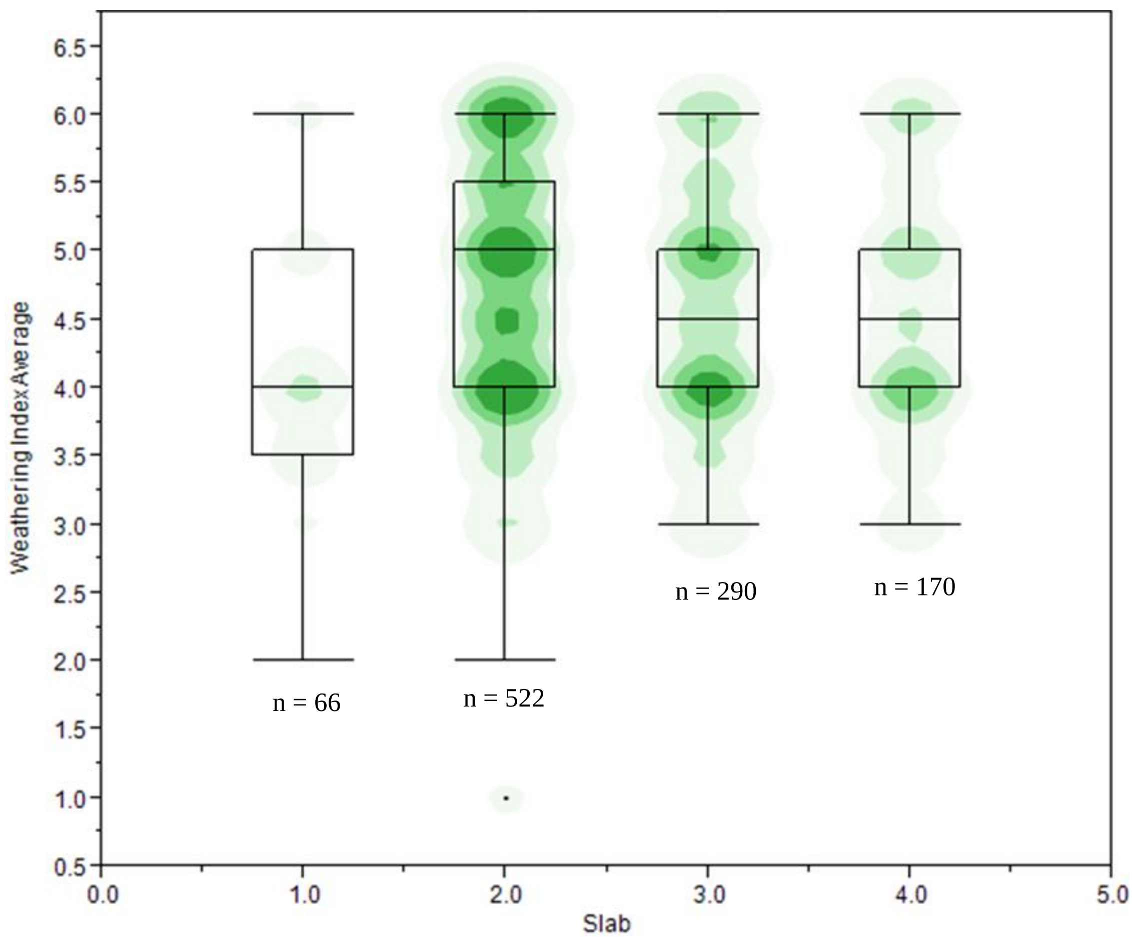

Figure 36: **Bivariate correlative heat map of crack weathering index.** Color intensity increases as frequency of that weathering index number increases.

Section 3: Sensor Readings

Daily temperature, light and acoustic emission sensor data can be found in Appendix G. They are discussed in the following section.

DISCUSSION

In this section, the field and sensor data from Twain Harte will be interpreted and synthesized in the context of hypotheses derived from previous studies.

If crustal unloading (via deglaciation or water-table lowering) triggered cracking, other such events should be evident regionally.

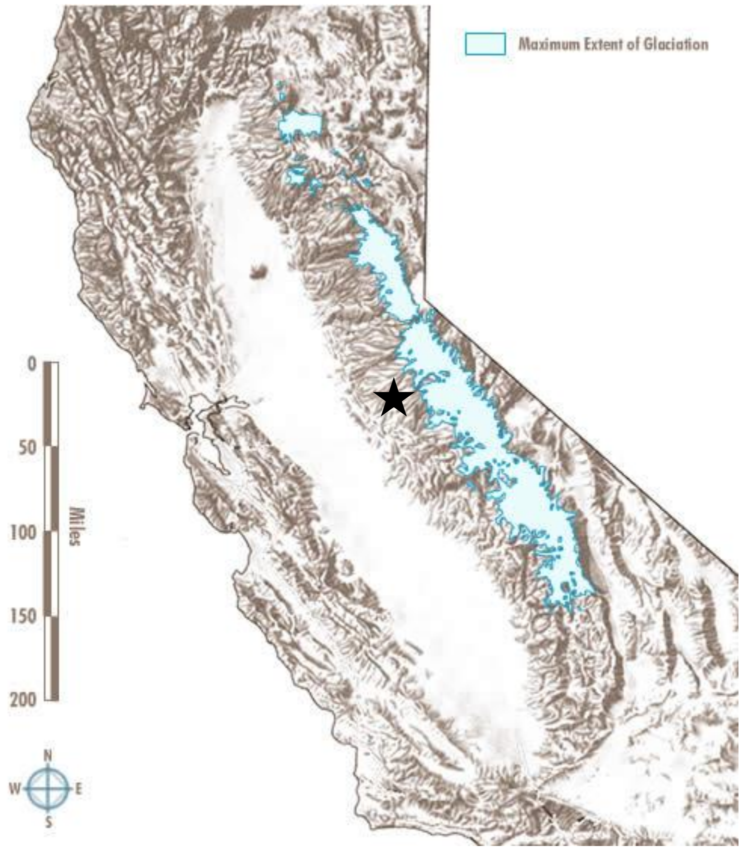

Figure 37: **Maximum extent of Quaternary glaciation.** The star indicates the approximate location of Twain Harte and the study sites. Map from *Sierra Nevada Photos*, http://www.sierranevadaphotos.com/geography/glaciation.asp

While the highlands of the Sierras were heavily glaciated during the Last Glacial Maximum (Figure 37), the region of Twain Harte remained untouched by the maximum extent of Quaternary glaciers (Gillespie and Clark, 2011). Personal communication from Gillespie (2017) also confirms that post-Last-Glacial-Maximum downstream incision of the granitic bedrock in the Twain Harte region is likely minimal (on the order of meters only). These data indicate that glacial scour did not contribute to significant crustal unloading in the vicinity of Twain Harte.

Further, only Twain Harte and its immediately adjacent sites had fresh (weathering index of 0 - 1) cracking based on observations of the weathering of crack edges (Figure 36). No fresh cracks were found at any other sites, suggesting that the 2014 macrofracturing events are, to date, unique to Twain Harte. Were it the case that large-scale, relatively sudden, regional crustal unloading due to drought-induced water table lowering or glacial scour caused this exfoliation, more fresh cracks would likely have been found in other places near Twain Harte where crustal lowering is of a similar magnitude according to Borsa, 2014 (Figure 9). Alternatively, there could be something unique about Twain Harte causing the rapid exfoliation that happened in the video recording (Dotysan, 2014), however the data presented herein suggests that domes in the region are similar in both their overall morphology as well as the characteristics of their associated exfoliation slabs.

Dome curvature should correlate with slab thickness (Martel, 2011).

If localized stress data were available (i.e. Figure 14), it would set the stage for testing Martel's (2006, 2011) curvature mechanics hypothesis. After several attempts to utilize the available data, it was found that the regional scale at which stress data is currently available is insufficient to properly utilize Martel's curvature modeling. It is recommended that, to continue testing the Martel model, it would be necessary to utilize the extensometer data collected by Dr. Collins and Dr. Stock, where they continuously monitored the near surface stress-strain environment of Twain Harte Rock. A further application of the extensometer data would be to interpret whether the stress levels at Twain Harte Rock are considerably higher than that found regionally. If it was found that they were, this would be supporting evidence for the implication that Twain Harte Rock has a unique intermingling of multiple exfoliation drivers (i.e. anthropogenic influences, dam/reservoir stress enhancement) when compared to the other more remote regional sites. Using this data would be essential to understand how surface morphology influences the formation of sheet joints.

Spatial and temporal variance in exfoliation processes.

Overall, macroscale (slab) and microscale (spall) exfoliation thicknesses were consistent across all sites. All slab thickness populations were found to be statistically the same (Table 5), with a characteristic thickness of 20 – 30 centimeters on all slabs at all sites (Figure 27). All measured spalling thickness (a.k.a. crack height) populations were also statistically the same (Table 10), with the exception of the relationship between Slab 2 and Slab 3. A complication that may explain this variance could lie in the correlation between slabs across sites – for example, stratigraphic Slab 3 at one site could be the same age as Slab 4 at another site. Regardless, because of the statistic equality between spalling thickness populations, it is significant that spalls had a characteristic thickness of 5 – 10 millimeters (Figure 34). Based on the macroscale (slabs) and microscale (spalls) exfoliation thickness consistency, it is likely that the drivers of exfoliation processes are temporally and spatially continuous in this region.

The timeline of cracking occurring at all sites appeared consistent as well. In efforts to quantify this periodicity, weathering-proxy field data was collected from each slab. The Schmidt hammer R-values were utilized as an age proxy to provide a general understanding of the relative ages between these slabs (Figure 38). In the case of the Twain Harte region, a strong negative correlation was found between R-value (rock strength) and slab age. Being that all Schmidt hammer R-value populations are statistically different, this relationship is significant. Therefore, this confirms that each slab was exposed at a distinctly different interval from its over- or underlying neighbor.

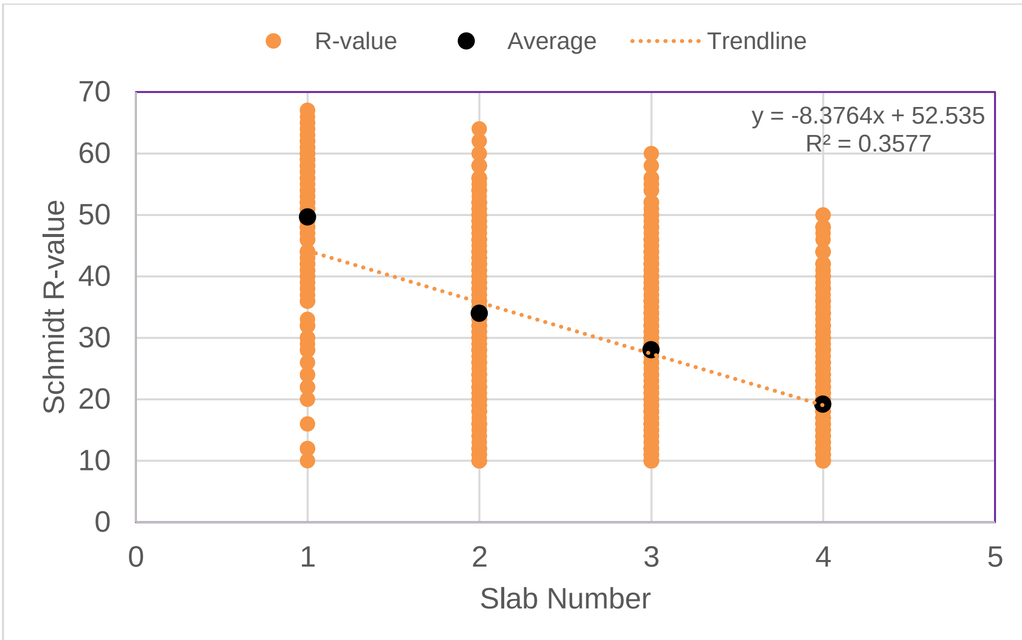

Figure 38: **Schmidt hammer R-value bivariate correlation with slab number.**

Generally, observed crack length values increased with slab age and levelled off with the oldest slab (Figure 32). This trend is attributed to a concomitant increase in granular disintegration, where the rock weathering is so advanced that is it falling apart along grain boundaries rather than maintaining enough strength for cracking to occur. This is further supported in Figure 35: for all Slab 4, the presence of granular disintegration increases to 81% and microspalling decreases to 78%. Also, cracks on older slabs exhibited higher degrees of weathering. Each average index population was found to be statistically different from the slab neighbor except for the relationship between Slab 3 and Slab 4 (Table 13), again suggesting that a maximum weathering is reached at “Slab 3 time,” as is typical of weathering processes (Birkeland, 1999).

Based on these weathering-proxy variables, it is possible to assign relative age relationships to the different slabs. As can be seen in Figure 39, a dramatic change occurs between Slab 1 and Slab 2 – which is understandable being that Slab 1 is a freshly exposed surface that has not been subjected to any form of weathering. The transition between Slab 2 and Slab 3 is more consistent with a slight increase in weathering. This data representing this transition could be a bit skewed, as mentioned previously – it is possible that these two slabs could be stratigraphically different at some sites (with Twain Harte Rock as a baseline), but the same absolute age. A significant increase in weathering variables occurs between Slab 3 and Slab 4. This is in support of the aforementioned idea that other weathering processes besides simple cracking, like granular disintegration, are starting to contribute to weathering.

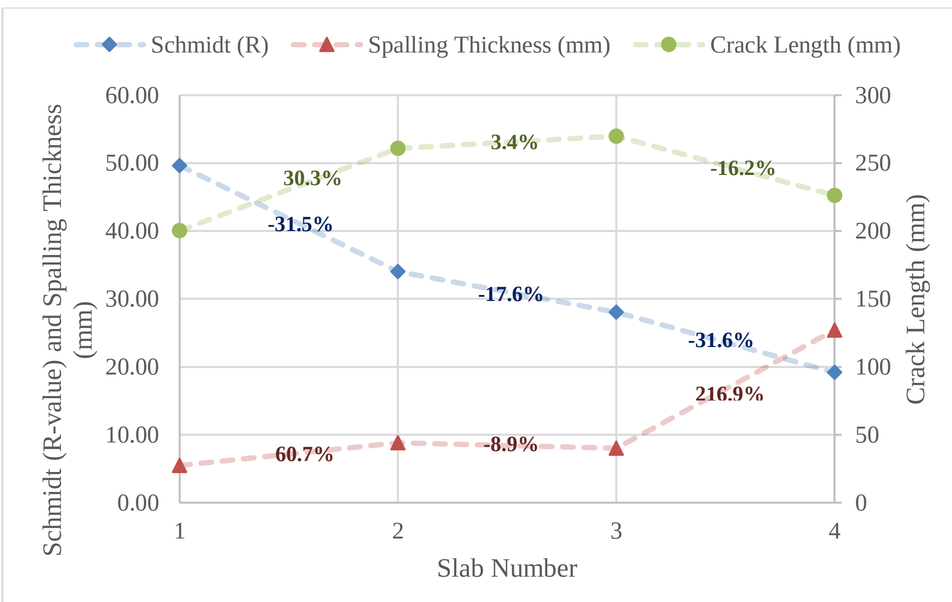

Figure 39: **Multiple weathering variables and the percent change between slabs.**

There is no difference, however, in slab thickness through time at any site. Thus, these data suggest that exfoliation events are happening periodically through time and that the driver of exfoliation has not changed. Overall, the collected data support the hypothesis initially proposed by Martel (2006, 2011) that exfoliation event long-term periodicity can be predictable.

Although overall timing of exfoliation seemed similar at all sites, the event at Twain Harte appeared unique, as previously mentioned. Based on the observations of Stock et al. (2012), rapid rock exfoliation resulted in imbalanced stresses as the exfoliated slab gravitationally adjusted to ideal equilibrium stress balance. The 2014 Twain Harte Rock exfoliation events occurred on August 3rd, August 6th, August 20th, and September 4th (THLA, 2016). Just from this timeline, it can be seen that as time progressed, the interval between exfoliation events increased. It is possible that events subsequent to the original August 3rd event represented adjustments to the original event, similar to earthquake aftershocks. Another exfoliation event occurred at Twain Harte Rock on July 22nd, 2016 (THLA, 2016) – expanding the timeline of exfoliation even further. (As a side note, the 2016 exfoliation event was generally not included in this discussion due to its occurrence post-field-study, but seemed particularly relevant to understanding this concept.) This event could have been triggered by stresses caused by expansion of the slab during warm weather (i.e. Collins and Stock, 2016) that influenced the new configuration of the slab.

From this, a conceptual model for exfoliation can be proposed whereby rapid exfoliation events ultimately culminate in a return to stress equilibrium. The resulting detached exfoliation slab is then left to weather and erode without subsequent deformation. All the other sites included in the regional survey displayed at least two of these stratigraphically-differentiated slabs, suggesting spatially- and roughly temporally-consistent exfoliation activity. Martel (2006, 2011) indicated that long-term exfoliation may be predictably periodic, whereby exfoliation is triggered similar to that of faulting through accumulation of elastic strain and then release. However, the timing of the Twain Harte events (below) suggest that the actual trigger of exfoliation is environmentally related.

Exfoliation is triggered by daily temperature cycling (Eppes et al., 2016; Collins and Stock, 2016).

Weathering data on different generations of exfoliation slabs indicates that exfoliation events are happening episodically through time. The similar morphology of exfoliation slabs suggests that exfoliation processes have remained temporally constant. Here, the possible thermal triggers of sudden exfoliation observed at Twain Harte are evaluated.

Local weather station data was collected from MOUC1 Weather Station in Mount Elizabeth, California – seventeen miles northeast of Twain Harte. This weather station was established in 1999, so climatic averages are based on sixteen years' worth of data. The Mount Elizabeth Weather Station climate data was consistent with the recorded temperature sensor data from the rock surface (Figure 40), therefore it was possible to correlate the climate data directly with Twain Harte exfoliation events and with measured AE activity. Figure 40 shows that Mount Elizabeth tends to be hotter than Twain Harte, so the Twain Harte temperatures were adjusted to more accurately represent the surrounding climate. This was done using the regression equation produced by Figure 40, and these adjustments can be viewed in Appendix J.

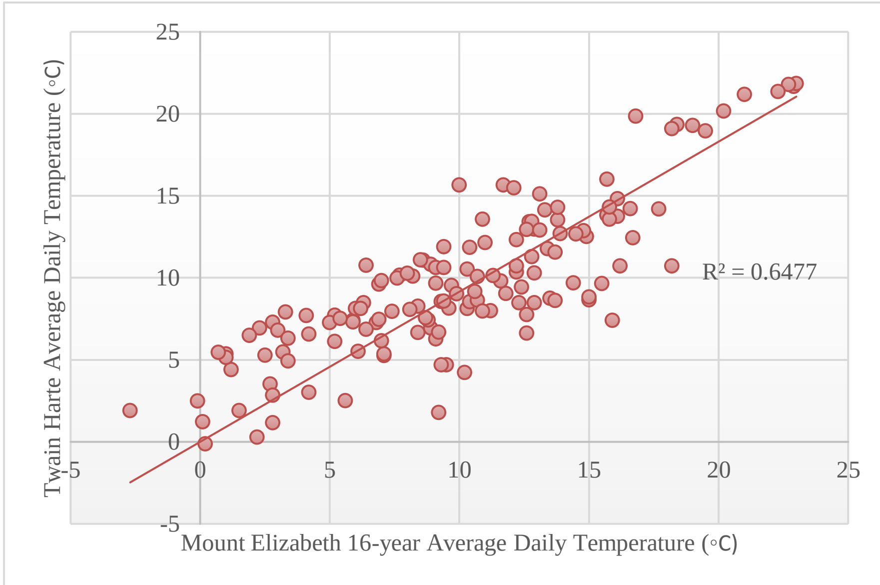

Figure 40: **Average daily temperature comparison between Twain Harte Rocks' temperature sensors and the Mount Elizabeth weather station.** The Mount Elizabeth values are 16-year daily averages. There is a strong positive correlation between the two temperature populations, indicating that they are comparable.

The four exfoliation events began in early August, which had the highest average temperatures in Twain Harte in 2014 per historical Weather Underground records (Figure 41). It was the peak of the hottest part of the year.

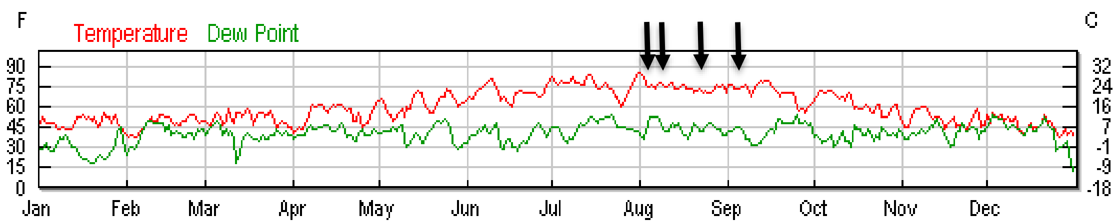

Figure 41: **Twain Harte average monthly temperature and dew point, 2014.** Graph generated by Weather Underground, https://www.wunderground.com. Arrows indicate approximate exfoliation event dates.

Based on the climate data from the Mount Elizabeth weather station, all four 2014 exfoliation events occurred on dry, hot days with conditions similar to the 16-year average (Table 14). 2014 was not the driest year based on the precipitation data from Mount Elizabeth, however it was below the climate average amidst a slight overall decline (Figure 42). Incoming solar radiation was also average, indicating that cloudiness was not increased on the exfoliation event dates in 2014.

Table 14: **Twain Harte Rocks' exfoliation event weather versus climate averages from the Mount Elizabeth weather station.**

		Solar Rad Total	AIR TEMPERATURE Ave.	Max.	Min.	RELATIVE HUMIDITY Ave.	Max.	Min.	Precip Total
		kW-hr/m2		*Deg. C*			*percent*		*mm*
August 3rd	Climate Avg	6.18	22.3	28.3	17.6	35.5	47.4	25.0	0.0
	Climate Std Dev	3.53	2.3	2.8	2.4	12.7	15.5	10.7	0.0
	8/3/2014	**3.77**	**22.3**	**26.7**	**18.9**	**31.0**	**41.0**	**24.0**	**0.0**
August 6th	Climate Avg	5.52	20.8	27.0	16.5	38.4	52.4	25.9	0.0
	Climate Std Dev	3.54	4.3	4.9	4.3	15.1	19.1	10.9	0.0
	8/6/2014	**8.18**	**20.9**	**26.7**	**16.1**	**49.0**	**70.0**	**34.0**	**0.0**
August 20th	Climate Avg	5.17	22.2	28.5	17.5	31.4	42.0	20.9	0.0
	Climate Std Dev	3.16	2.8	3.3	2.8	5.4	8.0	4.3	0.0
	8/20/2014	**7.69**	**19.8**	**25.6**	**16.1**	**43.0**	**51.0**	**32.0**	**0.0**
September 4th	Climate Avg	3.53	21.0	27.2	16.5	33.3	45.0	22.6	0.0
	Climate Std Dev	3.09	3.9	5.0	3.6	13.9	18.3	11.7	0.0
	9/4/2014	**7.21**	**22.8**	**29.4**	**18.3**	**34.0**	**44.0**	**23.0**	**0.0**

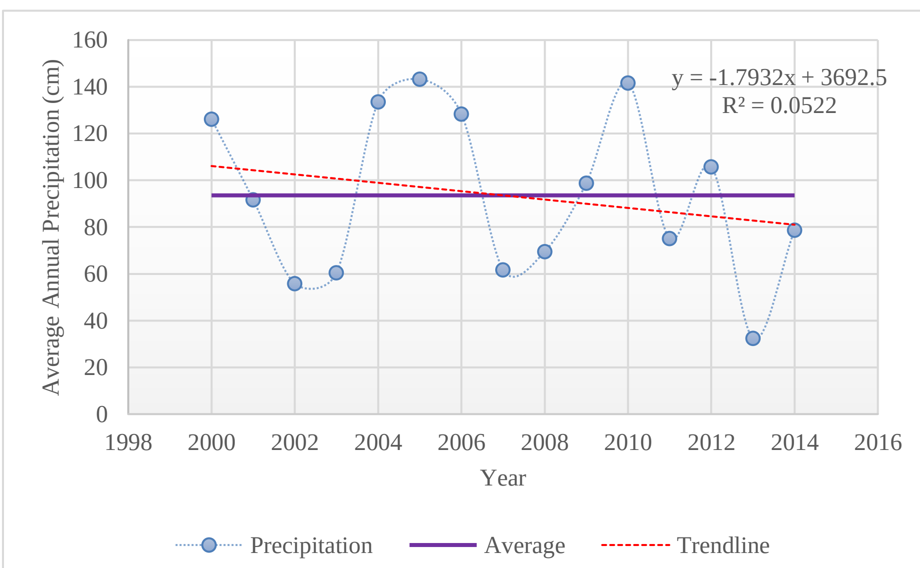

Figure 42: **Annual precipitation averages from the Mount Elizabeth weather station.**

Further utilizing this Mount Elizabeth data, it was of interest to also explore the relationship between Twain Harte Rock's temperature deviation from the 16-year climate average and AE activity. That is, if the rock surface temperature is much hotter or colder than the typical average daily temperature, will AE activity peak? This will address influences of relative temperature extremities on the recorded subsurface deformation. This comparison resulted in seemingly little correlation, however the three sensors with the most activity (Channel 1, Channel 2 and Channel 4) peaked when the temperature difference between Twain Harte Rock and the 16-year average was low/zero (Figure 43). To paint a clearer picture of the distribution of each individual sensor, AE occurrences were placed into buckets based on the standard deviation from the 16-year average daily temperature (Figure 44). If events are occurring at random in the context of temperature, then approximately 32% of events should fall outside of one standard deviation from average temperature for that day. Channels 2 and 3 were the only sensors to experience disproportioned events during weather outside the limits of standard deviation.

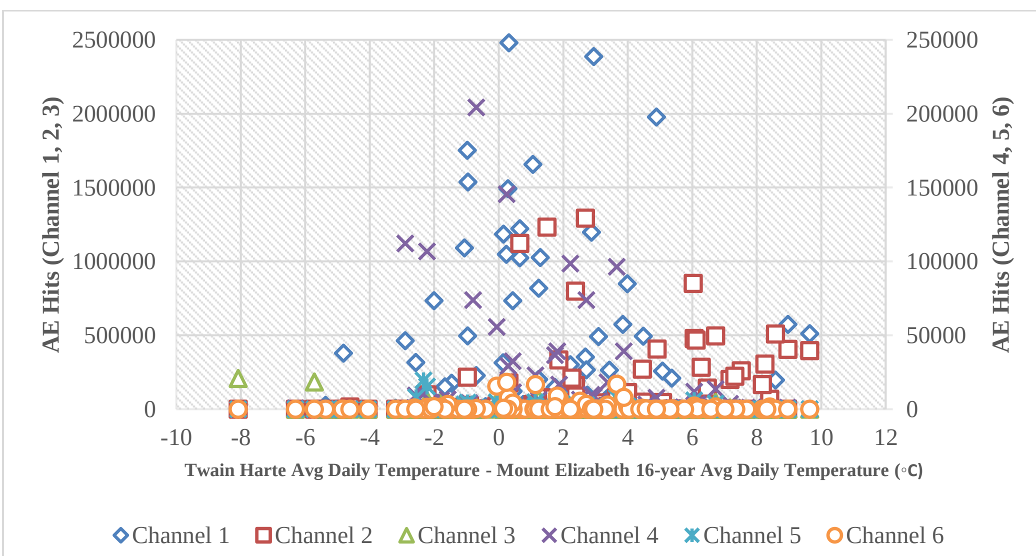

Figure 43: **Acoustic emission activity in relation to TH Rock relative temperature extremities.**

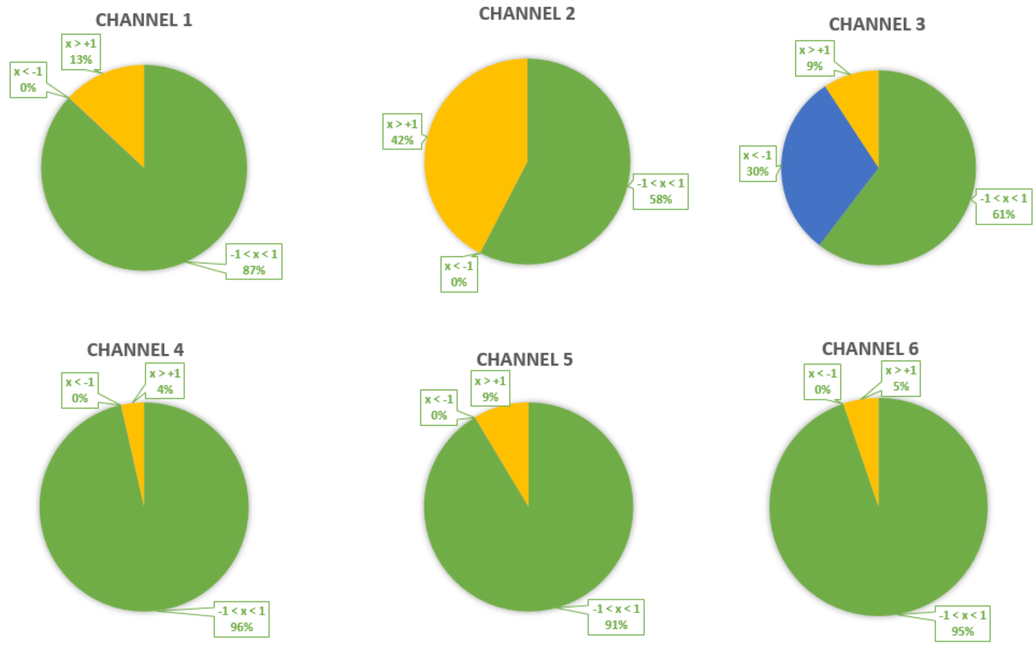

Figure 44: **AE activity and the standard deviation from 16-year average daily temperature.**

Due to the engineering activity and construction to repair the dam, the AE and temperature sensors were only deployed from October 2014 through March 2015, which is the colder part of the year. As can be seen in Figure 45, total AE hits and average monthly temperature had an almost inverse relationship. AE activity was lowest in October, rapidly increasing to peak activity in January. Then, AE hits decreased again from February to March. This is exactly correlative with the monthly average temperatures – with December and January being the coldest months during that period. From this, it is apparent that more intense temperatures (those outside the limits of +/- one standard deviation) increase the amount of crack activity overall. To ensure that this is the case, if would be necessary to monitor the warmer season in this region to see if the warmer temperatures do, in fact, have similar influence on AE activity.

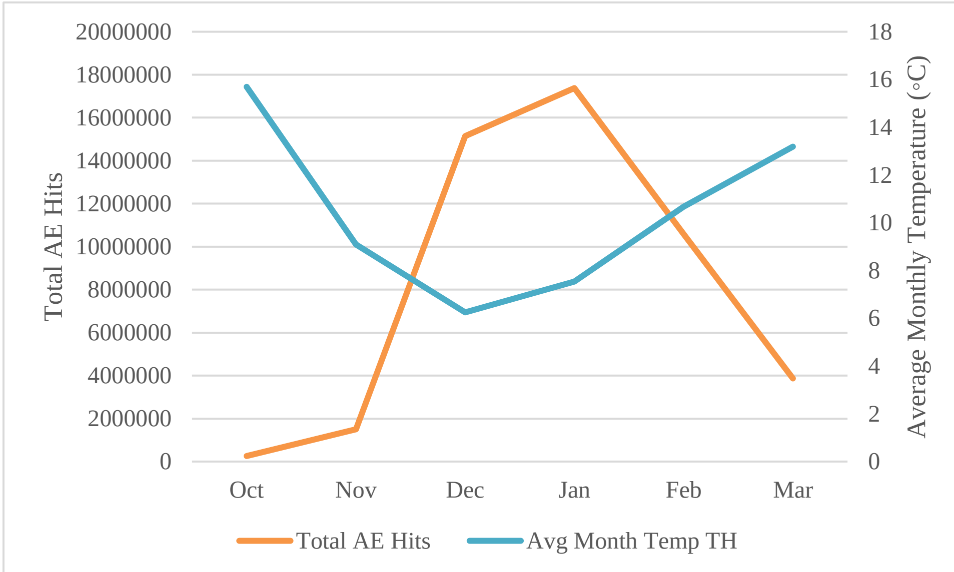

Figure 45: **The inverse relationship between AE hits and average monthly temperature during the "cold season."**

Over diurnal time scales, additional observations can be made for cracking and insolation. Figure 46 is an example of a six-day span during March, 2015. While temperature peaks (red) and light intensity (yellow) are following their daily predictable cycles, crack deformation (black) is emulating the same form. Acoustic emission hits are

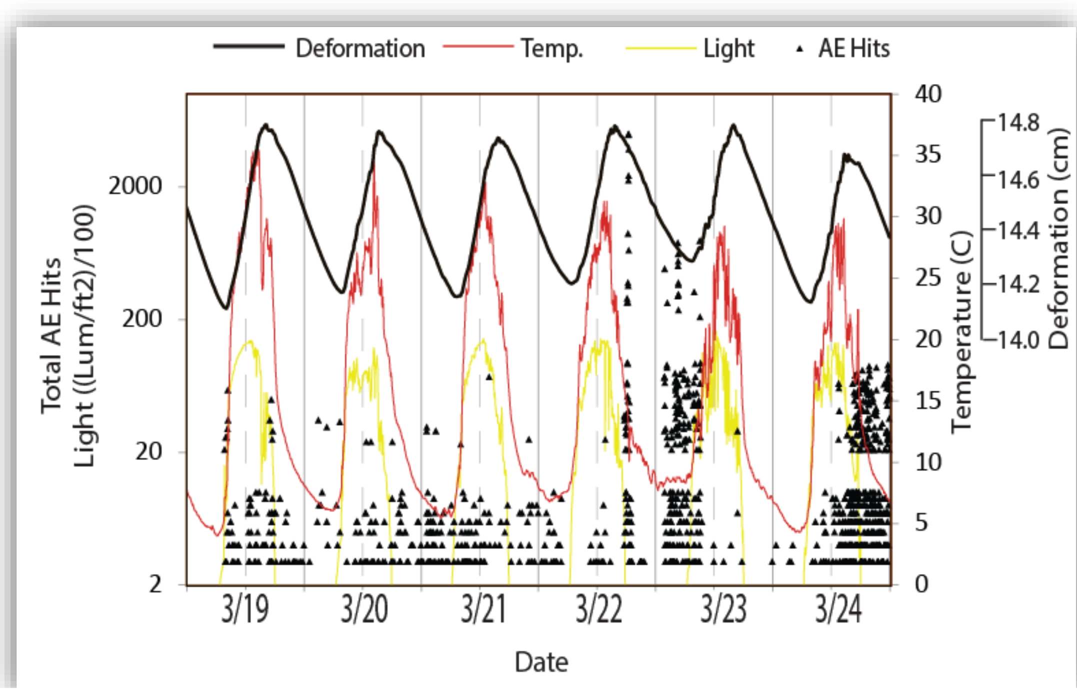

Figure 46: **Thermal influences on acoustic emission.** Crack deformation (represented by the black, solid line) is occurring with temperature change peaks (in red) and light intensity (in yellow).

primarily showing that times of peak cracking are occurring around sunrise and sunset (if the linear background noise below twenty is ignored). Importantly, sunrise and sunset have been suggested by other studies (i.e. Eppes et al., 2016) to be times of peak stresses associated with solar thermal cycling.

From surveying the domes around the study area, it is now understood that there are long-term exfoliation slabs and short-term exfoliation spalls. Being that thermal cycling has been addressed here in a variety of different scales (i.e. daily, monthly, seasonally), it was of interest to understand which degree of thermal cycling is affecting which scale of exfoliation. A general penetration depth of the diurnal cycle was calculated using the following equation:

Equation 5: **Thermal penetration depth**

$$\text{thermal penetration depth} = \sqrt{\text{diffusivity} \times \text{period}}$$

where the diffusivity of granite/gneiss is 7.24E-7 m^2/s (Eppelbaum et al., 2014) and the period is one day (a.k.a. 86,400 seconds). The result is that the diurnal thermal cycle can penetrate to approximately 25 centimeters, which correlates with the characteristic slab thickness (Figure 27).

Overall, the acoustic emission data provide strong evidence that cracking is related, at least in part, to thermal stresses arising in Twain Harte Rock and its exfoliation slabs. In this case, these data have been interpreted as reflecting cracking events due to both thermal-related stresses and the settling of the exfoliated slab due to temperature. For example, Channels 2 and 3 were both placed on the underlying dome, below the slab that was loosened by the 2014 exfoliation events. Thus, these sensors may be reflecting stresses due to overall heating of the dome surface like the measurements made on cliff-face slabs at Yosemite National Park (Collins and Stock, 2016). Channels 4 and 6 were placed next to the terminations of vertical cracks that cut the 2014 slab near where it rolls over to a more vertical orientation. Consequently, the increases in AE activity during the cold weather might reflect the cooling and associated settling of the slab that extended those fractures. Channel 1 was located closest to where the slab ruptured again in 2016. Therefore, its activity recorded in 2014/2015 might reflect precursor microcracking leading into the newest exfoliation event.

CONCLUSIONS AND IMPLICATONS

The morphology of exfoliation slabs and domes in the Twain Harte region provides insight into the processes responsible for exfoliation sheet formation, its recurrence through time and the weathering/erosion history of exfoliated slabs. In particular, regional consistency in Schmidt hammer R-values and slab thicknesses suggest that stacked slabs represent recurring exfoliation caused by similar magnitudes and/or mechanisms of forcing over long time scales. Differences in weathering characteristics of subsequent slab generations suggest that the periodicity of these events is generally consistent assuming that the rate of mechanical weathering processes on dome surfaces is roughly constant through time. The generations of exfoliation slabs provide evidence of temporal continuity – while nearby domes suggest spatial continuity – of exfoliation processes overall in this region.

Therefore, it can be concluded that long-term (10^5) exfoliation processes are consistent through time and space in the western Sierra Nevada foothills region. Further, at least at short time scales (10^{-1}), major episodes of cracking appear to be triggered by thermal cycling. However, based on the data compiled here and the existing documentation of the cracking event, this rapid exfoliation is, as yet, unique to Twain Harte Rock. One potential possibility is that the stresses of Twain Harte Rock are just fundamentally different from the other local domes. Another could be that Twain Harte's exfoliation event is just the first of many and other future events are possible in the other nearby domes. Other events are likely given that all the other surveyed domes have evidence of recurring cracking. To understand this uniqueness, it is recommended that future research on the Twain Harte exfoliation focus on revisiting/monitoring nearby domes as well as grasping the anthropogenic influences and disruption of Twain Harte Rock's natural processes.

Finally, these data also contribute to the overall understanding of continental evolution over geologic time. Erosion of bedrock potentially limits long-term landscape evolution (i.e. Hancock and Kirwan, 2007), the understanding of which is, in turn, critical to interpreting crust and mantle deformation (i.e. Gallen et al., 2013). Further, if exfoliation can be linked to tectonic compression and surface curvature (Martel, 2011), or to climatic parameters associated with ongoing global warming, there are important implications for similar sub-surface regolith production and associated erosion processes dependent on rock break-up (i.e. Heimsath, 1997). For example, the data presented herein show that crack deformation maximizes with more intense temperatures – which suggests that bedrock erosion may increase as overall global temperatures increase. Therefore, with this insight into exfoliation periodicity at Twain Harte, we are one step closer to understanding long-term geomorphological processes. Overall, this study is one of the first to document the morphologic characteristics of exfoliation in granite domes, and provides field-based insight into the formation mechanisms of these enigmatic, but ubiquitous, landforms.

REFERENCES

Argus, D. F., Fu, Y., & Landerer, F. W. (2014). Seasonal variation in total water storage in California inferred from GPS observations of vertical land motion. *Geophysical Research Letters, 41*(6), 1971-1980. doi:dx.doi.org.librarylink.uncc.edu/10.1002/2014GL059570

Bahat, D., Grossenbacher, K. A., & Karasaki, K. (1998). Mechanism of exfoliation joint formation in granitic rocks, Yosemite National Park. *Journal of Structural Geology, 21*(1), 85-96. doi:10.1016/S0191-8141(98)00069-8

Borsa, A. A., Agnew, D. C., & Cayan, D. R. (2014). Ongoing drought-induced uplift in the western United States. *Science, 345*(6204), 1587-1590. doi:dx.doi.org.librarylink.uncc.edu/10.1126/science.1260279

California Geological Survey. (2010) *Geologic Data Map No. 6 – Fault Activity Map of California (2010)*. Retrieved from maps.conservation.ca.gov/cgs/fam/.

Collins, B. D., & Stock, G. M. (2016). Rockfall triggering by cyclic thermal stressing of exfoliation fractures. *Nature Geoscience, 9*(5), 395-400. doi:dx.doi.org.librarylink.uncc.edu/10.1038/NGEO2686

[Dotysan]. (2014, August 16). *Twain Harte Rock Exfoliating*. [Video File]. Retrieved from www.youtube.com/watch?v=yAZ1V_DJKV8.

Eppelbaum, L., Kutasov, I., & Pilchin, A. (2014). Chapter 2: Thermal properties of rocks and density of fluids. *Applied Geothermics*. Berlin Heidelberg: Springer-Verlag. doi:10.1007/978-3-642-34023-9

Eppes, M. C., Magi, B., Hallet, B., Delmelle, E., Mackenzie-Helnwein, P., Warren, K., & Swami, S. (2016). Deciphering the role of solar-induced thermal stresses in rock weathering. *Geological Society of America Bulletin, 128*(9-10), 1315-1338. doi:dx.doi.org.librarylink.uncc.edu/10.1130/B31422.1

Fossen, H. (2016). *Structural Geology*. Cambridge: Cambridge University Press. doi:doi.org/10.1017/CBO9780511777806

Gallen, S. F., Wegmann, K. W., & Bohnenstiehl, D. R. (2013). Miocene rejuvenation of topographic relief in the southern Appalachians. *GSA Today*, *23*(2), 4-10. doi:dx.doi.org.librarylink.uncc.edu/10.1130/GSATG163A.1

Gilbert, G. K. (1904). Domes and dome structure of the high sierra. *Bulletin of the Geological Society of America, 15*, 29-36. doi:dx.doi.org.librarylink.uncc.edu/10.1130/GSAB-15-29

Gillespie, A. R., & Clark, D. H. (2011). Glaciations of the Sierra Nevada, California, USA. *Developments in Quaternary Science, 15*, 447-462. doi:10.1016/B978-0-444-53447-7.00034-9

Girard, L., Beutel, J., Gruber, S., Hunziker, J., Lim, R., & Weber, S. (2012). A custom acoustic emission monitoring system for harsh environments; application to freezing-induced damage in alpine rock walls. *Geoscientific Instrumentation, Methods and Data Systems (GI), 1*(2), 155-167. doi:dx.doi.org.librarylink.uncc.edu/10.5194/gi-1-155-2012

Hancock, G., & Kirwan, M. (2007). Summit erosion rates deduced from (super 10) be; implications for relief production in the central Appalachians. *Geology (Boulder), 35*(1), 89-92. doi:dx.doi.org.librarylink.uncc.edu/10.1130/G23147A.1

Heidbach, Oliver; Rajabi, Mojtaba; Reiter, Karsten; Ziegler, Moritz; WSM Team (2016): World Stress Map Database Release 2016. GFZ Data Services. doi.org/10.5880/WSM.2016.001

Heimsath, A. M., Dietrich, W. E., Nishiizumi, K., & Finkel, R. C. (1997). The soil production function and landscape equilibrium. *Nature (London), 388*(6640), 358-361. doi:10.1038/41056

Holzhausen, G. R. (1989). Origin of sheet structure; 1, morphology and boundary conditions. *Engineering Geology, 27*(1-4), 225-278. doi:10.1016/0013-7952(89)90035-5

Jain, S. (2014). *Fundamentals of physical geology*. New Delhi: Springer. doi:10.1007/978-81-322-1539-4

Leith, K., Moore, J. R., Amann, F., & Loew, S. (2014). In situ stress control on microcrack generation and macroscopic extensional fracture in exhuming bedrock. *Journal of Geophysical Research: Solid Earth*, *119*(1), 594-615. doi:dx.doi.org.librarylink.uncc.edu/10.1002/2012JB009801

Martel, S. J. (2006). Effect of topographic curvature on near-surface stresses and application to sheeting joints. *Geophysical Research Letters, 33*(1), 5. doi:dx.doi.org.librarylink.uncc.edu/10.1029/2005GL024710

Martel, S. J. (2011). Mechanics of curved surfaces, with application to surface-parallel cracks. *Geophysical Research Letters*, *38*(20), Citation L20303. doi:dx.doi.org.librarylink.uncc.edu/10.1029/2011GL049354

Moses, C., Robinson, D., & Barlow, J. (2014). Methods for measuring rock surface weathering and erosion; a critical review. *Earth-Science Reviews, 135,* 141-161. doi:dx.doi.org.librarylink.uncc.edu/10.1016/j.earscirev.2014.04.006

Plummer, C. C., Carlson, D. H., Hammersley, L. (2016). *Physical geology*. New York, NY: McGraw-Hill/Education, Inc.

Shlemon, R. J., Horner, T., & Florsheim, J. (2000). *Quaternary Geology of the Sacramento area: Guidebook for field trip, 25 March 2000 – Association of Engineering Geologists, Sacramento Section* [PDF file]. Retrieved from www.csus.edu/indiv/h/hornert/geologic%20maps%20and%20references/shlemon_horner_florsheim_2000_aeg_field_trip.pdf.

State of California – California Natural Resources Agency – Department of Water Resources – Division of Safety of Dams. (2016). *Jurisdictional Dams* [PDF file]. Retrieved from www.water.ca.gov/damsafety/docs/Jurisdictional2016.pdf.

Stock, G. M., Martel, S. J., Collins, B. D., & Harp, E. L. (2012). Progressive failure of sheeted rock slopes; the 2009-2010 rhombus wall rock falls in Yosemite Valley, California, USA. *Earth Surface Processes and Landforms, 37*(5), 546-561. doi:dx.doi.org.librarylink.uncc.edu/10.1002/esp.3192

Tarbuck, E. J., Lutgens, F. K., & Tasa, D. (2016). *Earth: an introduction to physical geology*. Boston, MA: Prentice Hall.

Terry, R. D., & Chilingar, G. V. (1955). Summary of "concerning some additional aids in studying sedimentary formations," by M. S. Shvetsov. *Journal of Sedimentary Petrology, 25*(3), 229-234. doi:10.1306/74D70466-2B21-11D7-8648000102C1865D

Twain Harte Lake Association. (2016, July 22). *History*. Retrieved from www.thlake.org/history/.

Wakasa, S., Matsuzaki, H., Tanaka, Y., & Matsukura, Y. (2006). Estimation of episodic exfoliation rates of rock sheets on a granite dome in Korea from cosmogenic nuclide analysis. *Earth Surface Processes and Landforms, 31*(10), 1246-1256. doi:dx.doi.org.librarylink.uncc.edu/10.1002/esp.1328

Warren, K., Eppes, M. C., Swami, S., Garbini, J., & Putkonen, J. (2013). Automated field detection of rock fracturing, microclimate, and diurnal rock temperature and strain fields. *Geoscientific Instrumentation, Methods and Data Systems (GI), 2*(2), 275-288. doi:dx.doi.org.librarylink.uncc.edu/10.5194/gi-2-275-2013

Ziegler, M., Loew, S., & Moore, J. R. (2013). Distribution and inferred age of exfoliation joints in the Aar granite of the central Swiss Alps and relationship to quaternary landscape evolution. *Geomorphology, 201*, 344-362. doi:dx.doi.org.librarylink.uncc.edu/10.1016/j.geomorph.2013.07.010

Ziegler, M., Loew, S., & Bahat, D. (2014). Growth of exfoliation joints and near-surface stress orientations inferred from fractographic markings observed in the upper Aar valley (Swiss Alps). *Tectonophysics, 626*, 1-20. doi:dx.doi.org.librarylink.uncc.edu/10.1016/j.tecto.2014.03.017

APPENDIX A: GEOLOGIC MAP OF SACRAMENTO QUADRANGLE (1:250000)

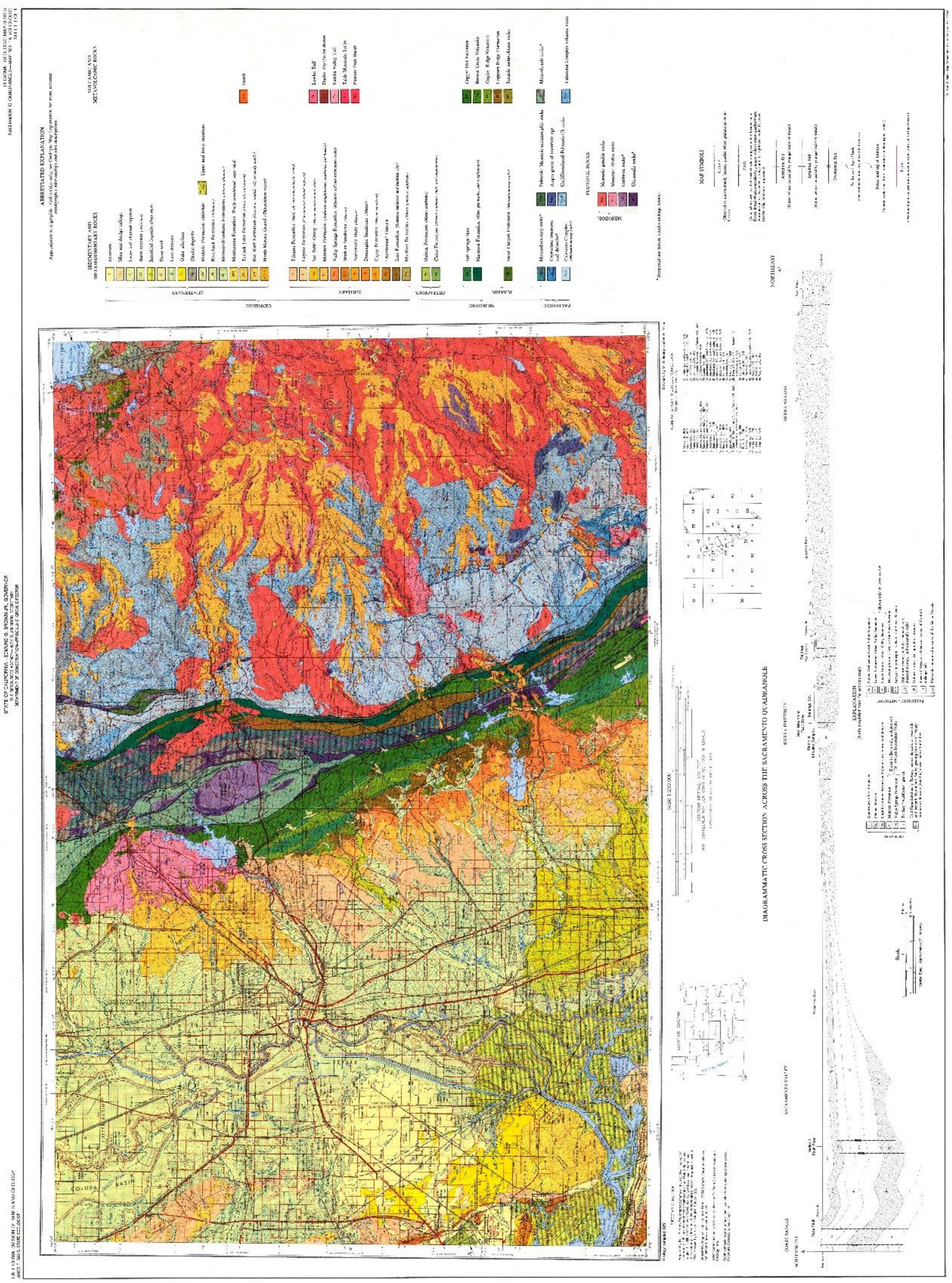

APPENDIX B: COLLECTION OF SKETCHED FIELD MAPS OF EACH SITE

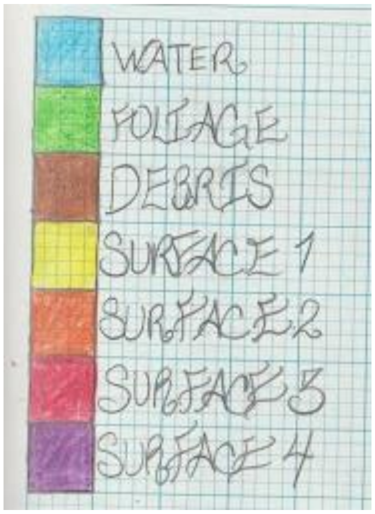

Figure B - 1: **Color key for field maps.** Indicates the different slabs ("surface" in this key) and the variety of other observed surface variables in the field map sketches.

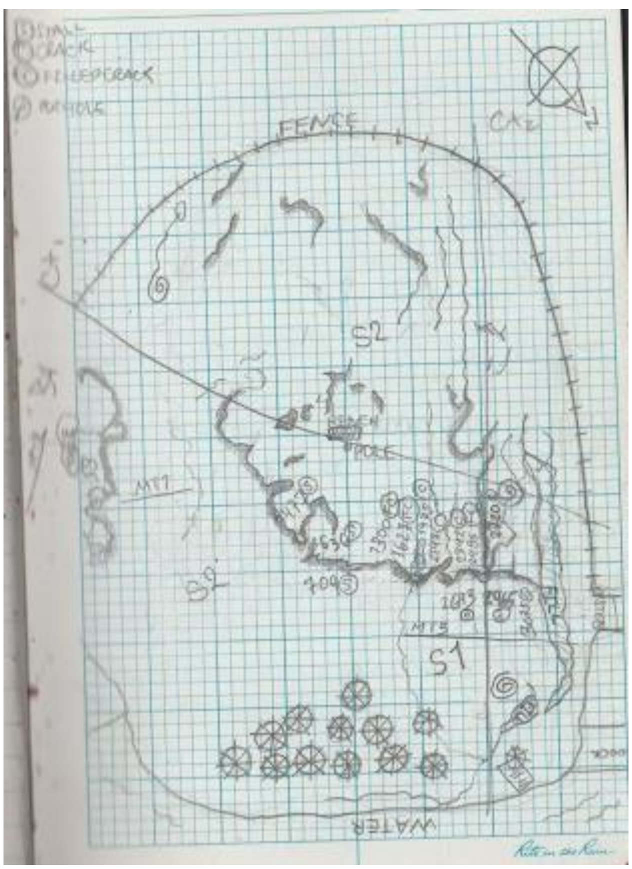

Figure B - 2: **Site 0 field sketch - Twain Harte Rock.**

Figure B - 3: **Site 1 field sketch.**

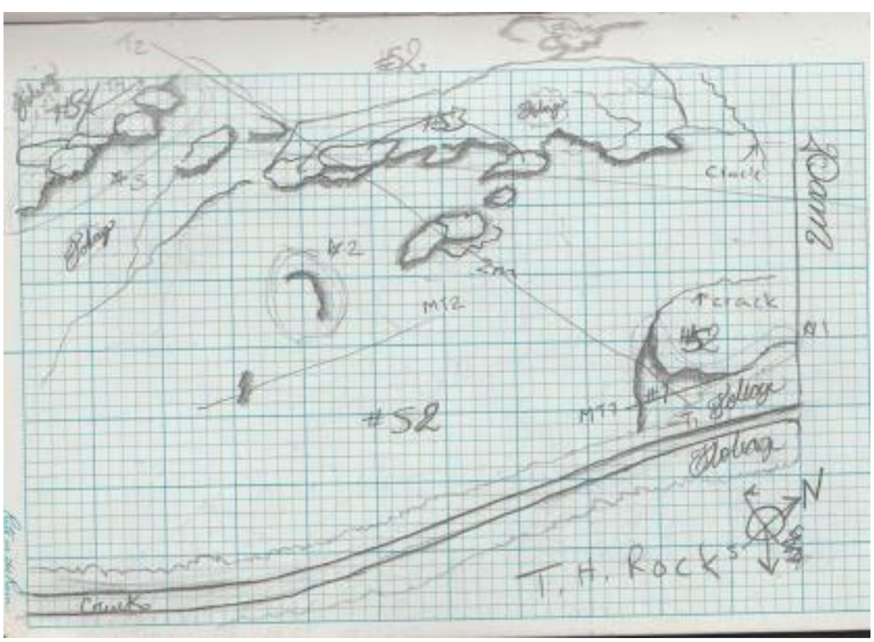

Figure B - 4: **Site 2 field sketch.**

Figure B - 6: **Site 3 field sketch.**

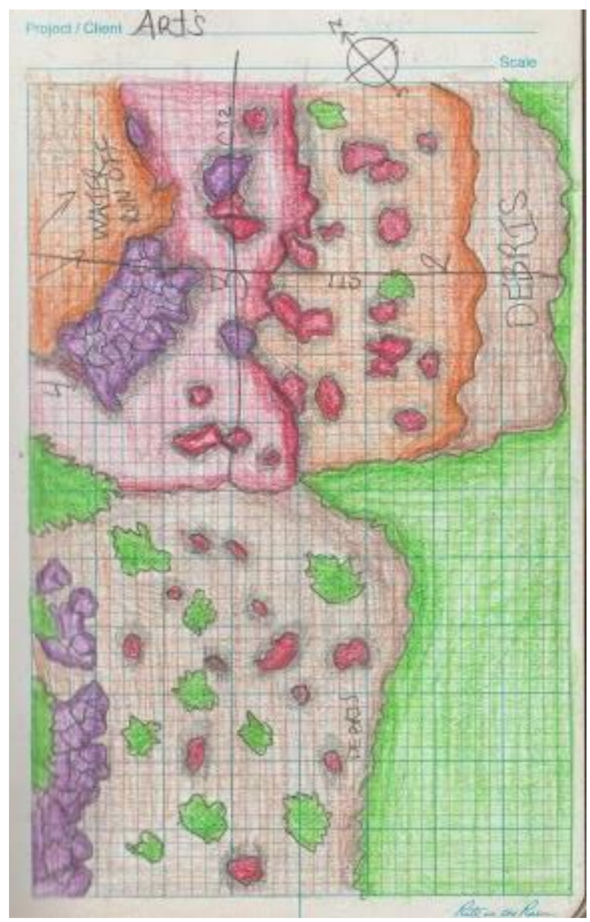

Figure B - 5: **Site 4 field sketch.**

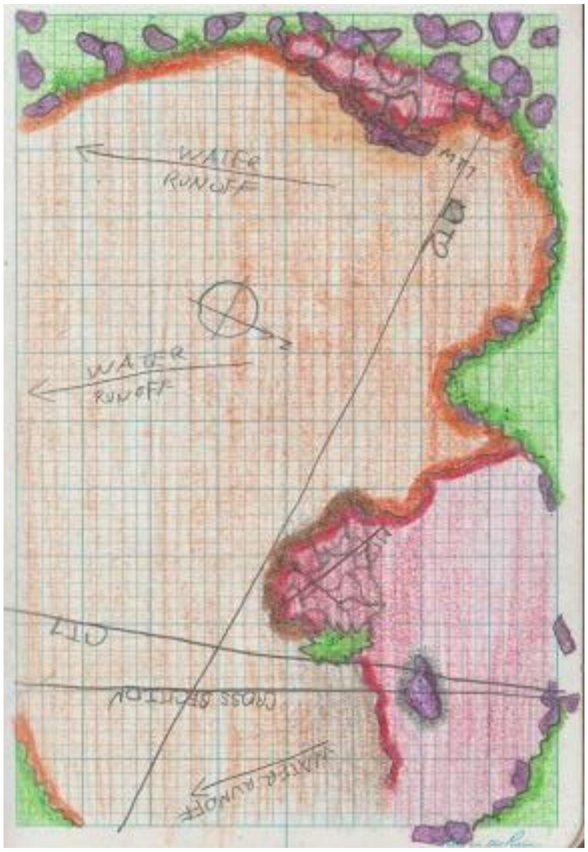

Figure B - 7: **Site 5 field sketch.**

Figure B - 8: **Site 6 field sketch.**

Figure B - 9: **Site 7 field sketch.**

Figure B - 10: **Site 8 field sketch.**

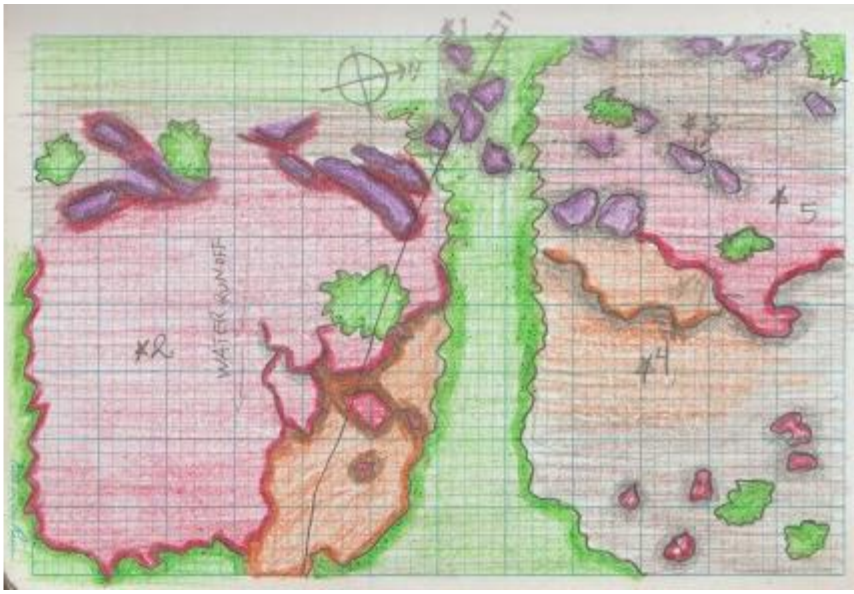

Figure B - 11: **Site 10 field sketch.**

Figure B - 12: **Site 11 field sketch.**

Figure B - 13: **Site 12 field sketch.**

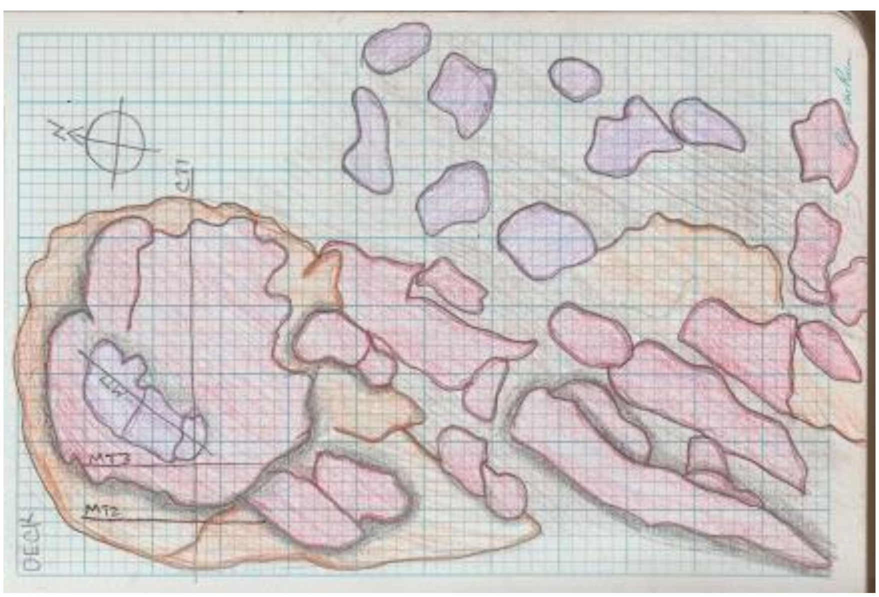

Figure B - 14: **Site 13 field sketch.**

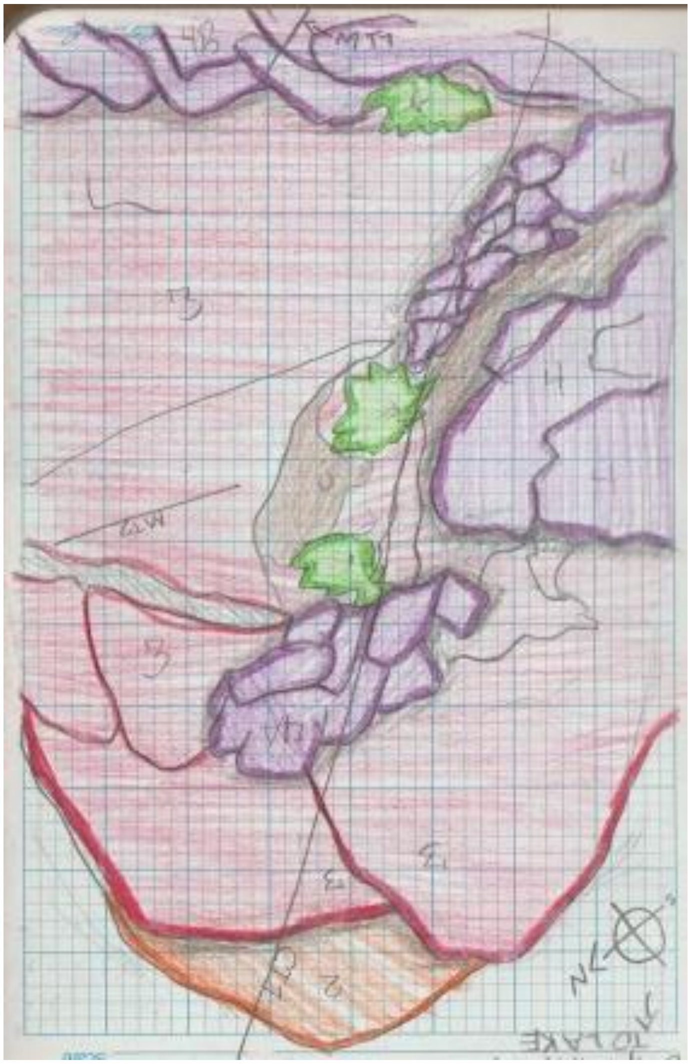

Figure B - 15: **Site 14 field sketch.**

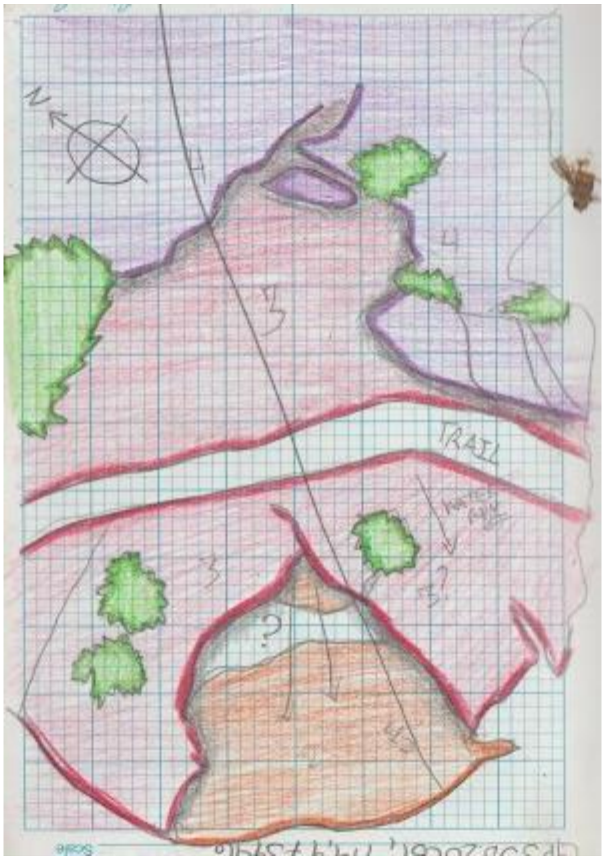

Figure B - 16: **Site 15 field sketch.**

Figure B - 17: **Site 16 field sketch**.

APPENDIX C: TOPOGRAPHIC LONGITUDINAL PROFILES OF ALL SITES

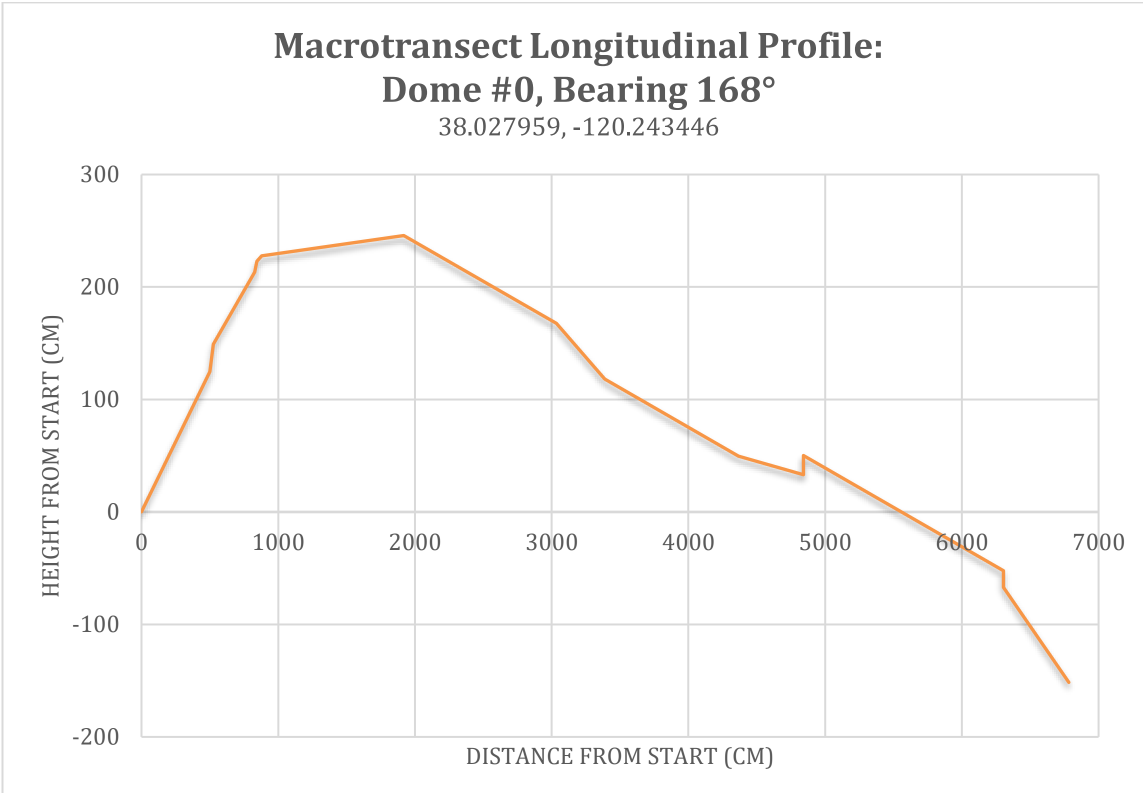

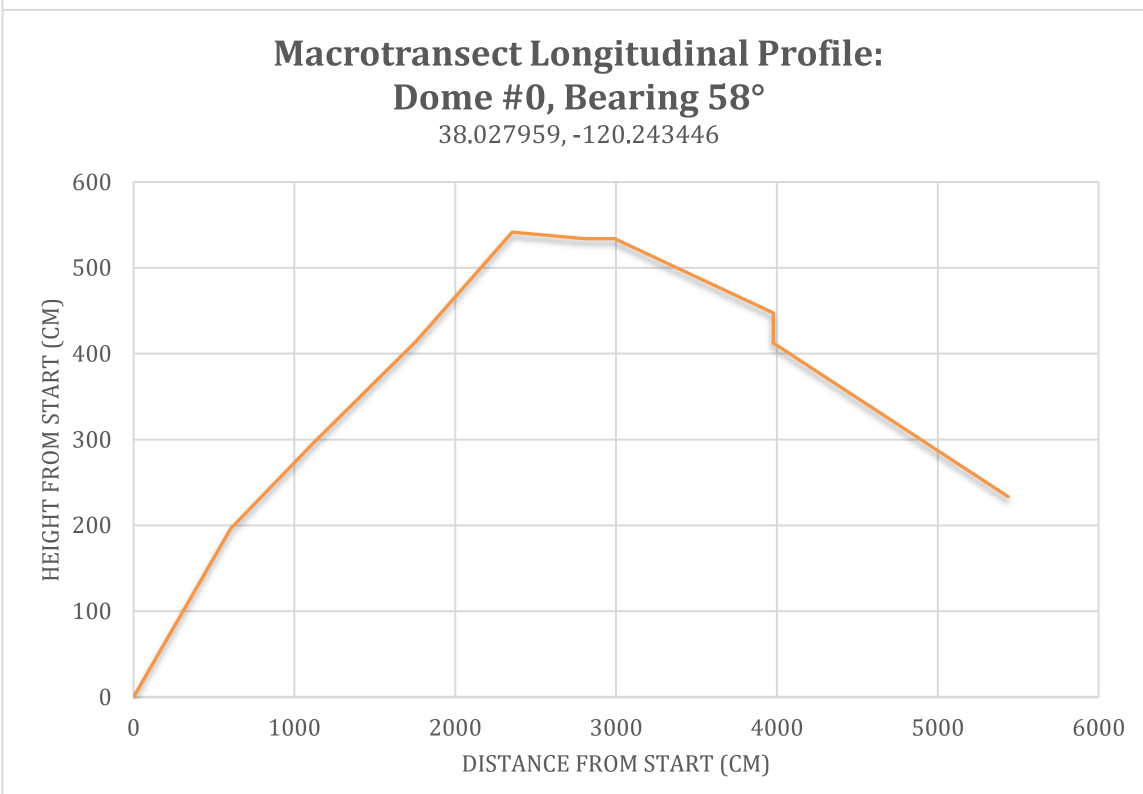

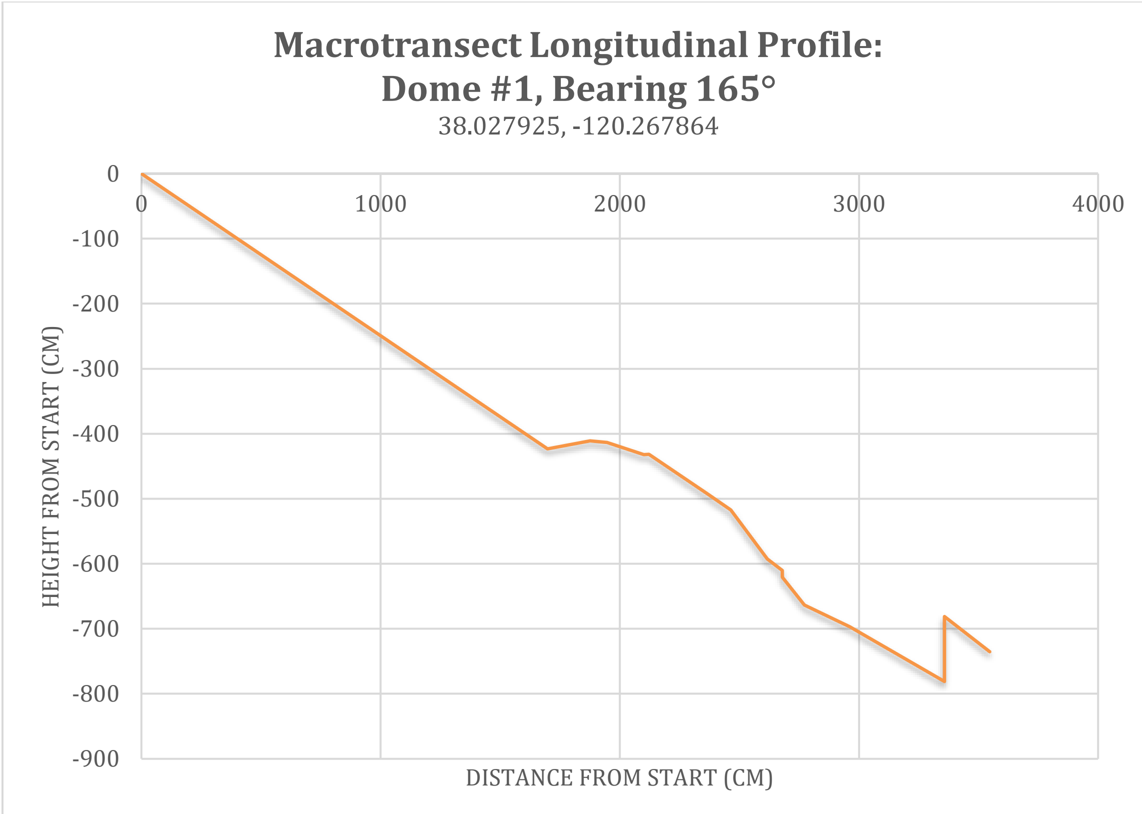
Macrotransect Longitudinal Profile:
Dome #1, Bearing 165°
38.027925, -120.267864
0
-100
-200
-300
-400
-500
-600
-700
-800
-900
0
1000
2000
3000
4000
HEIGHT FROM START (CM)
DISTANCE FROM START (CM)

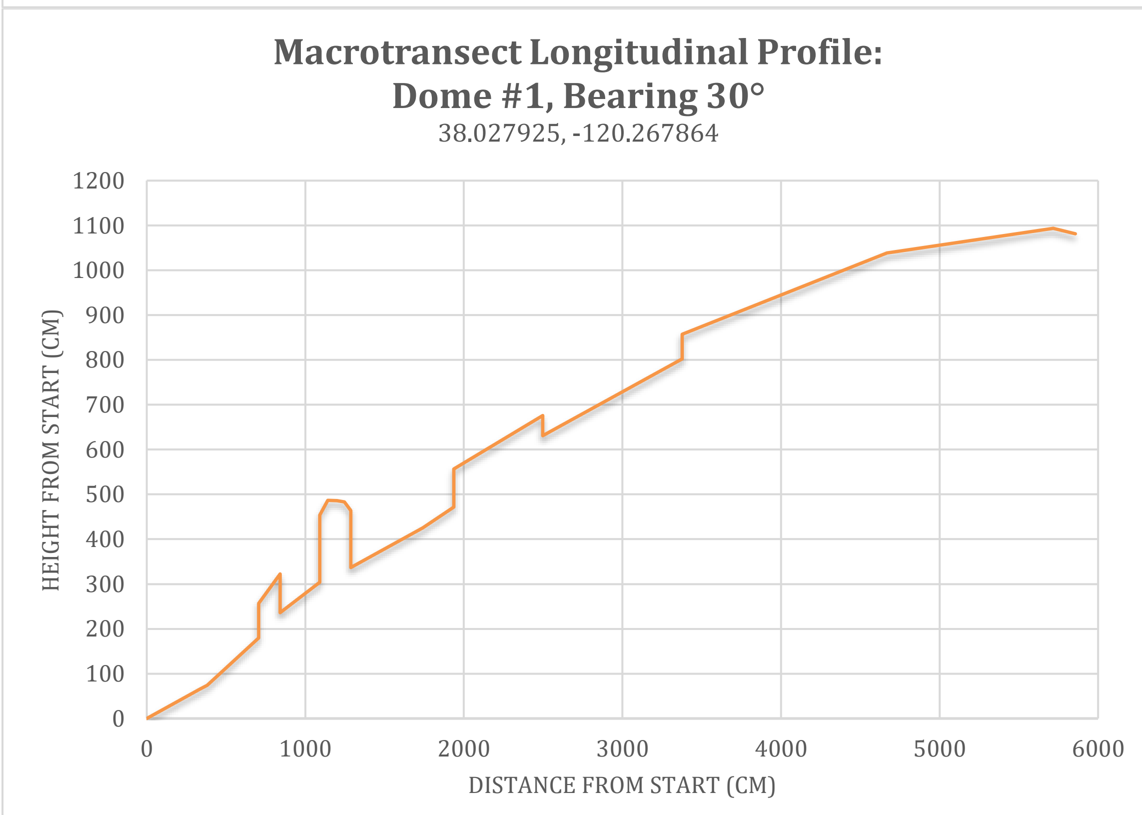
Macrotransect Longitudinal Profile:
Dome #1, Bearing 30°
38.027925, -120.267864
1200
1100
1000
900
800
700
600
500
400
300
200
100
0
0
1000
2000
3000
4000
5000
6000
HEIGHT FROM START (CM)
DISTANCE FROM START (CM)

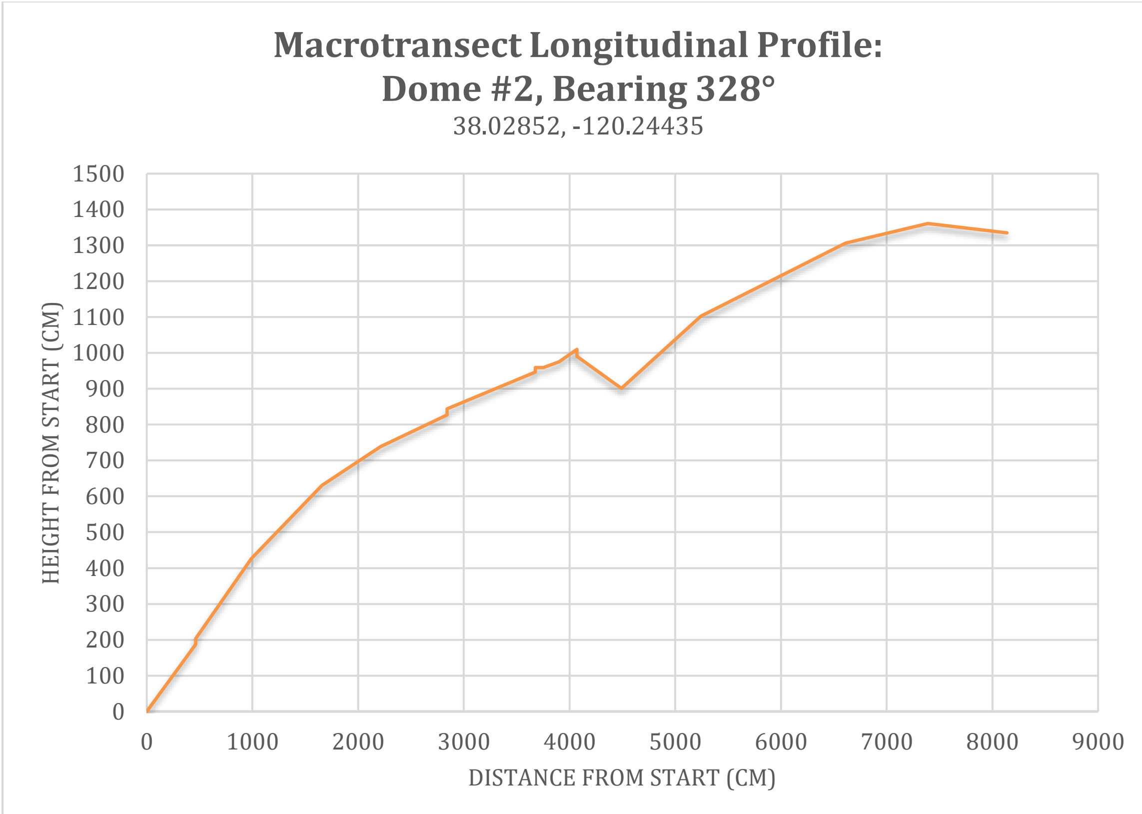
Macrotransect Longitudinal Profile:
Dome #2, Bearing 328°
38.02852, -120.24435
HEIGHT FROM START (CM)
0
100
200
300
400
500
600
700
800
900
1000
1100
1200
1300
1400
1500
0
1000
2000
3000
4000
5000
6000
7000
8000
9000
DISTANCE FROM START (CM)

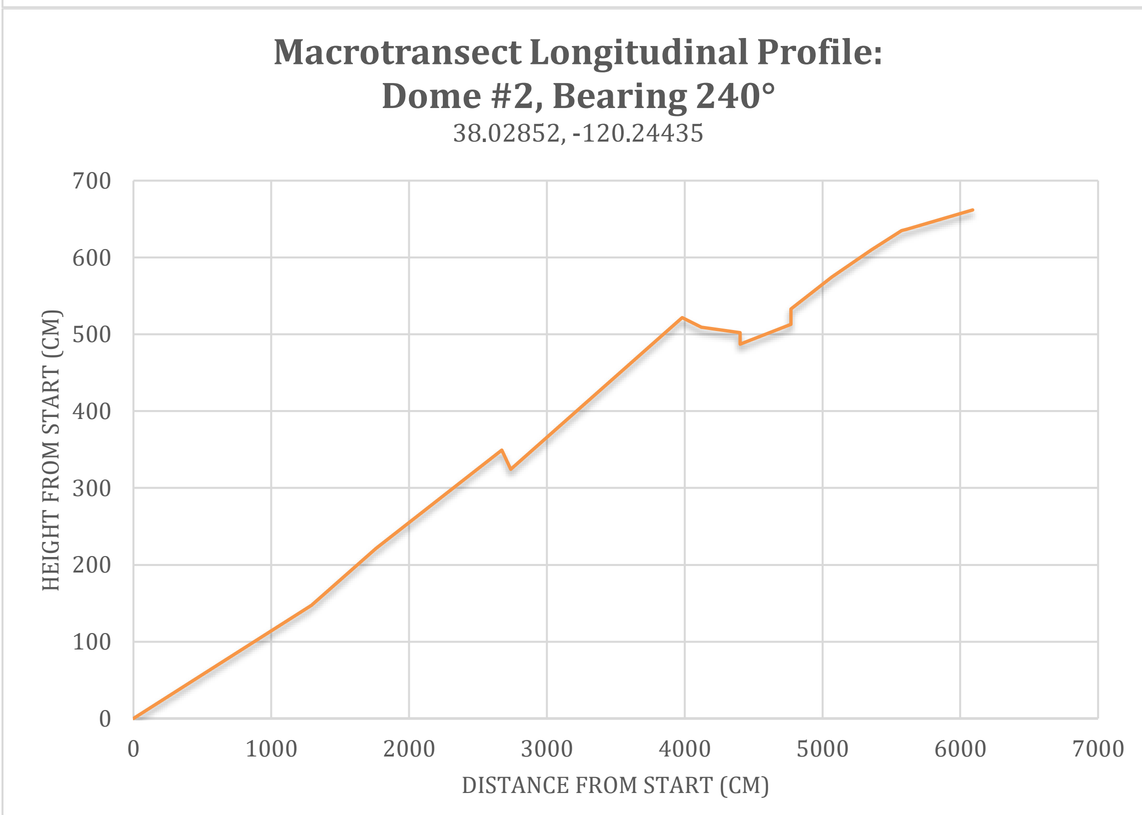
Macrotransect Longitudinal Profile:
Dome #2, Bearing 240°
38.02852, -120.24435
HEIGHT FROM START (CM)
0
100
200
300
400
500
600
700
0
1000
2000
3000
4000
5000
6000
7000
DISTANCE FROM START (CM)

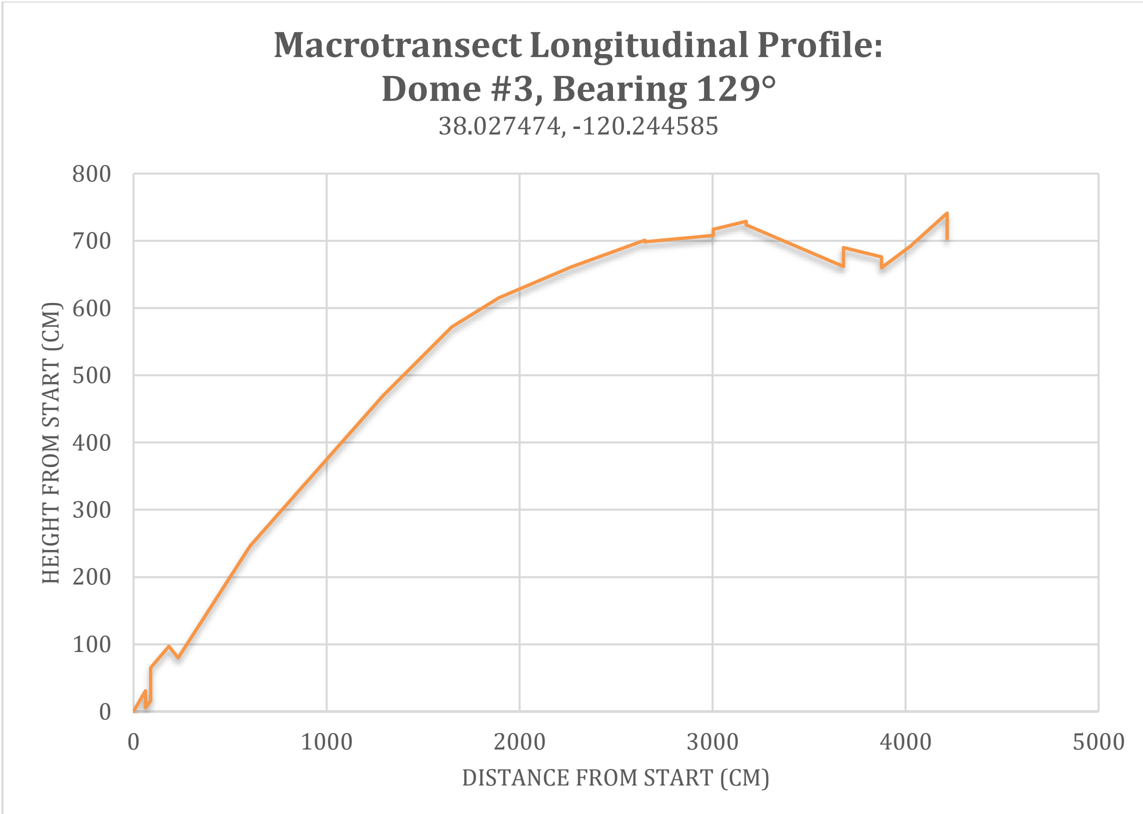
Macrotransect Longitudinal Profile:
Dome #3, Bearing 129°
38.027474, -120.244585
HEIGHT FROM START (CM)
DISTANCE FROM START (CM)
0
100
200
300
400
500
600
700
800
0
1000
2000
3000
4000
5000

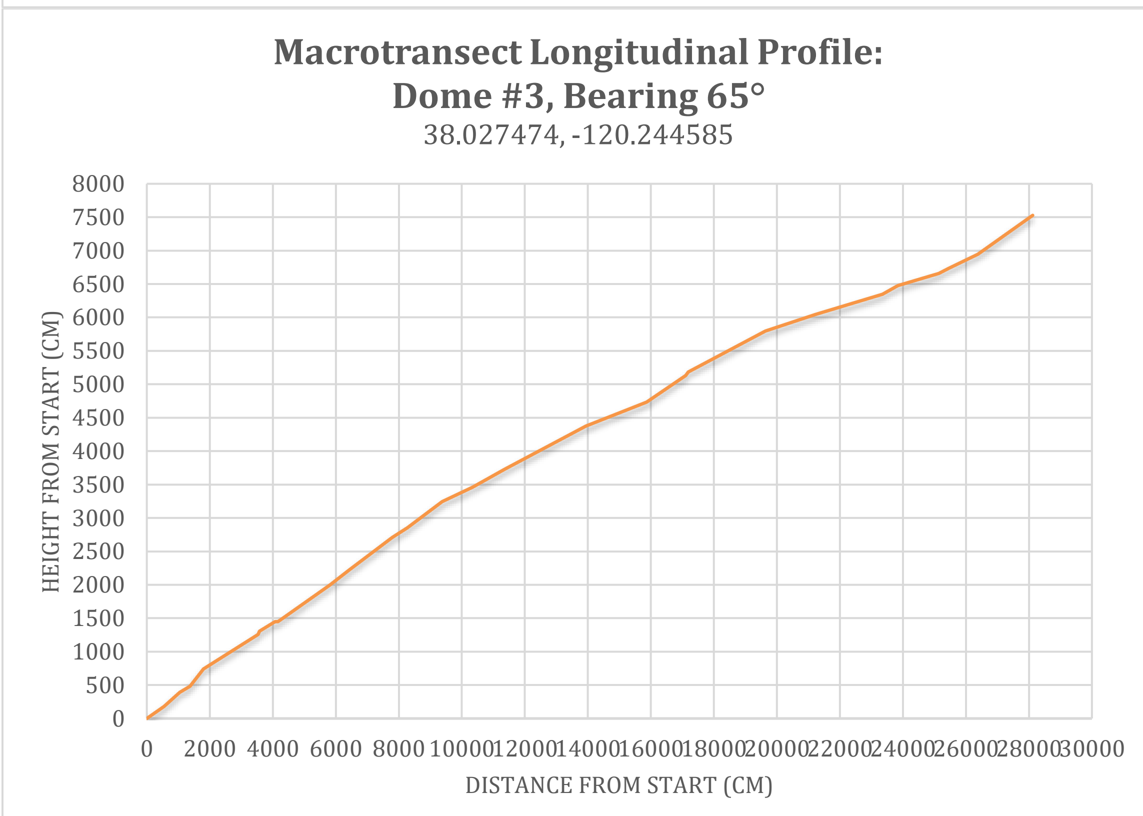
Macrotransect Longitudinal Profile:
Dome #3, Bearing 65°
38.027474, -120.244585
HEIGHT FROM START (CM)
DISTANCE FROM START (CM)
0
500
1000
1500
2000
2500
3000
3500
4000
4500
5000
5500
6000
6500
7000
7500
8000
0
2000
4000
6000
8000
10000
12000
14000
16000
18000
20000
22000
24000
26000
28000
30000

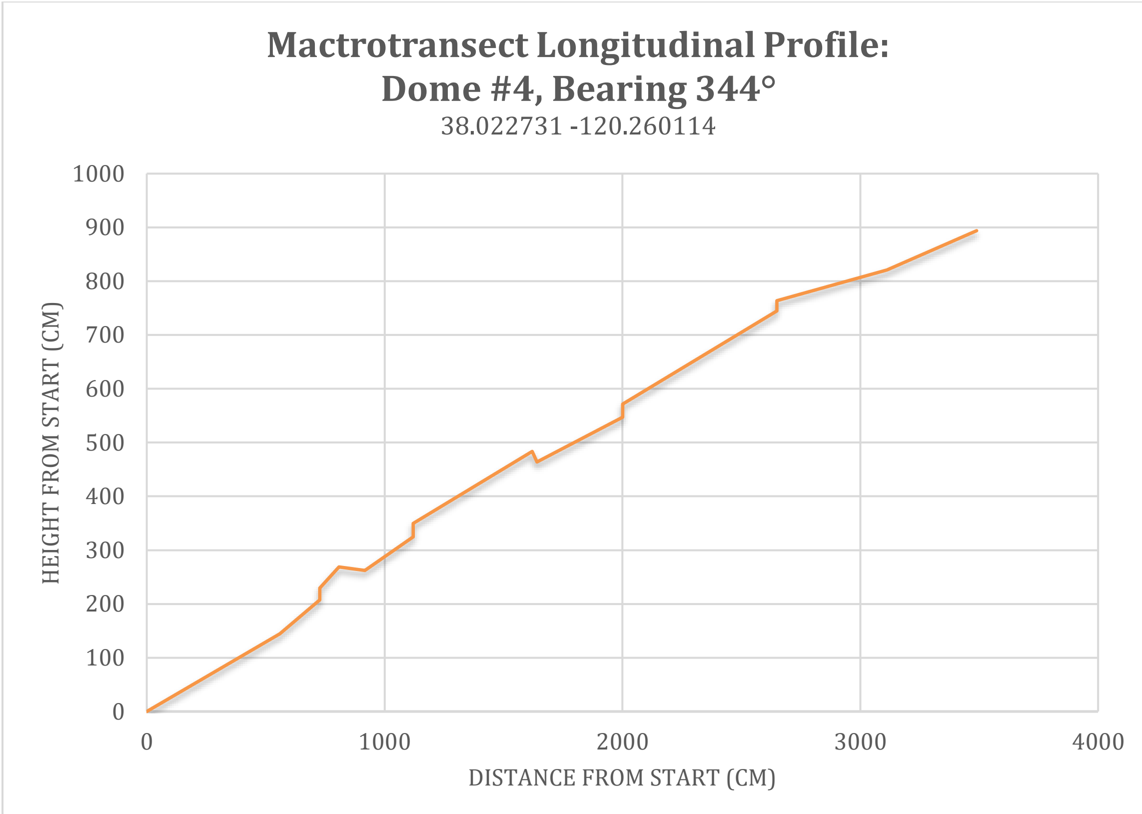
Mactrotransect Longitudinal Profile:
Dome #4, Bearing 344°
38.022731 -120.260114
HEIGHT FROM START (CM)
DISTANCE FROM START (CM)
0
100
200
300
400
500
600
700
800
900
1000
0
1000
2000
3000
4000

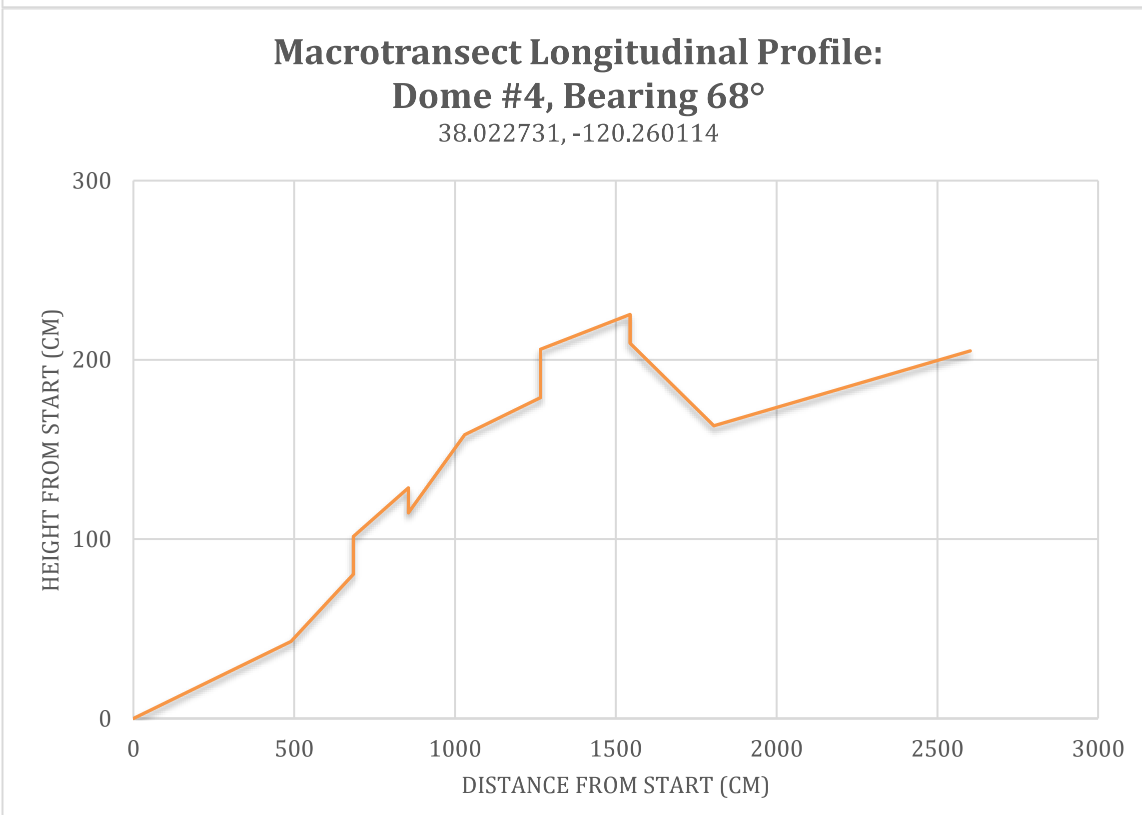
Macrotransect Longitudinal Profile:
Dome #4, Bearing 68°
38.022731, -120.260114
HEIGHT FROM START (CM)
DISTANCE FROM START (CM)
0
100
200
300
0
500
1000
1500
2000
2500
3000

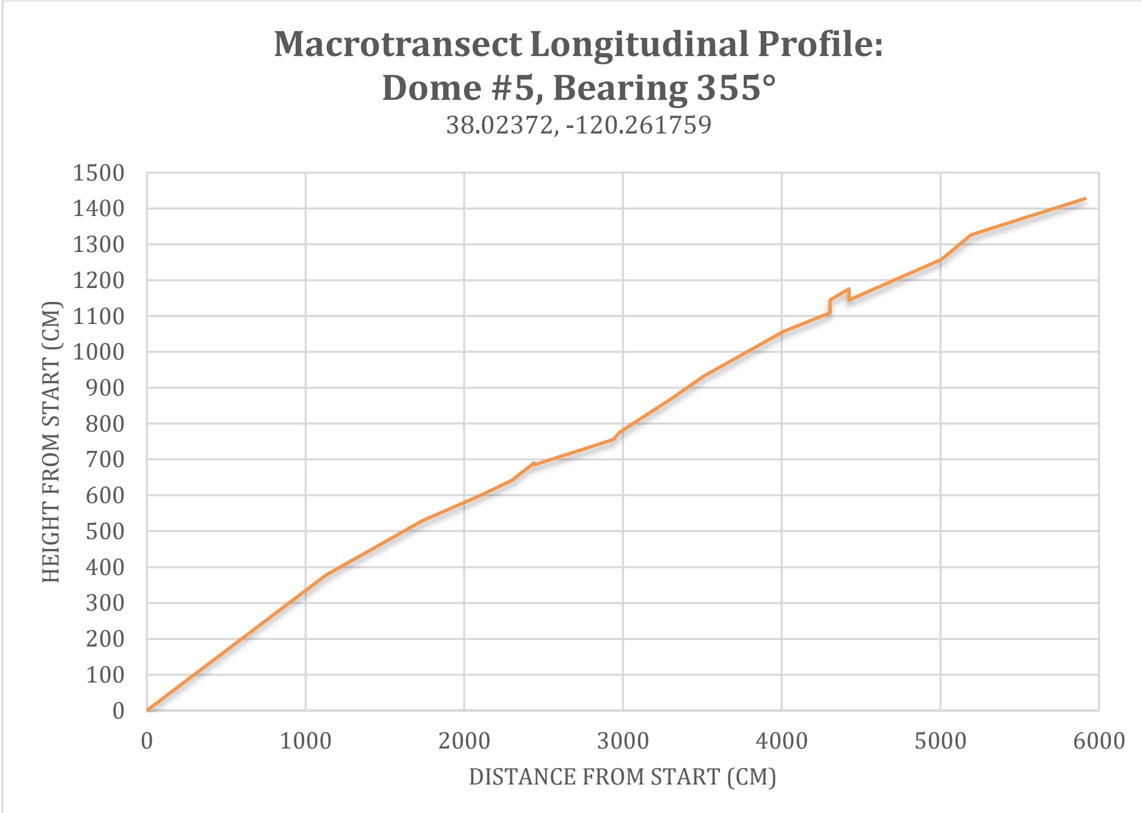
Macrotransect Longitudinal Profile:
Dome #5, Bearing 355°
38.02372, -120.261759
HEIGHT FROM START (CM)
DISTANCE FROM START (CM)
0
100
200
300
400
500
600
700
800
900
1000
1100
1200
1300
1400
1500
0
1000
2000
3000
4000
5000
6000

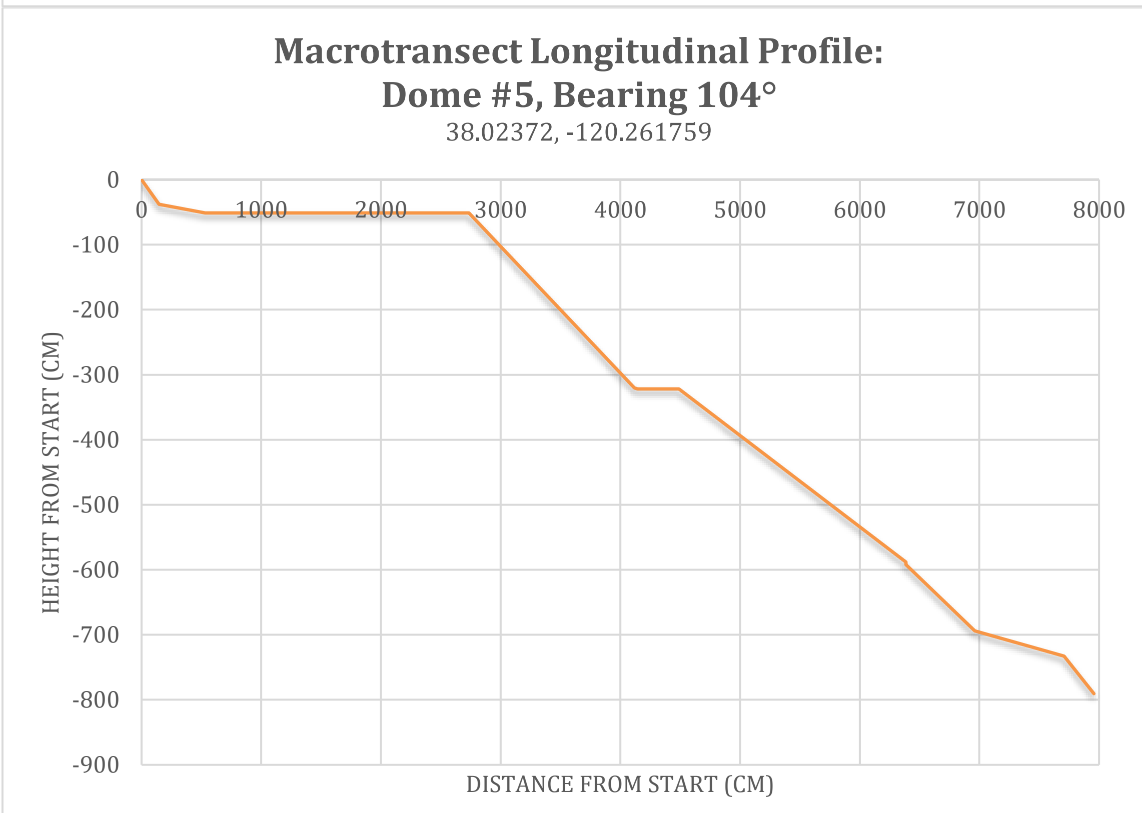
Macrotransect Longitudinal Profile:
Dome #5, Bearing 104°
38.02372, -120.261759
HEIGHT FROM START (CM)
DISTANCE FROM START (CM)
0
-100
-200
-300
-400
-500
-600
-700
-800
-900
0
1000
2000
3000
4000
5000
6000
7000
8000

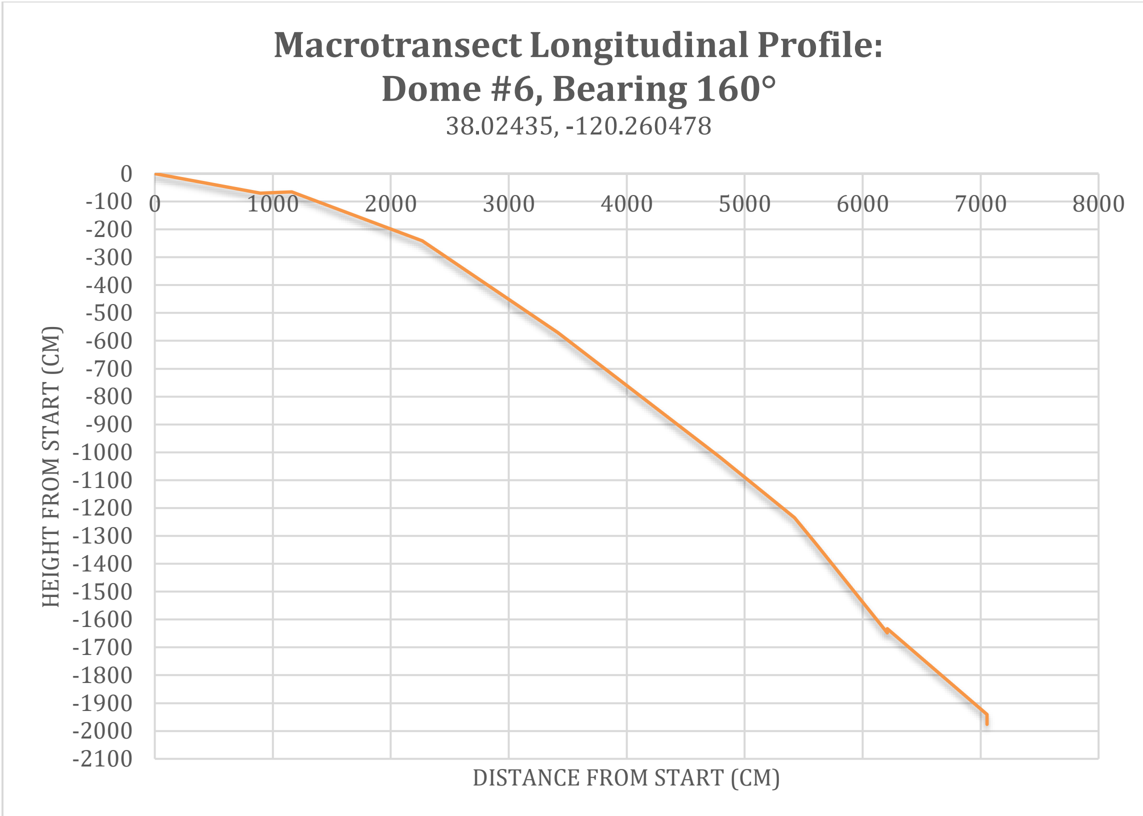
Macrotransect Longitudinal Profile:
Dome #6, Bearing 160°
38.02435, -120.260478
HEIGHT FROM START (CM)
DISTANCE FROM START (CM)
0
-100
-200
-300
-400
-500
-600
-700
-800
-900
-1000
-1100
-1200
-1300
-1400
-1500
-1600
-1700
-1800
-1900
-2000
-2100
0
1000
2000
3000
4000
5000
6000
7000
8000

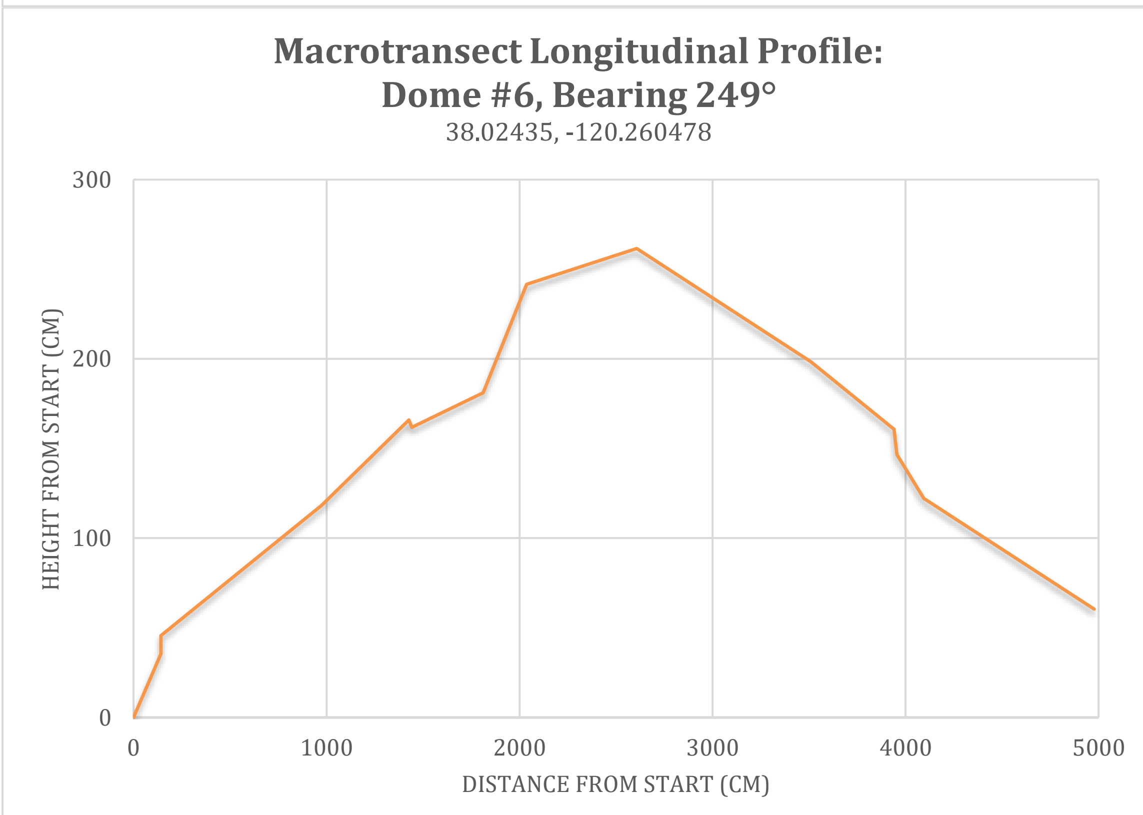
Macrotransect Longitudinal Profile:
Dome #6, Bearing 249°
38.02435, -120.260478
HEIGHT FROM START (CM)
DISTANCE FROM START (CM)
300
200
100
0
0
1000
2000
3000
4000
5000

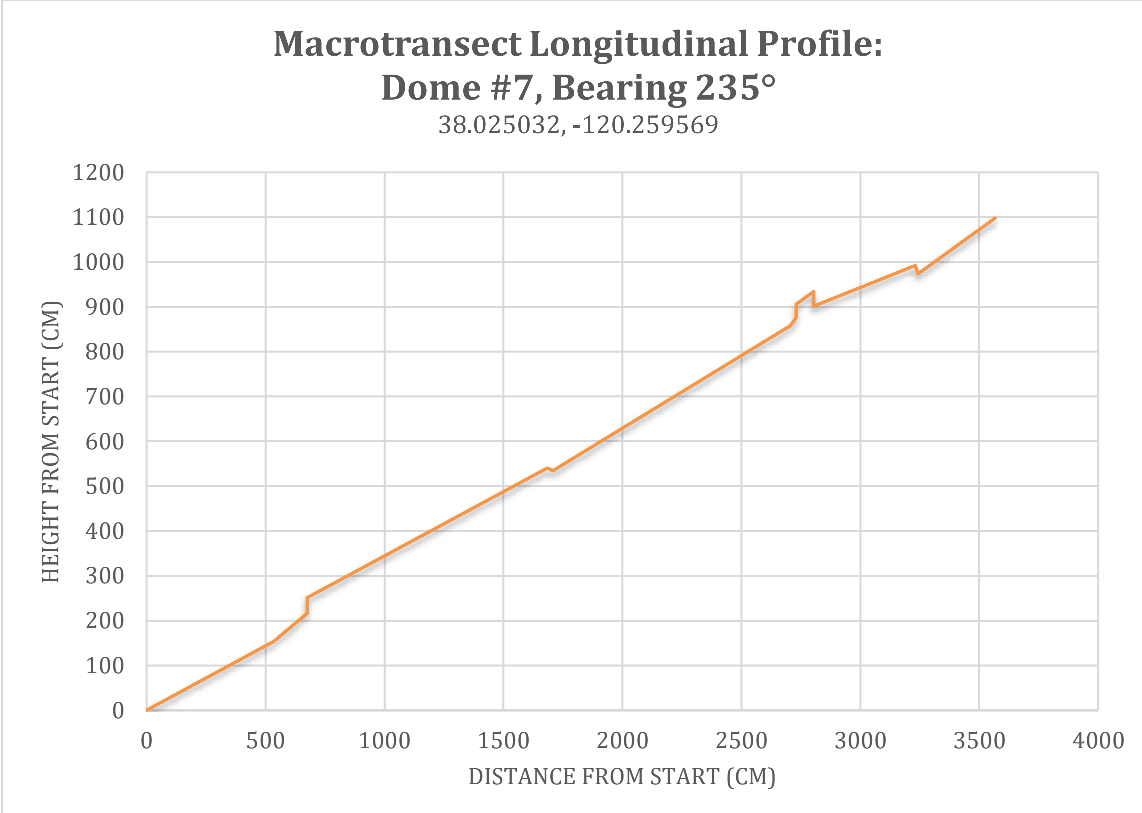
Macrotransect Longitudinal Profile:
Dome #7, Bearing 235°
38.025032, -120.259569
HEIGHT FROM START (CM)
DISTANCE FROM START (CM)
0
100
200
300
400
500
600
700
800
900
1000
1100
1200
0
500
1000
1500
2000
2500
3000
3500
4000

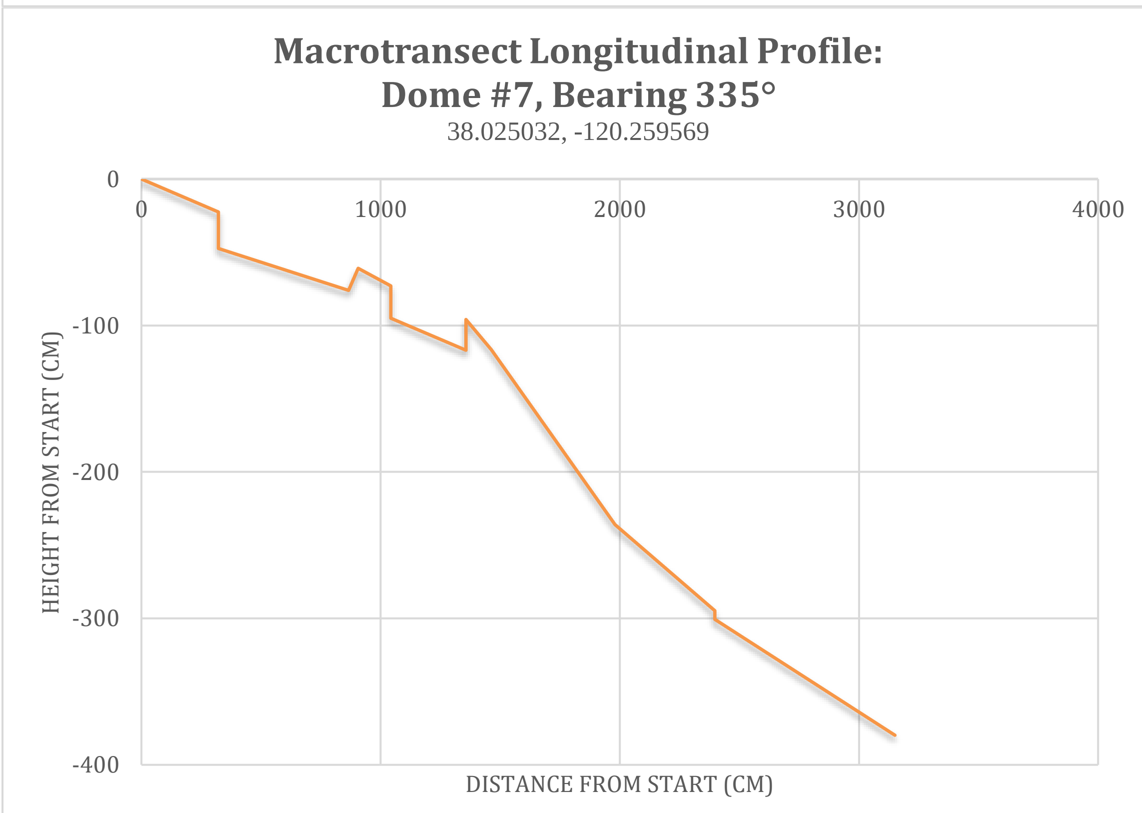
Macrotransect Longitudinal Profile:
Dome #7, Bearing 335°
38.025032, -120.259569
HEIGHT FROM START (CM)
DISTANCE FROM START (CM)
0
-100
-200
-300
-400
0
1000
2000
3000
4000

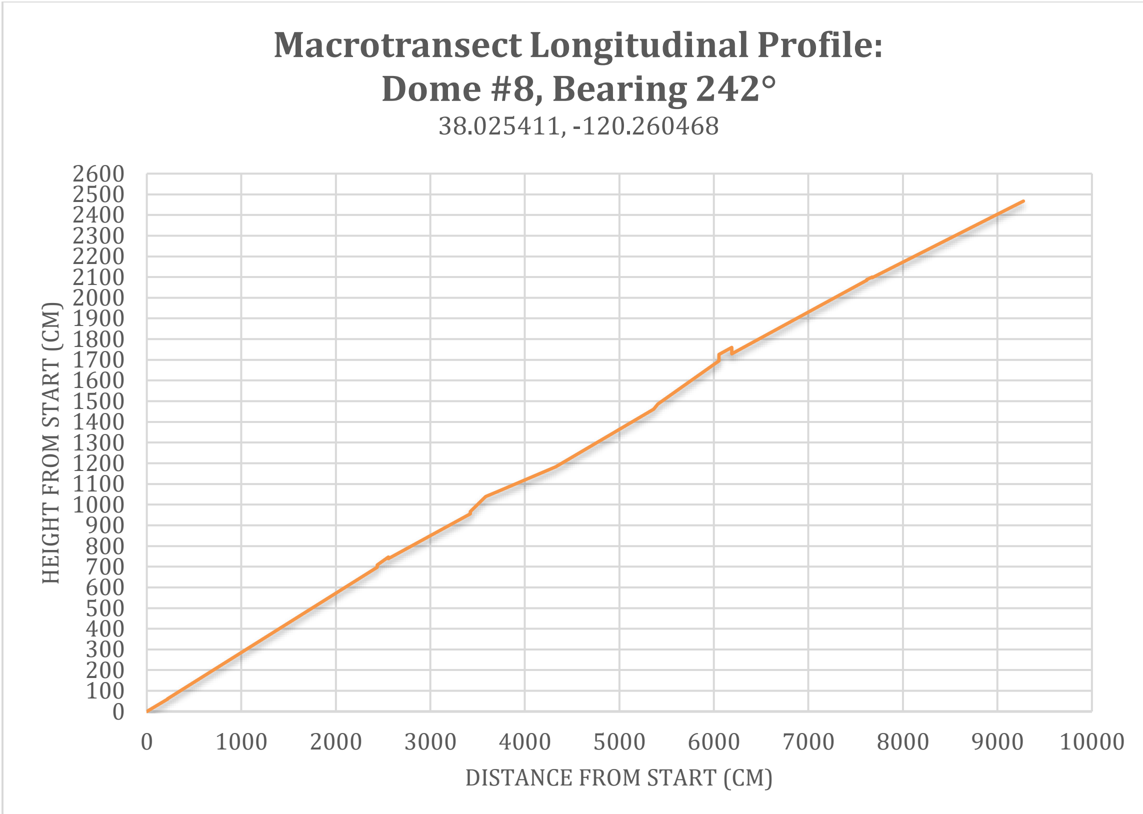
Macrotransect Longitudinal Profile:
Dome #8, Bearing 242°
38.025411, -120.260468
HEIGHT FROM START (CM)
2600
2500
2400
2300
2200
2100
2000
1900
1800
1700
1600
1500
1400
1300
1200
1100
1000
900
800
700
600
500
400
300
200
100
0
0
1000
2000
3000
4000
5000
6000
7000
8000
9000
10000
DISTANCE FROM START (CM)

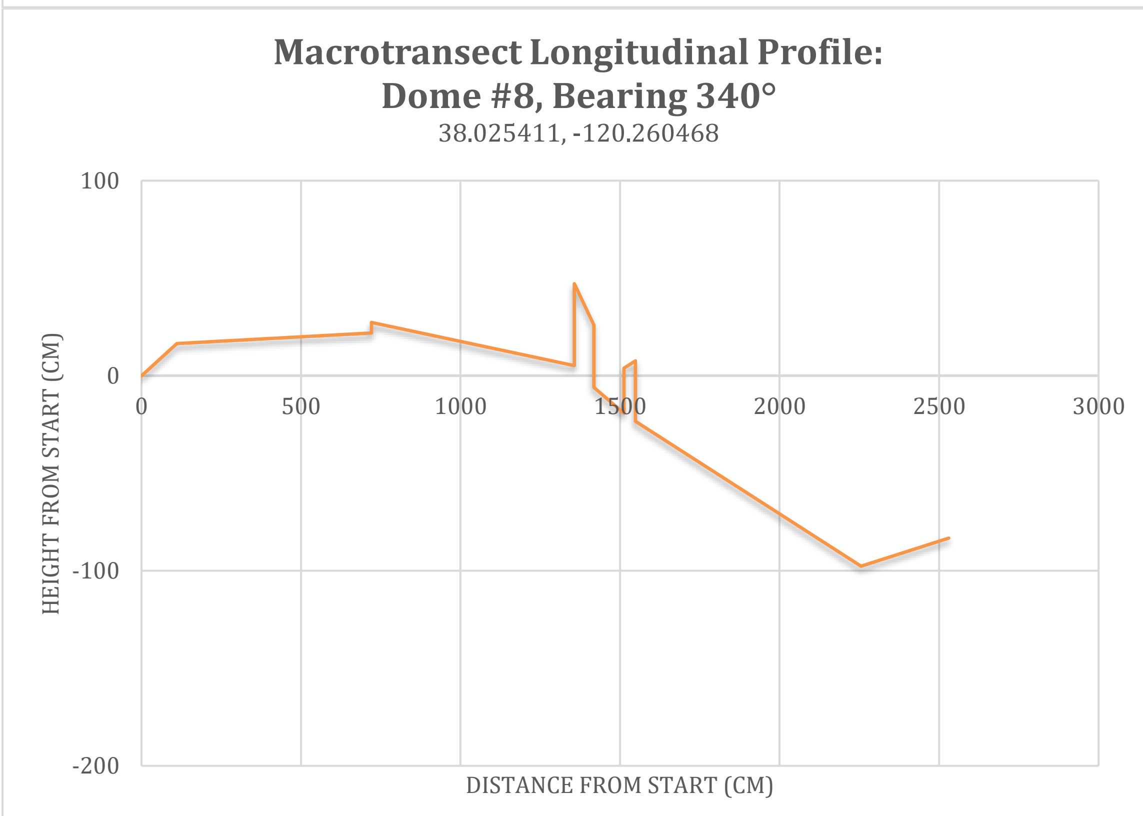
Macrotransect Longitudinal Profile:
Dome #8, Bearing 340°
38.025411, -120.260468
HEIGHT FROM START (CM)
100
0
-100
-200
0
500
1000
1500
2000
2500
3000
DISTANCE FROM START (CM)

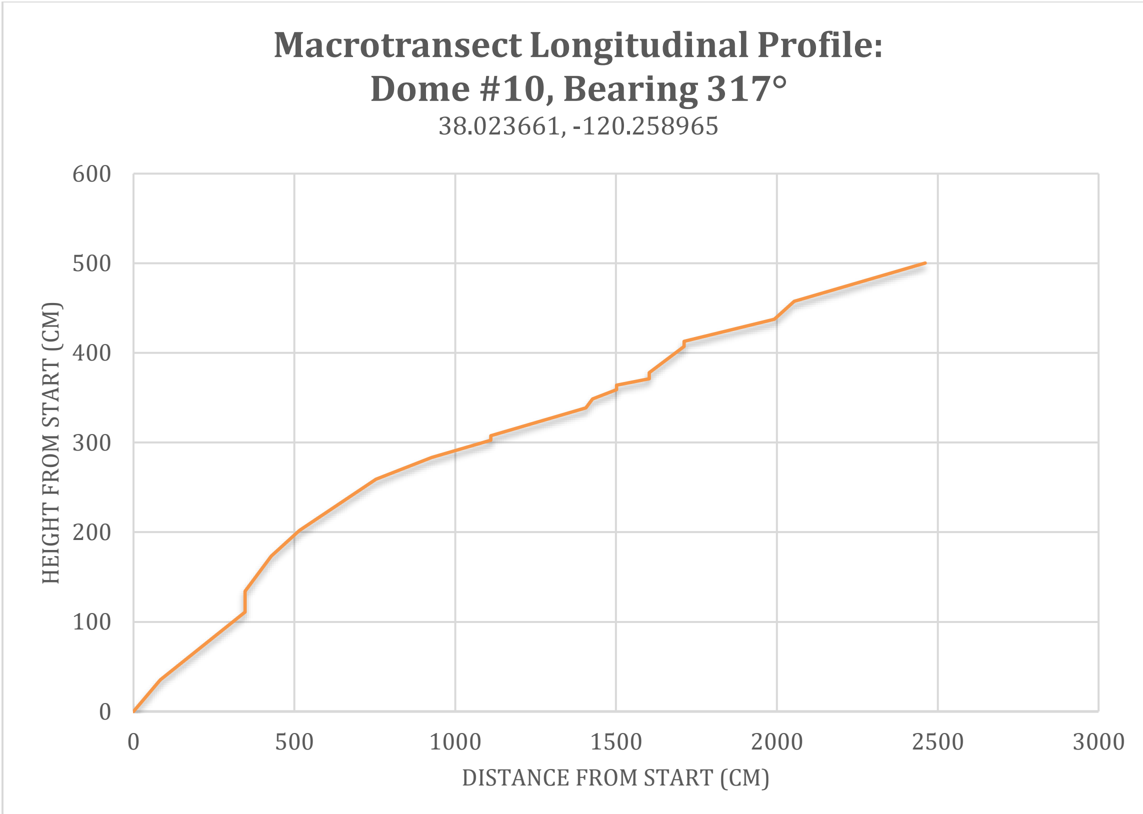

Macrotransect Longitudinal Profile:
Dome #10, Bearing 317°
38.023661, -120.258965
HEIGHT FROM START (CM)
0
100
200
300
400
500
600
0
500
1000
1500
2000
2500
3000
DISTANCE FROM START (CM)

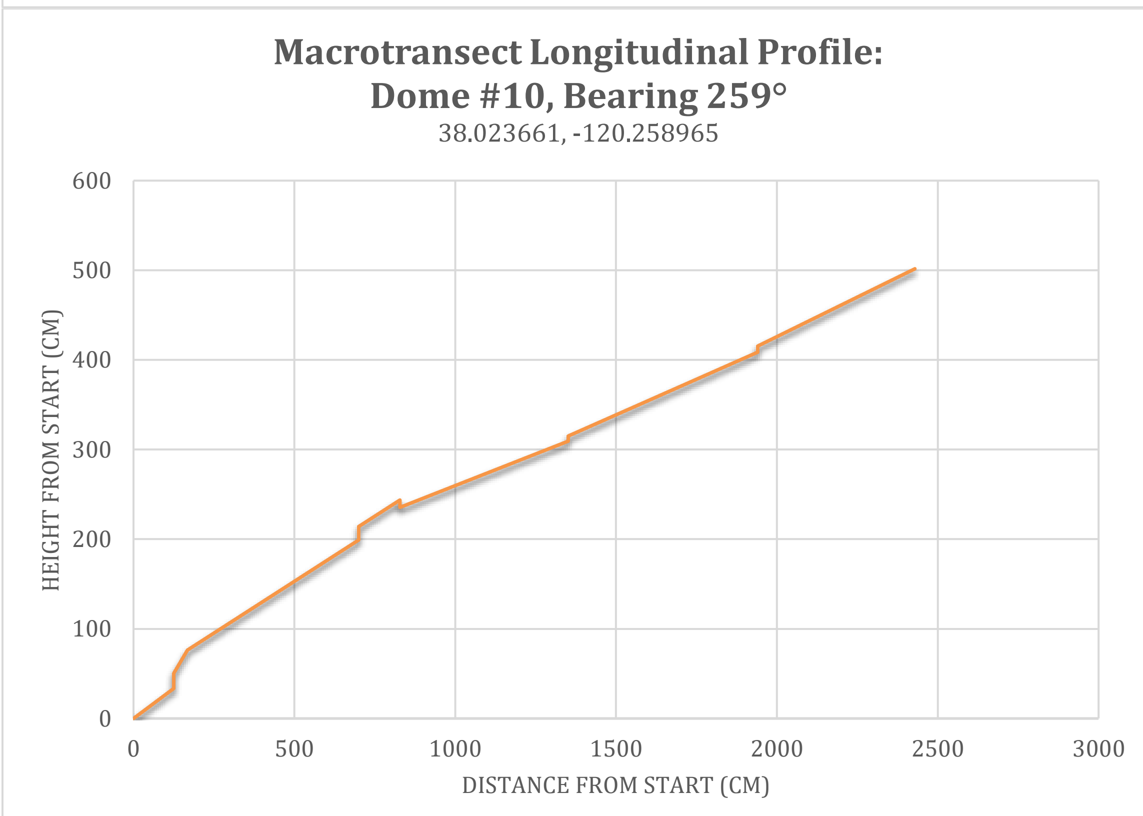

Macrotransect Longitudinal Profile:
Dome #10, Bearing 259°
38.023661, -120.258965
HEIGHT FROM START (CM)
0
100
200
300
400
500
600
0
500
1000
1500
2000
2500
3000
DISTANCE FROM START (CM)

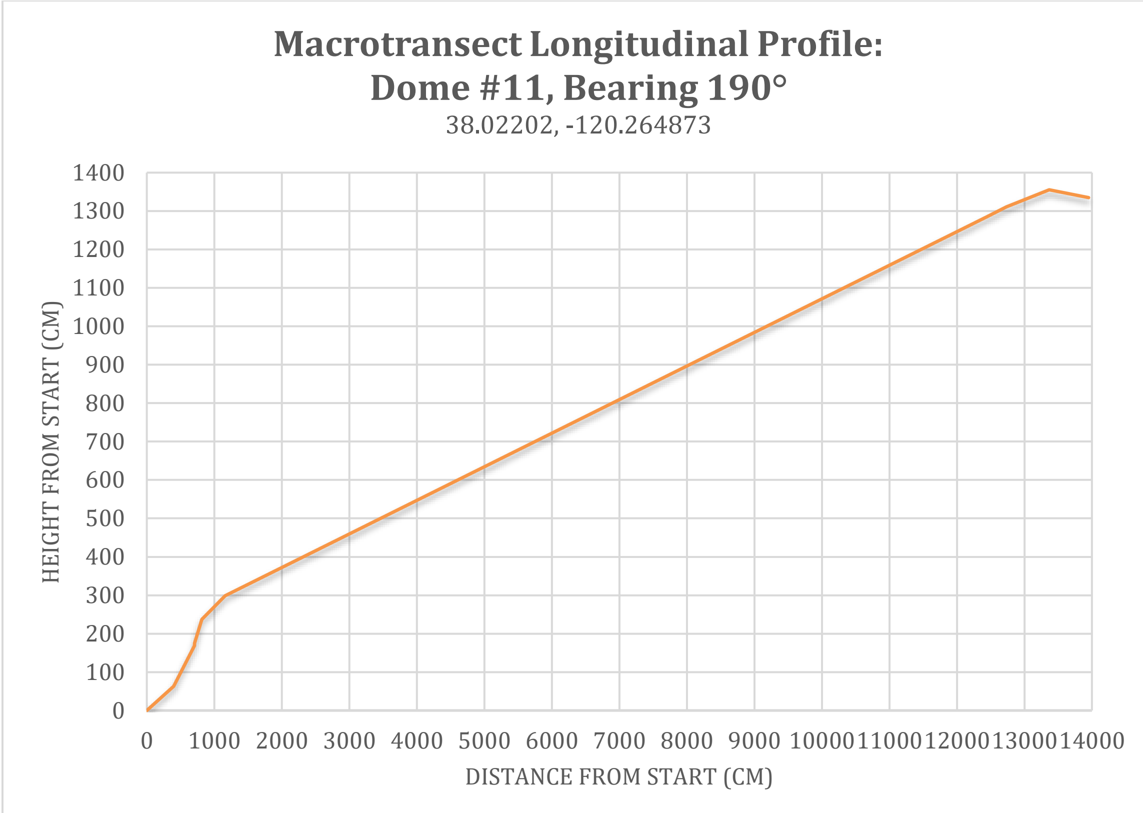
Macrotransect Longitudinal Profile:
Dome #11, Bearing 190°
38.02202, -120.264873
HEIGHT FROM START (CM)
1400
1300
1200
1100
1000
900
800
700
600
500
400
300
200
100
0
0 1000 2000 3000 4000 5000 6000 7000 8000 9000 10000 11000 12000 13000 14000
DISTANCE FROM START (CM)

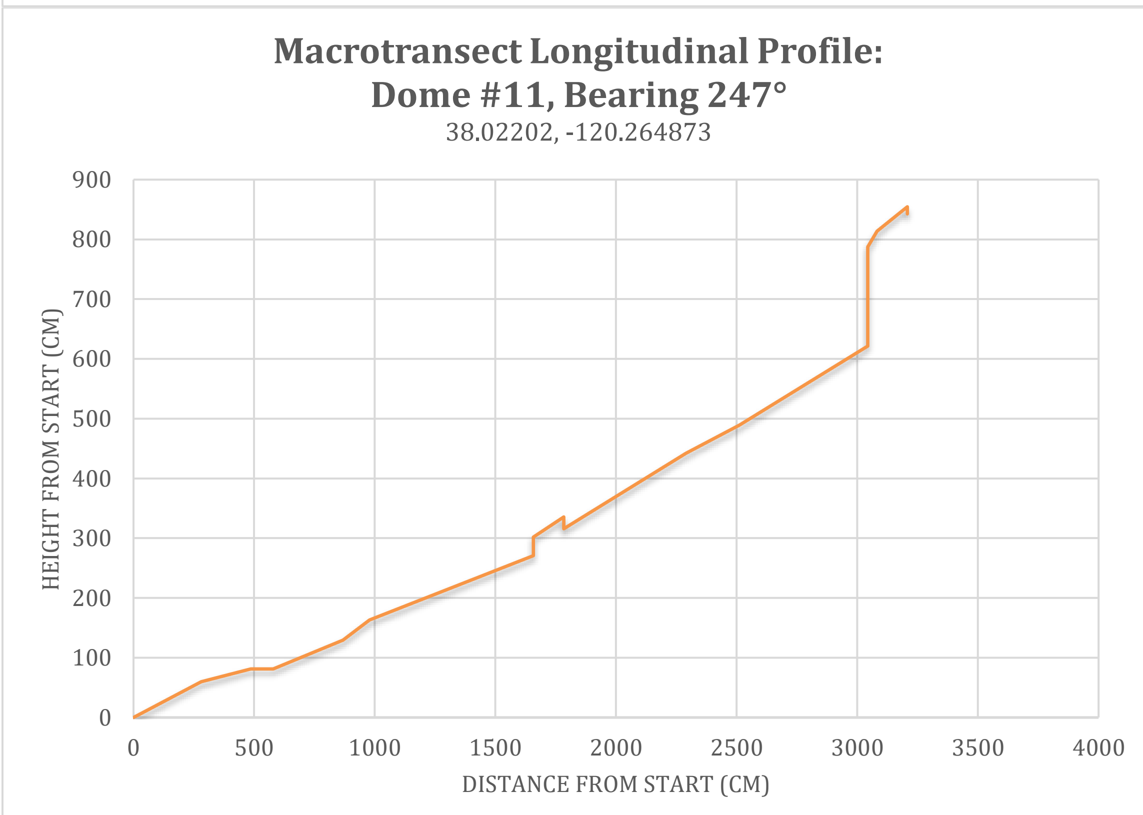
Macrotransect Longitudinal Profile:
Dome #11, Bearing 247°
38.02202, -120.264873
HEIGHT FROM START (CM)
900
800
700
600
500
400
300
200
100
0
0 500 1000 1500 2000 2500 3000 3500 4000
DISTANCE FROM START (CM)

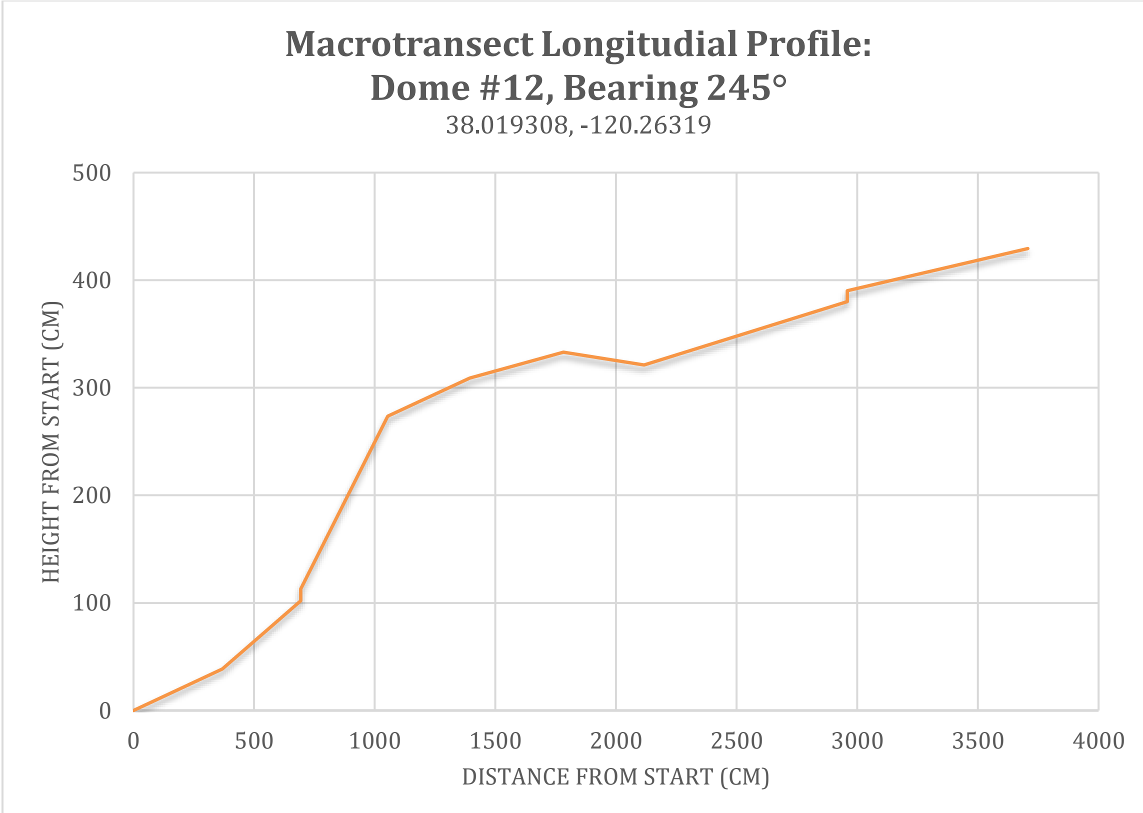
Macrotransect Longitudial Profile:
Dome #12, Bearing 245°
38.019308, -120.26319
HEIGHT FROM START (CM)
0
100
200
300
400
500
DISTANCE FROM START (CM)
0
500
1000
1500
2000
2500
3000
3500
4000

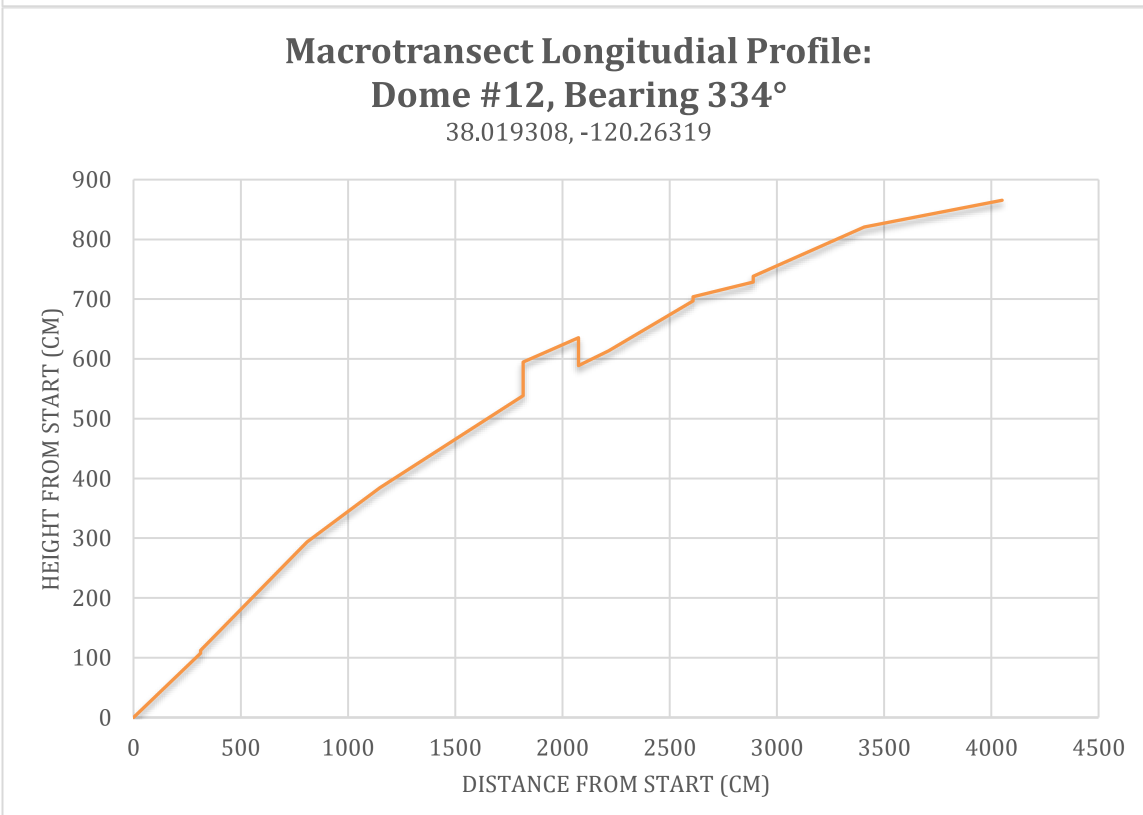
Macrotransect Longitudial Profile:
Dome #12, Bearing 334°
38.019308, -120.26319
HEIGHT FROM START (CM)
0
100
200
300
400
500
600
700
800
900
DISTANCE FROM START (CM)
0
500
1000
1500
2000
2500
3000
3500
4000
4500

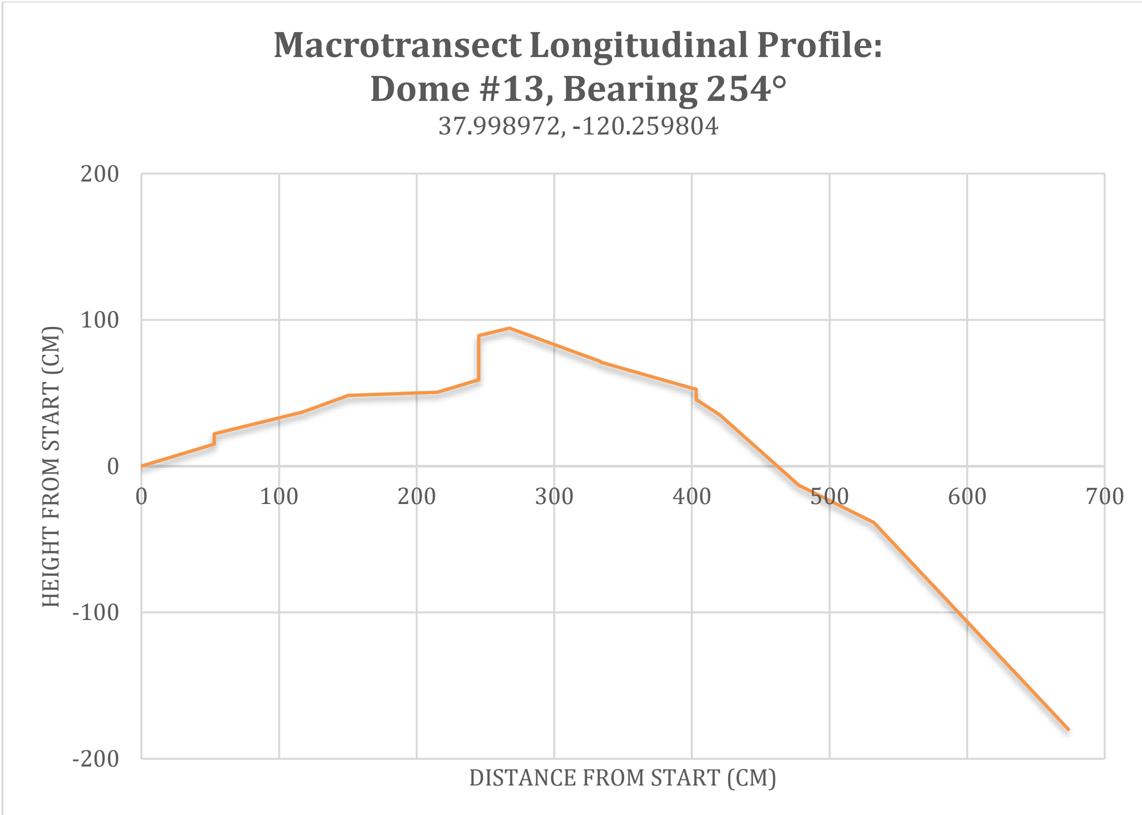
Macrotransect Longitudinal Profile:
Dome #13, Bearing 254°
37.998972, -120.259804
HEIGHT FROM START (CM)
200
100
0
-100
-200
0
100
200
300
400
500
600
700
DISTANCE FROM START (CM)

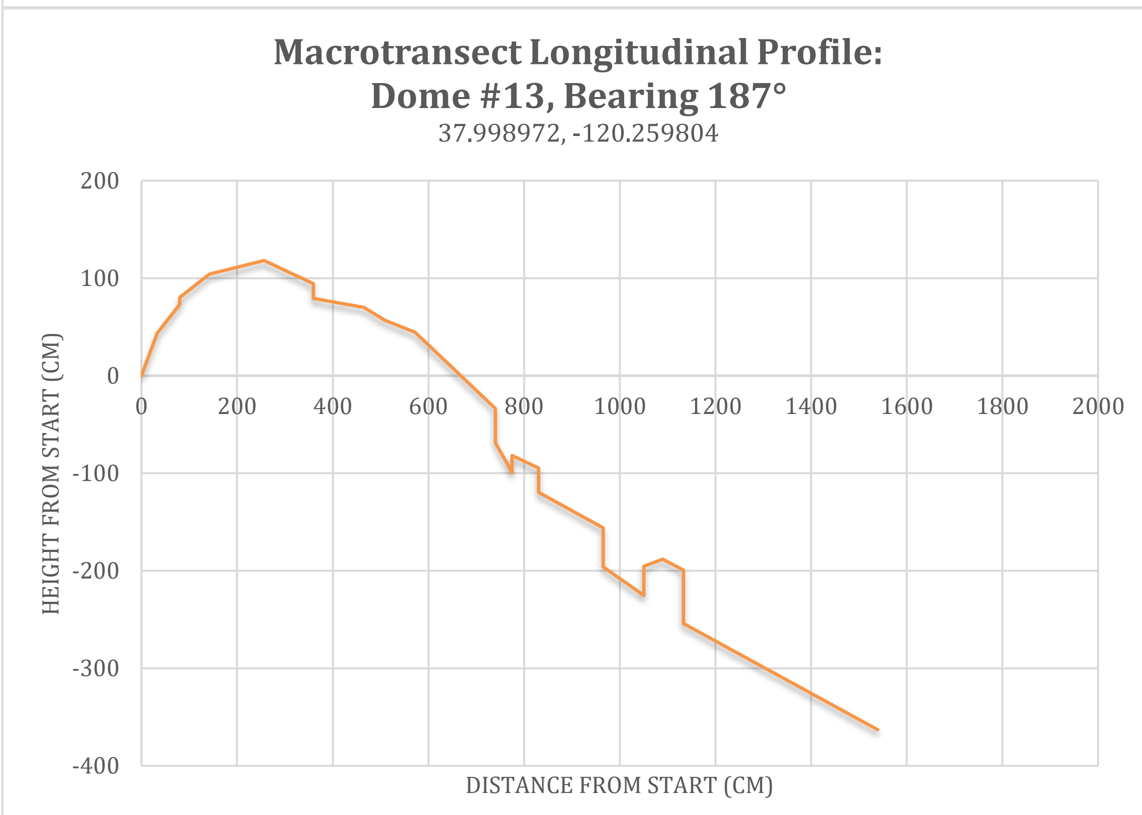
Macrotransect Longitudinal Profile:
Dome #13, Bearing 187°
37.998972, -120.259804
HEIGHT FROM START (CM)
200
100
0
-100
-200
-300
-400
0
200
400
600
800
1000
1200
1400
1600
1800
2000
DISTANCE FROM START (CM)

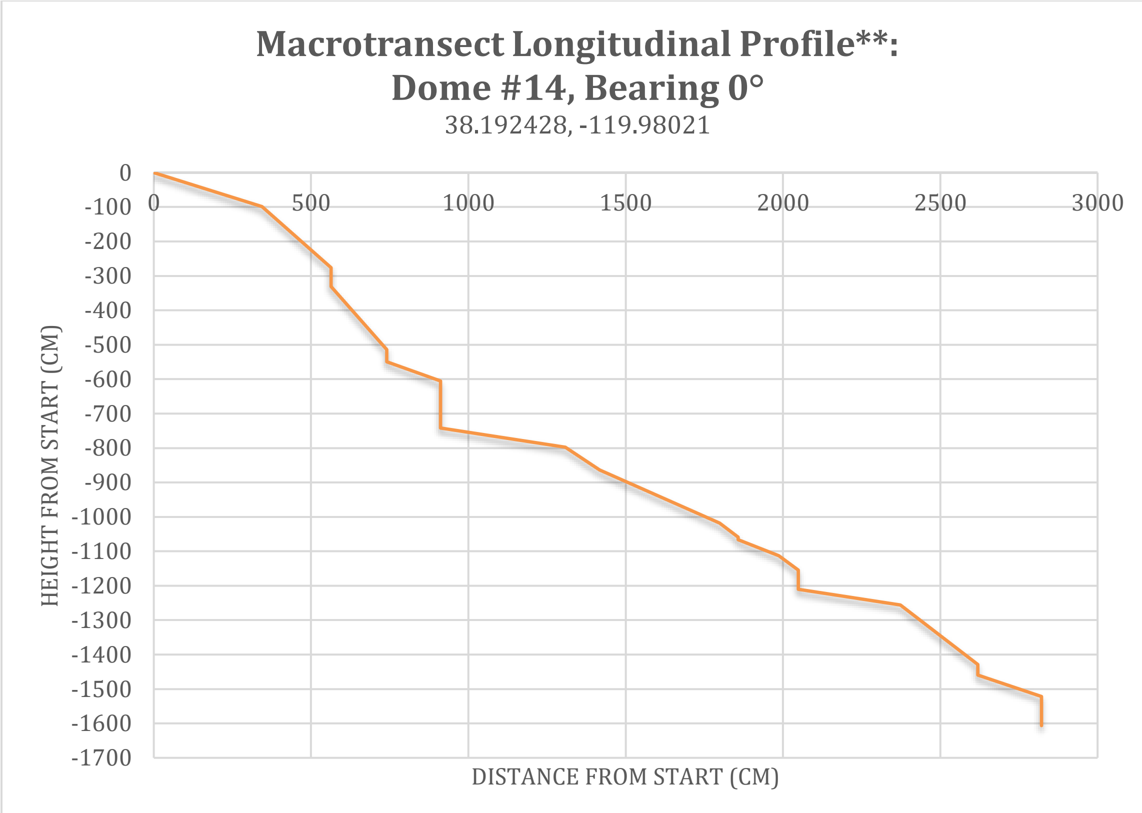

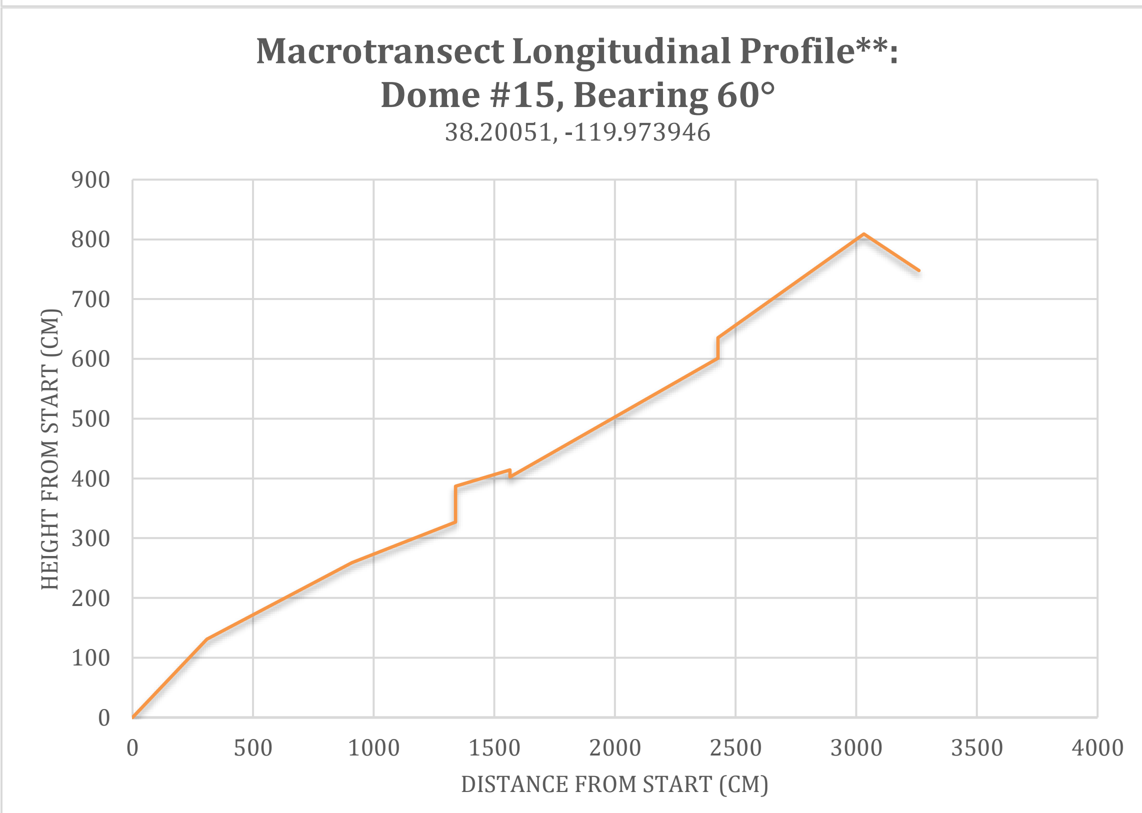

** Only one macrotransect was collected from Domes 14 and 15 due to difficult terrain conditions.

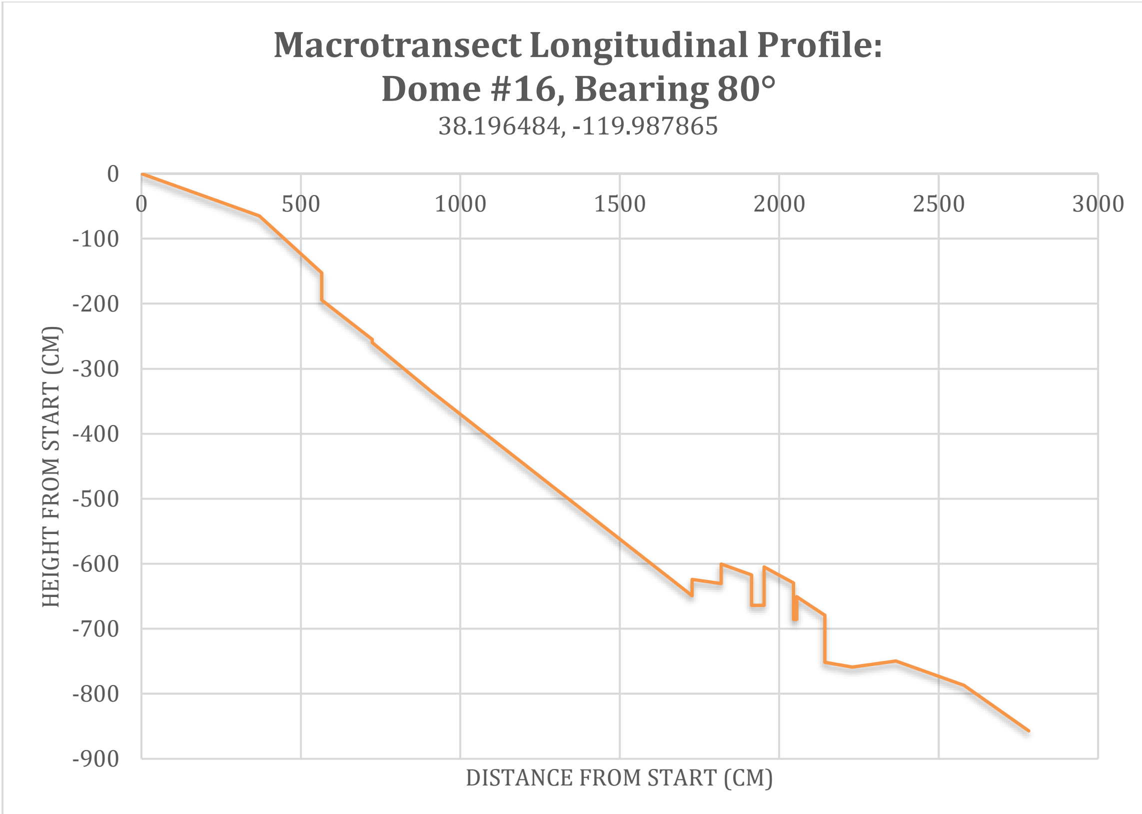
Macrotransect Longitudinal Profile:
Dome #16, Bearing 80°
38.196484, -119.987865
HEIGHT FROM START (CM)
DISTANCE FROM START (CM)
0
-100
-200
-300
-400
-500
-600
-700
-800
-900
0
500
1000
1500
2000
2500
3000

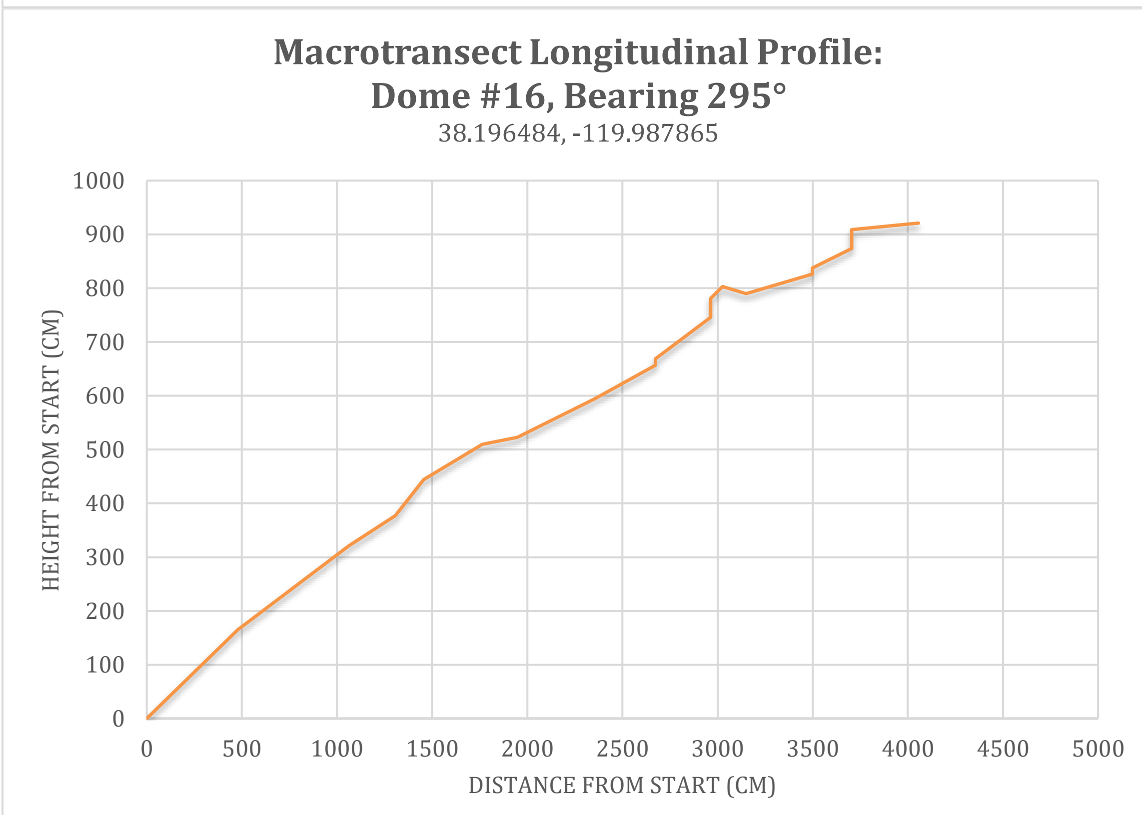
Macrotransect Longitudinal Profile:
Dome #16, Bearing 295°
38.196484, -119.987865
HEIGHT FROM START (CM)
DISTANCE FROM START (CM)
1000
900
800
700
600
500
400
300
200
100
0
0
500
1000
1500
2000
2500
3000
3500
4000
4500
5000

APPENDIX D: SAMPLE MICROTRANSECT DATA SHEET

TRANSECT DATA SHEET FOR LOCATION:

Name(s) Surface Slope GPS Page

Date Surface Orientation Other Notes Photo(s)

Bearing:

ID	Distance (cm)	Crack Parallel to	Crack Length (mm)	Crack Height (mm)	Crack Strike (°)	Crack Dip (°)	Edge Aspect	*Weathering Index*	Cracks <2 cm	GD	Spall	**Microtopography** Strike	Dip
		S F O						0 1 2 3 4 5 6	y n	y n	y n		
		S F O						0 1 2 3 4 5 6	y n	y n	y n		
		S F O						0 1 2 3 4 5 6	y n	y n	y n		
		S F O						0 1 2 3 4 5 6	y n	y n	y n		
		S F O						0 1 2 3 4 5 6	y n	y n	y n		
		S F O						0 1 2 3 4 5 6	y n	y n	y n		
		S F O						0 1 2 3 4 5 6	y n	y n	y n		
		S F O						0 1 2 3 4 5 6	y n	y n	y n		
		S F O						0 1 2 3 4 5 6	y n	y n	y n		
		S F O						0 1 2 3 4 5 6	y n	y n	y n		
		S F O						0 1 2 3 4 5 6	y n	y n	y n		
		S F O						0 1 2 3 4 5 6	y n	y n	y n		
		S F O						0 1 2 3 4 5 6	y n	y n	y n		
		S F O						0 1 2 3 4 5 6	y n	y n	y n		
		S F O						0 1 2 3 4 5 6	y n	y n	y n		
		S F O						0 1 2 3 4 5 6	y n	y n	y n		
		S F O						0 1 2 3 4 5 6	y n	y n	y n		
		S F O						0 1 2 3 4 5 6	y n	y n	y n		
		S F O						0 1 2 3 4 5 6	y n	y n	y n		
		S F O						0 1 2 3 4 5 6	y n	y n	y n		
		S F O						0 1 2 3 4 5 6	y n	y n	y n		
		S F O						0 1 2 3 4 5 6	y n	y n	y n		
		S F O						0 1 2 3 4 5 6	y n	y n	y n		
		S F O						0 1 2 3 4 5 6	y n	y n	y n		
		S F O						0 1 2 3 4 5 6	y n	y n	y n		
		S F O						0 1 2 3 4 5 6	y n	y n	y n		
		S F O						0 1 2 3 4 5 6	y n	y n	y n		
		S F O						0 1 2 3 4 5 6	y n	y n	y n		
		S F O						0 1 2 3 4 5 6	y n	y n	y n		

Cracks <2 cm: Evidence of microcracks <2 cm long.

GD: Evidence of granular disentigration.

Spall: Evidence of spalling.

Crack Strike measured using right hand rule.

Crack Length defined as the length of the long side of the plane defining the crack.

S: Surface, F: Fabric (joints, bedding), O: Other

WEATHERING INDEX:

0: fresh, no signs of oxidation or weatherin

1: fresh with < 50% face oxidized

2: fresh with > 50% face oxidized

3: sharp and fully oxidized

4: rounded corner & fully oxidized

5: rounded no corner, sealed

6:

APPENDIX E: STATISTICAL TABLES

Section E-1: Slab thickness statistics

Table E - 1: **Single factor ANOVA results for thickness of Slabs 2, 3, and 4.**

SUMMARY

Groups	*Count*	*Sum*	*Average*	*Variance*
Slab 2	17	765.5	45.02941	2021.077
Slab 3	65	2317.1	35.64769	1368.773
Slab 4	52	1795.8	34.53462	1156.196

ANOVA

Source of Variation	*SS*	*df*	*MS*	*F*	*P-value*	*F crit*
Between Groups	1483.66	2	741.83	0.543193	0.58219332	3.065296
Within Groups	178904.7	131	1365.685			
Total	180388.4	133				

Table E - 2: **Slab 2 and Slab 3 thickness comparative Student's t-test results.**

t-Test: Two-Sample Assuming Equal Variances

	Slab 2	*Slab 3*
Mean	45.029	35.647
Variance	2021.077	1368.773
Observations	17	65
Pooled Variance	1499.233	
Hypothesized Mean Difference	0	
df	80	
t Stat	0.8894	
P(T<=t) one-tail	0.1882	
t Critical one-tail	1.6641	
P(T<=t) two-tail	0.3764	
t Critical two-tail	1.9900	

t-Test: Two-Sample Assuming Unequal Variances

	Slab 2	*Slab 3*
Mean	45.029	35.647
Variance	2021.07	1368.77
Observations	17	65
Hypothesized Mean Difference	0	
df	22	
t Stat	0.7930	
P(T<=t) one-tail	0.2181	
t Critical one-tail	1.7171	
P(T<=t) two-tail	0.4362	
t Critical two-tail	2.0738	

Table E - 3: **Slab 2 and Slab 4 thickness comparative Student's t-test results.**

t-Test: Two-Sample Assuming Equal Variances

	Slab 2	*Slab 4*
Mean	45.029	34.534
Variance	2021.07	1156.19
Observations	17	52
Pooled Variance	1362.73	
Hypothesized Mean Difference	0	
df	67	
t Stat	1.01758	
P(T<=t) one-tail	0.1562	
t Critical one-tail	1.6679	
P(T<=t) two-tail	0.3125	
t Critical two-tail	1.9960	

t-Test: Two-Sample Assuming Unequal Variances

	Slab 2	*Slab 4*
Mean	45.029	34.534
Variance	2021.07	1156.19
Observations	17	52
Hypothesized Mean Difference	0	
df	22	
t Stat	0.8834	
P(T<=t) one-tail	0.1932	
t Critical one-tail	1.7171	
P(T<=t) two-tail	0.3865	
t Critical two-tail	2.0738	

Table E - 4: **Slab 3 and Slab 4 thickness comparative Student's t-test results.**

t-Test: Two-Sample Assuming Equal Variances

	Slab 3	*Slab 4*
Mean	35.647	34.534
Variance	1368.77	1156.19
Observations	65	52
Pooled Variance	1274.5	
Hypothesized Mean Difference	0	
df	115	
t Stat	0.1675	
P(T<=t) one-tail	0.4336	
t Critical one-tail	1.6582	
P(T<=t) two-tail	0.8672	
t Critical two-tail	1.9808	

t-Test: Two-Sample Assuming Unequal Variances

	Slab 3	*Slab 4*
Mean	35.64769	34.534
Variance	1368.77	1156.19
Observations	65	52
Hypothesized Mean Difference	0	
df	113	
t Stat	0.1691	
P(T<=t) one-tail	0.4329	
t Critical one-tail	1.6584	
P(T<=t) two-tail	0.8659	
t Critical two-tail	1.9811	

Section E-2: Schmidt hammer statistics

Table E - 5: **Single factor ANOVA results for Slabs 1 - 4 Schmidt hammer R-values**

SUMMARY

Groups	*Count*	*Sum*	*Average*	*Variance*
Slab 1	298	14790	49.63087	116.9407
Slab 2	1707	58041	34.00176	117.5973
Slab 3	1906	53423	28.02886	113.1829
Slab 4	1594	30555	19.16876	55.57791

ANOVA

Source of Variation	*SS*	*df*	*MS*	*F*	*P-value*	*F crit*
Between Groups	323945.6	3	107981.9	1101.032	0	2.606523
Within Groups	539501.4	5501	98.07333			
Total	863447	5504				

Table E - 6: **Slab 1 & Slab 2 Student's t-test results for Schmidt hammer R-values.**

t-Test: Two-Sample Assuming Equal Variances

	Slab 1	*Slab 2*
Mean	49.63	34.00
Variance	116.94	117.59
Observations	298	1707
Pooled Variance	117.4999	
Hypothesized Mean Difference	0	
df	2003	
t Stat	22.9658	
P(T<=t) one-tail	4.2E-104	
t Critical one-tail	1.645615	
P(T<=t) two-tail	8.4E-104	
t Critical two-tail	1.9611	

t-Test: Two-Sample Assuming Unequal Variances

	Slab 1	*Slab 2*
Mean	49.63	34.00
Variance	116.94	117.59
Observations	298	1707
Hypothesized Mean Difference	0	
df	408	
t Stat	23.0111	
P(T<=t) one-tail	5.13E-76	
t Critical one-tail	1.648597	
P(T<=t) two-tail	1.03E-75	
t Critical two-tail	1.9657	

Table E - 7: **Slab 1 & Slab 3 Student's t-test results for Schmidt hammer R-values.**

t-Test: Two-Sample Assuming Equal Variances

	Slab 1	*Slab 3*
Mean	49.63	28.028
Variance	116.94	113.18
Observations	298	1906
Pooled Variance	113.68	
Hypothesized Mean Difference	0	
df	2202	
t Stat	32.5235	
P(T<=t) one-tail	3.9E-190	
t Critical one-tail	1.645546	
P(T<=t) two-tail	7.9E-190	
t Critical two-tail	1.9610	

t-Test: Two-Sample Assuming Unequal Variances

	Slab 1	*Slab 3*
Mean	49.63	28.02
Variance	116.94	113.18
Observations	298	1906
Hypothesized Mean Difference	0	
df	392	
t Stat	32.13814	
P(T<=t) one-tail	3.3E-112	
t Critical one-tail	1.64875	
P(T<=t) two-tail	6.6E-112	
t Critical two-tail	1.966034	

Table E - 8: **Slab 1 & Slab 4 Student's t-test results for Schmidt hammer R-values.**

t-Test: Two-Sample Assuming Equal Variances

	Slab 1	*Slab 4*
Mean	49.63	19.16
Variance	116.94	55.57
Observations	298	1594
Pooled Variance	65.22063	
Hypothesized Mean Difference	0	
df	1890	
t Stat	59.7667	
P(T<=t) one-tail	0	
t Critical one-tail	1.64566	
P(T<=t) two-tail	0	
t Critical two-tail	1.96122	

t-Test: Two-Sample Assuming Unequal Variances

	Slab 1	*Slab 4*
Mean	49.63087	19.16876
Variance	116.9407	55.57791
Observations	298	1594
Hypothesized Mean Difference	0	
df	352	
t Stat	46.60162	
P(T<=t) one-tail	6.2E-153	
t Critical one-tail	1.649194	
P(T<=t) two-tail	1.2E-152	
t Critical two-tail	1.966726	

Table E - 9: **Slab 2 & Slab 3 Student's t-test results for Schmidt hammer R-values.**

t-Test: Two-Sample Assuming Equal Variances

	Slab 2	*Slab 3*
Mean	34.00	28.02
Variance	117.59	113.18
Observations	1707	1906
Pooled Variance	115.2685	
Hypothesized Mean Difference	0	
df	3611	
t Stat	16.69453	
P(T<=t) one-tail	1.24E-60	
t Critical one-tail	1.645276	
P(T<=t) two-tail	2.49E-60	
t Critical two-tail	1.960621	

t-Test: Two-Sample Assuming Unequal Variances

	Slab 2	*Slab 3*
Mean	34.00176	28.02886
Variance	117.5973	113.1829
Observations	1707	1906
Hypothesized Mean Difference	0	
df	3552	
t Stat	16.67695	
P(T<=t) one-tail	1.77E-60	
t Critical one-tail	1.645283	
P(T<=t) two-tail	3.54E-60	
t Critical two-tail	1.960632	

Table E - 10: **Slab 2 & Slab 4 Student's t-test results for Schmidt hammer R-values.**

t-Test: Two-Sample Assuming Equal Variances

	Slab 2	*Slab 4*
Mean	34.00	19.16
Variance	117.59	55.57
Observations	1707	1594
Pooled Variance	87.64977	
Hypothesized Mean Difference	0	
df	3299	
t Stat	45.48747	
P(T<=t) one-tail	0	
t Critical one-tail	1.645316	
P(T<=t) two-tail	0	
t Critical two-tail	1.960683	

t-Test: Two-Sample Assuming Unequal Variances

	Slab 2	*Slab 4*
Mean	34.00176	19.16876
Variance	117.5973	55.57791
Observations	1707	1594
Hypothesized Mean Difference	0	
df	3037	
t Stat	46.04875	
P(T<=t) one-tail	0	
t Critical one-tail	1.645356	
P(T<=t) two-tail	0	
t Critical two-tail	1.960745	

Table E - 11: **Slab 3 & Slab 4 Student's t-test results for Schmidt hammer R-values.**

t-Test: Two-Sample Assuming Equal Variances

	Slab 3	*Slab 4*
Mean	28.02	19.16
Variance	113.18	55.57
Observations	1906	1594
Pooled Variance	86.9494	
Hypothesized Mean Difference	0	
df	3498	
t Stat	27.99476	
P(T<=t) one-tail	4.4E-156	
t Critical one-tail	1.645289	
P(T<=t) two-tail	8.7E-156	
t Critical two-tail	1.960642	

t-Test: Two-Sample Assuming Unequal Variances

	Slab 3	*Slab 4*
Mean	28.02886	19.16876
Variance	113.1829	55.57791
Observations	1906	1594
Hypothesized Mean Difference	0	
df	3398	
t Stat	28.8602	
P(T<=t) one-tail	2.7E-164	
t Critical one-tail	1.645302	
P(T<=t) two-tail	5.3E-164	
t Critical two-tail	1.960662	

Section E-3: Crack length statistics

Table E - 12: **Single factor ANOVA results for crack length (millimeters) of Slabs 1 – 4.**

SUMMARY

Groups	*Count*	*Sum*	*Average*	*Variance*
Slab 1	67	13412.1	200.1806	291450.8
Slab 2	522	136173.3	260.8684	478898.4
Slab 3	291	78532.4	269.8708	820251.9
Slab 4	169	38223.6	226.1751	348831.6

ANOVA

Source of Variation	*SS*	*df*	*MS*	*F*	*P-value*	*F crit*
Between Groups	422823.4	3	140941.1	0.260578	0.853811	2.61342
Within Groups	5.65E+08	1045	540879			
Total	5.66E+08	1048				

Table E - 13: **Slab 1 & Slab 2 Student's t-test results for crack length (millimeters).**

t-Test: Two-Sample Assuming Equal Variances

	Slab 1	*Slab 2*
Mean	200.18	260.86
Variance	291450.8	478898.4
Observations	67	522
Pooled Variance	457822.5	
Hypothesized Mean Difference	0	
df	587	
t Stat	-0.691	
P(T<=t) one-tail	0.2448	
t Critical one-tail	1.6474	
P(T<=t) two-tail	0.4897	
t Critical two-tail	1.9640	

t-Test: Two-Sample Assuming Unequal Variances

	Slab 1	*Slab 2*
Mean	200.18	260.86
Variance	291450.8	478898.4
Observations	67	522
Hypothesized Mean Difference	0	
df	96	
t Stat	-0.836	
P(T<=t) one-tail	0.2025	
t Critical one-tail	1.6608	
P(T<=t) two-tail	0.4051	
t Critical two-tail	1.9849	

Table E - 14: **Slab 1 & Slab 3 Student's t-test results for crack length (millimeters)**.

t-Test: Two-Sample Assuming Equal Variances

	Slab 1	*Slab 3*
Mean	200.18	269.87
Variance	291450	820252
Observations	67	291
Pooled Variance	722215.7	
Hypothesized Mean Difference	0	
df	356	
t Stat	-0.60517	
P(T<=t) one-tail	0.272724	
t Critical one-tail	1.649145	
P(T<=t) two-tail	0.545449	
t Critical two-tail	1.96665	

t-Test: Two-Sample Assuming Unequal Variances

	Slab 1	*Slab 3*
Mean	200.18	269.87
Variance	291450	820252
Observations	67	291
Hypothesized Mean Difference	0	
df	164	
t Stat	-0.8231	
P(T<=t) one-tail	0.20582	
t Critical one-tail	1.65419	
P(T<=t) two-tail	0.41164	
t Critical two-tail	1.97453	

Table E - 15: **Slab 1 & Slab 4 Student's t-test results for crack lengths (millimeters).**

t-Test: Two-Sample Assuming Equal Variances

	Slab 1	*Slab 4*
Mean	200.18	226.17
Variance	291450	348831
Observations	67	169
Pooled Variance	332647.3	
Hypothesized Mean Difference	0	
df	234	
t Stat	-0.3121	
P(T<=t) one-tail	0.37758	
t Critical one-tail	1.65139	
P(T<=t) two-tail	0.75517	
t Critical two-tail	1.97015	

t-Test: Two-Sample Assuming Unequal Variances

	Slab 1	*Slab 4*
Mean	200.18	226.17
Variance	291450	348831
Observations	67	169
Hypothesized Mean Difference	0	
df	132	
t Stat	-0.324	
P(T<=t) one-tail	0.3730	
t Critical one-tail	1.6564	
P(T<=t) two-tail	0.7460	
t Critical two-tail	1.9780	

Table E - 16: **Slab 2 & Slab 3 Student's t-test results for crack lengths (millimeters).**

t-Test: Two-Sample Assuming Equal Variances

	Slab 2	*Slab 3*
Mean	260.868	269.870
Variance	478898	820252
Observations	522	291
Pooled Variance	600960.7	
Hypothesized Mean Difference	0	
df	811	
t Stat	-0.15873	
P(T<=t) one-tail	0.436959	
t Critical one-tail	1.646735	
P(T<=t) two-tail	0.873917	
t Critical two-tail	1.962893	

t-Test: Two-Sample Assuming Unequal Variances

	Slab 2	*Slab 3*
Mean	260.86	269.87
Variance	478898.4	820251.9
Observations	522	291
Hypothesized Mean Difference	0	
df	481	
t Stat	-0.14728	
P(T<=t) one-tail	0.441486	
t Critical one-tail	1.648028	
P(T<=t) two-tail	0.882972	
t Critical two-tail	1.964908	

Table E - 17: **Slab 2 & Slab 4 Student's t-test results for crack lengths (millimeters).**

t-Test: Two-Sample Assuming Equal Variances

	Slab 2	*Slab 4*
Mean	260.86	226.17
Variance	478898	348831
Observations	522	169
Pooled Variance	447184	
Hypothesized Mean Difference	0	
df	689	
t Stat	0.586194	
P(T<=t) one-tail	0.278969	
t Critical one-tail	1.647068	
P(T<=t) two-tail	0.557937	
t Critical two-tail	1.963413	

t-Test: Two-Sample Assuming Unequal Variances

	Slab 2	*Slab 4*
Mean	260.86	226.17
Variance	478898	348831
Observations	522	169
Hypothesized Mean Difference	0	
df	330	
t Stat	0.635369	
P(T<=t) one-tail	0.262814	
t Critical one-tail	1.649484	
P(T<=t) two-tail	0.525628	
t Critical two-tail	1.967179	

Table E - 18: **Slab 3 & Slab 4 Student's t-test results for crack lengths (millimeters).**

t-Test: Two-Sample Assuming Equal Variances

	Slab 3	*Slab 4*
Mean	269.870	226.175
Variance	820252	348831
Observations	291	169
Pooled Variance	647329.2	
Hypothesized Mean Difference	0	
df	458	
t Stat	0.561547	
P(T<=t) one-tail	0.28735	
t Critical one-tail	1.648187	
P(T<=t) two-tail	0.574699	
t Critical two-tail	1.965157	

t-Test: Two-Sample Assuming Unequal Variances

	Slab 3	*Slab 4*
Mean	269.870	226.175
Variance	820252	348831
Observations	291	169
Hypothesized Mean Difference	0	
df	452	
t Stat	0.62532	
P(T<=t) one-tail	0.266038	
t Critical one-tail	1.648232	
P(T<=t) two-tail	0.532077	
t Critical two-tail	1.965226	

Section E-4: Crack height / Spall thickness statistics

Table E - 19: **Single factor ANOVA results for crack height (millimeters).**

SUMMARY

Groups	*Count*	*Sum*	*Average*	*Variance*
Slab 1	67	367	5.477612	38.3751
Slab 2	522	4595.9	8.804406	175.1656
Slab 3	291	2333.5	8.0189	338.7248
Slab 4	169	4294.6	25.41183	6210.967

ANOVA

Source of Variation	*SS*	*df*	*MS*	*F*	*P-value*	*F crit*
Between Groups	42244.64	3	14081.55	11.91065	1.13E-07	2.613419814
Within Groups	1235467	1045	1182.265			
Total	1277711	1048				

Table E - 20: **Slab 1 & Slab 2 Student's t-test results for crack height (millimeters).**

t-Test: Two-Sample Assuming Equal Variances

	Slab 1	*Slab 2*
Mean	5.47761	8.80440
Variance	38.3751	175.165
Observations	67	522
Pooled Variance	159.7854	
Hypothesized Mean Difference	0	
df	587	
t Stat	-2.0280	
P(T<=t) one-tail	0.02150	
t Critical one-tail	1.64745	
P(T<=t) two-tail	0.04300	
t Critical two-tail	1.96401	

t-Test: Two-Sample Assuming Unequal Variances

	Slab 1	*Slab 2*
Mean	5.47761	8.80440
Variance	38.3751	175.165
Observations	67	522
Hypothesized Mean Difference	0	
df	159	
t Stat	-3.49063	
P(T<=t) one-tail	0.000312	
t Critical one-tail	1.654494	
P(T<=t) two-tail	0.000624	
t Critical two-tail	1.974996	

Table E - 21: **Slab 1 & Slab 3 Student's t-test results for crack height (millimeters).**

t-Test: Two-Sample Assuming Equal Variances

	Slab 1	*Slab 3*
Mean	5.47761	8.0189
Variance	38.3751	338.724
Observations	67	291
Pooled Variance	283.042	
Hypothesized Mean Difference	0	
Df	356	
t Stat	-1.11473	
P(T<=t) one-tail	0.132858	
t Critical one-tail	1.649145	
P(T<=t) two-tail	0.265717	
t Critical two-tail	1.96665	

t-Test: Two-Sample Assuming Unequal Variances

	Slab 1	*Slab 3*
Mean	5.47761	8.0189
Variance	38.3751	338.724
Observations	67	291
Hypothesized Mean Difference	0	
df	313	
t Stat	-1.92834	
P(T<=t) one-tail	0.027359	
t Critical one-tail	1.649736	
P(T<=t) two-tail	0.054717	
t Critical two-tail	1.967572	

Table E - 22: **Slab 1 & Slab 4 Student's t-test results for crack height (millimeters).**

t-Test: Two-Sample Assuming Equal Variances

	Slab 1	*Slab 4*
Mean	5.47761	25.4118
Variance	38.3751	6210.96
Observations	67	169
Pooled Variance	4469.98	
Hypothesized Mean Difference	0	
df	234	
t Stat	-2.0652	
P(T<=t) one-tail	0.02000	
t Critical one-tail	1.65139	
P(T<=t) two-tail	0.04000	
t Critical two-tail	1.97015	

t-Test: Two-Sample Assuming Unequal Variances

	Slab 1	*Slab 4*
Mean	5.47761	25.4118
Variance	38.3751	6210.96
Observations	67	169
Hypothesized Mean Difference	0	
df	173	
t Stat	-3.26291	
P(T<=t) one-tail	0.000664	
t Critical one-tail	1.653709	
P(T<=t) two-tail	0.001329	
t Critical two-tail	1.973771	

Table E - 23: **Slab 2 & Slab 3 Student's t-test results for crack height (millimeters).**

t-Test: Two-Sample Assuming Equal Variances

	Slab 2	*Slab 3*
Mean	8.80440	8.0189
Variance	175.165	338.724
Observations	522	291
Pooled Variance	233.6516	
Hypothesized Mean Difference	0	
df	811	
t Stat	0.702427	
P(T<=t) one-tail	0.241307	
t Critical one-tail	1.646735	
P(T<=t) two-tail	0.482614	
t Critical two-tail	1.962893	

t-Test: Two-Sample Assuming Unequal Variances

	Slab 2	*Slab 3*
Mean	8.80440	8.0189
Variance	175.165	338.724
Observations	522	291
Hypothesized Mean Difference	0	
df	460	
t Stat	0.641455	
P(T<=t) one-tail	0.260773	
t Critical one-tail	1.648173	
P(T<=t) two-tail	0.521547	
t Critical two-tail	1.965134	

Table E - 24: **Slab 2 & Slab 4 Student's t-test results for crack height (millimeters).**

t-Test: Two-Sample Assuming Equal Variances

	Slab 2	*Slab 4*
Mean	8.80440	25.4118
Variance	175.165	6210.96
Observations	522	169
Pooled Variance	1646.885	
Hypothesized Mean Difference	0	
df	689	
t Stat	-4.62392	
P(T<=t) one-tail	2.25E-06	
t Critical one-tail	1.647068	
P(T<=t) two-tail	4.5E-06	
t Critical two-tail	1.963413	

t-Test: Two-Sample Assuming Unequal Variances

	Slab 2	*Slab 4*
Mean	8.80440	25.4118
Variance	175.165	6210.96
Observations	522	169
Hypothesized Mean Difference	0	
df	171	
t Stat	-2.72705	
P(T<=t) one-tail	0.003528	
t Critical one-tail	1.653813	
P(T<=t) two-tail	0.007057	
t Critical two-tail	1.973934	

Table E - 25: **Slab 3 & Slab 4 Student's t-test results for crack height (millimeters).**

t-Test: Two-Sample Assuming Equal Variances

	Slab 3	*Slab 4*
Mean	8.0189	25.411
Variance	338.724	6210.9
Observations	291	169
Pooled Variance	2492.735	
Hypothesized Mean Difference	0	
df	458	
t Stat	-3.60202	
P(T<=t) one-tail	0.000175	
t Critical one-tail	1.648187	
P(T<=t) two-tail	0.00035	
t Critical two-tail	1.965157	

t-Test: Two-Sample Assuming Unequal Variances

	Slab 3	*Slab 4*
Mean	8.0189	25.4118
Variance	338.724	6210.96
Observations	291	169
Hypothesized Mean Difference	0	
df	179	
t Stat	-2.82466	
P(T<=t) one-tail	0.002635	
t Critical one-tail	1.653411	
P(T<=t) two-tail	0.00527	
t Critical two-tail	1.973305	

Section E-5: Weathering index statistics

Table E - 26: **Single factor ANOVA for weathering index averages.**

SUMMARY

Groups	*Count*	*Sum*	*Average*	*Variance*
Slab 1	66	281.5	4.265152	0.855536
Slab 2	522	2458.5	4.70977	0.948714
Slab 3	290	1331.5	4.591379	0.707019
Slab 4	170	772	4.541176	0.758649

ANOVA

Source of Variation	*SS*	*df*	*MS*	*F*	*P-value*	*F crit*
Between Groups	13.80808	3	4.602692	5.445429	0.001023	2.613428
Within Groups	882.4302	1044	0.84524			
Total	896.2383	1047				

Table E - 27: **Slab 1 & Slab 2 Student's t-test results for weathering index averages.**

t-Test: Two-Sample Assuming Equal Variances

	Slab 1	*Slab 2*
Mean	4.26515	4.70977
Variance	0.85553	0.94871
Observations	66	522
Pooled Variance	0.938379	
Hypothesized Mean Difference	0	
df	586	
t Stat	-3.51331	
P(T<=t) one-tail	0.000238	
t Critical one-tail	1.647458	
P(T<=t) two-tail	0.000477	
t Critical two-tail	1.96402	

t-Test: Two-Sample Assuming Unequal Variances

	Slab 1	*Slab 2*
Mean	4.26515	4.70977
Variance	0.85553	0.94871
Observations	66	522
Hypothesized Mean Difference	0	
df	84	
t Stat	-3.6572	
P(T<=t) one-tail	0.000222	
t Critical one-tail	1.663197	
P(T<=t) two-tail	0.000444	
t Critical two-tail	1.98861	

Table E - 28: **Slab 1 & Slab 3 Student's t-test results for weathering index average.**

t-Test: Two-Sample Assuming Equal Variances

	Slab 1	*Slab 3*
Mean	4.26515	4.59137
Variance	0.85553	0.70701
Observations	66	290
Pooled Variance	0.734289	
Hypothesized Mean Difference	0	
df	354	
t Stat	-2.79147	
P(T<=t) one-tail	0.002766	
t Critical one-tail	1.649169	
P(T<=t) two-tail	0.005531	
t Critical two-tail	1.966688	

t-Test: Two-Sample Assuming Unequal Variances

	Slab 1	*Slab 3*
Mean	4.26515	4.59137
Variance	0.85553	0.70701
Observations	66	290
Hypothesized Mean Difference	0	
df	91	
t Stat	-2.62876	
P(T<=t) one-tail	0.00503	
t Critical one-tail	1.661771	
P(T<=t) two-tail	0.01006	
t Critical two-tail	1.986377	

Table E - 29: **Slab 1 & Slab 4 Student's t-test results for weathering index averages.**

t-Test: Two-Sample Assuming Equal Variances

	Slab 1	*Slab 4*
Mean	4.26515	4.54117
Variance	0.85553	0.75864
Observations	66	170
Pooled Variance	0.785562	
Hypothesized Mean Difference	0	
df	234	
t Stat	-2.14733	
P(T<=t) one-tail	0.016398	
t Critical one-tail	1.651391	
P(T<=t) two-tail	0.032795	
t Critical two-tail	1.970154	

t-Test: Two-Sample Assuming Unequal Variances

	Slab 1	*Slab 4*
Mean	4.26515	4.54117
Variance	0.85553	0.75864
Observations	66	170
Hypothesized Mean Difference	0	
df	112	
t Stat	-2.09102	
P(T<=t) one-tail	0.019394	
t Critical one-tail	1.658573	
P(T<=t) two-tail	0.038788	
t Critical two-tail	1.981372	

Table E - 30: **Slab 2 & Slab 3 Student's t-test results for weathering index averages.**

t-Test: Two-Sample Assuming Equal Variances

	Slab 2	*Slab 3*
Mean	4.70977	4.59137
Variance	0.94871	0.70701
Observations	522	290
Pooled Variance	0.86248	
Hypothesized Mean Difference	0	
df	810	
t Stat	1.740603	
P(T<=t) one-tail	0.041066	
t Critical one-tail	1.646737	
P(T<=t) two-tail	0.082133	
t Critical two-tail	1.962897	

t-Test: Two-Sample Assuming Unequal Variances

	Slab 2	*Slab 3*
Mean	4.70977	4.59137
Variance	0.94871	0.70701
Observations	522	290
Hypothesized Mean Difference	0	
df	673	
t Stat	1.814867	
P(T<=t) one-tail	0.034995	
t Critical one-tail	1.647121	
P(T<=t) two-tail	0.069989	
t Critical two-tail	1.963495	

Table E - 31: **Slab 2 & Slab 4 Student's t-test results for weathering index averages.**

t-Test: Two-Sample Assuming Equal Variances

	Slab 2	*Slab 4*
Mean	4.70977	4.54117
Variance	0.94871	0.75864
Observations	522	170
Pooled Variance	0.902162	
Hypothesized Mean Difference	0	
df	690	
t Stat	2.010044	
P(T<=t) one-tail	0.022408	
t Critical one-tail	1.647065	
P(T<=t) two-tail	0.044815	
t Critical two-tail	1.963408	

t-Test: Two-Sample Assuming Unequal Variances

	Slab 2	*Slab 4*
Mean	4.70977	4.54117
Variance	0.94871	0.75864
Observations	522	170
Hypothesized Mean Difference	0	
df	318	
t Stat	2.127442	
P(T<=t) one-tail	0.017076	
t Critical one-tail	1.649659	
P(T<=t) two-tail	0.034153	
t Critical two-tail	1.967452	

Table E - 32: **Slab 3 & Slab 4 Student's t-test results for weathering index averages.**

t-Test: Two-Sample Assuming Equal Variances

	Slab 3	*Slab 4*
Mean	4.59137	4.54117
Variance	0.70701	0.75864
Observations	290	170
Pooled Variance	0.72607	
Hypothesized Mean Difference	0	
df	458	
t Stat	0.609935	
P(T<=t) one-tail	0.271104	
t Critical one-tail	1.648187	
P(T<=t) two-tail	0.542207	
t Critical two-tail	1.965157	

t-Test: Two-Sample Assuming Unequal Variances

	Slab 3	*Slab 4*
Mean	4.59137	4.54117
Variance	0.70701	0.75864
Observations	290	170
Hypothesized Mean Difference	0	
df	344	
t Stat	0.604343	
P(T<=t) one-tail	0.273007	
t Critical one-tail	1.649295	
P(T<=t) two-tail	0.546014	
t Critical two-tail	1.966884	

APPENDIX F: ROSE DIAGRAMS PER SITE

Section F-1: Site 0 "Twain Harte Rock"

Uniaxial

Slab 1

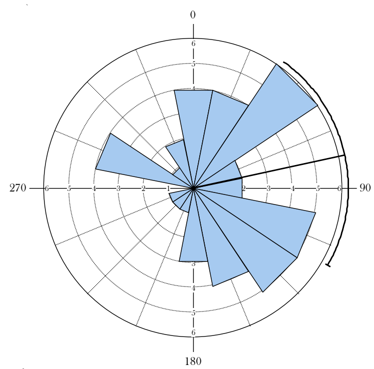

Slab 2

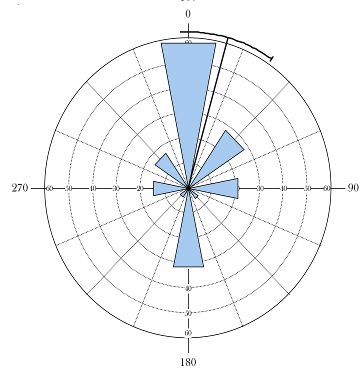

Slab 3

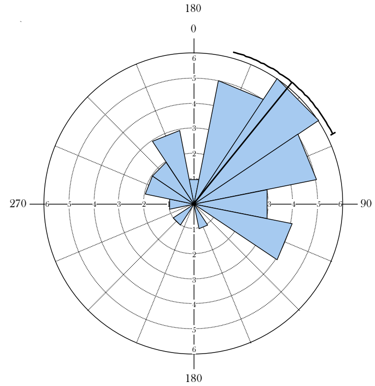

Slab 4

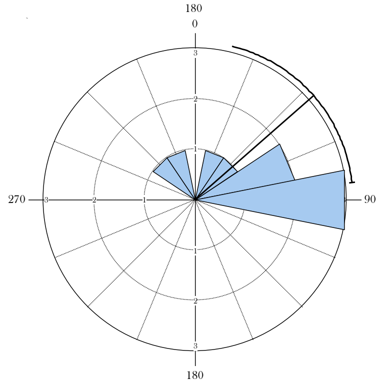

Uniaxial

All Slabs

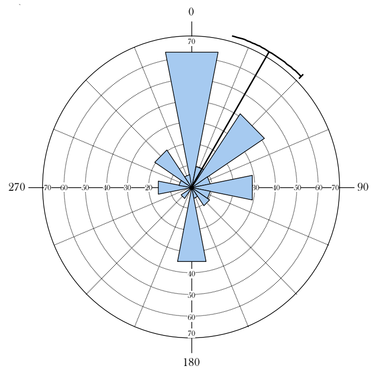

Section F-2: Site 2

Slab 1

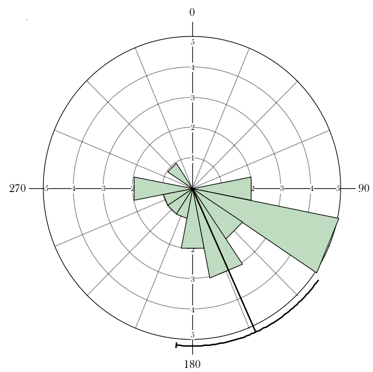

Slab 2

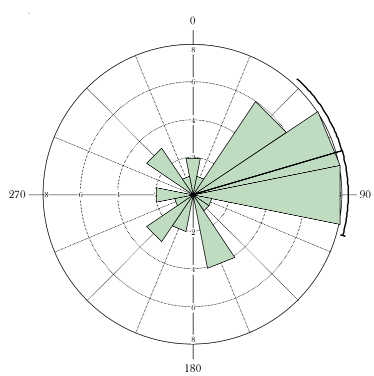

Slab 3

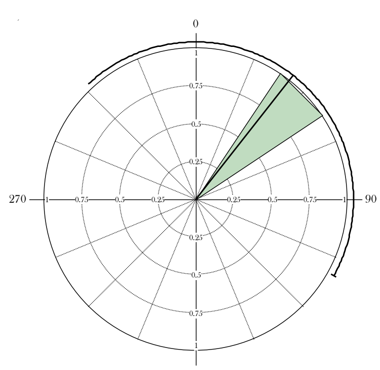

Uniaxial

Slab 4

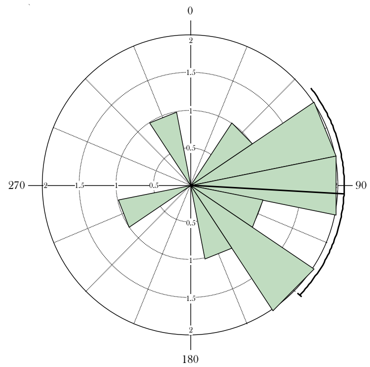

All Slabs

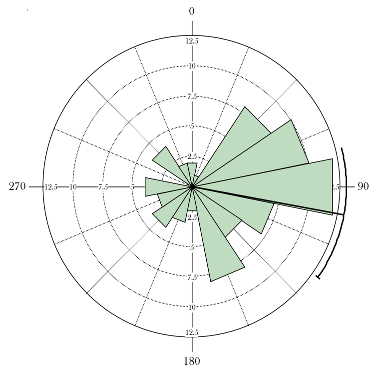

Section F-3: Site 3

Slab 2

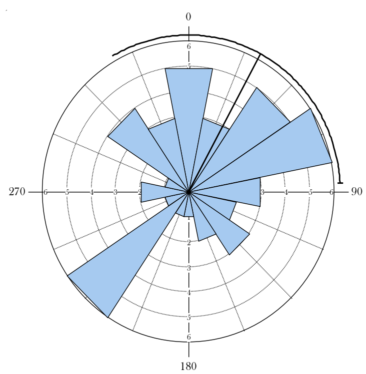

Slab 3

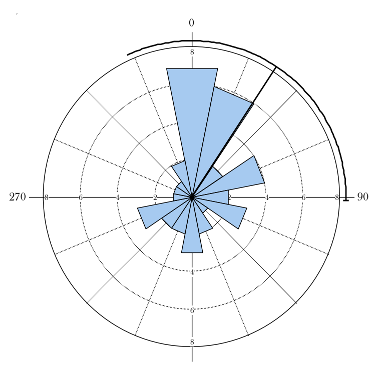

Uniaxial

Slab 4

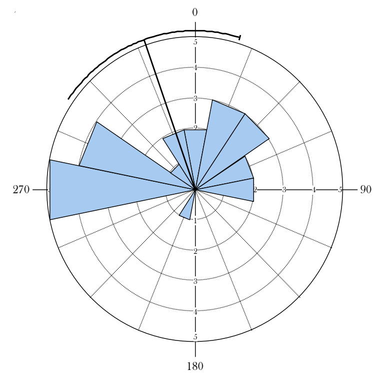

All Slabs

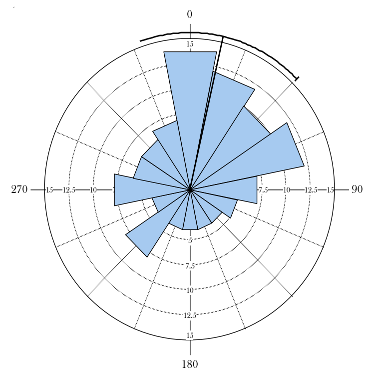

Section F-4: Site 5

Slab 2

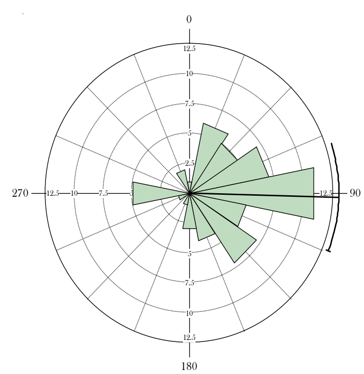

Slab 3

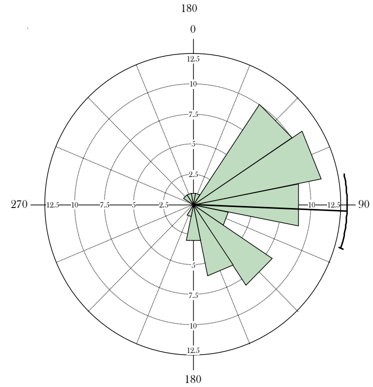

Uniaxial

Slab 4

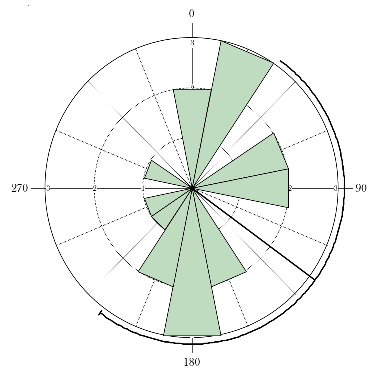

All Slabs

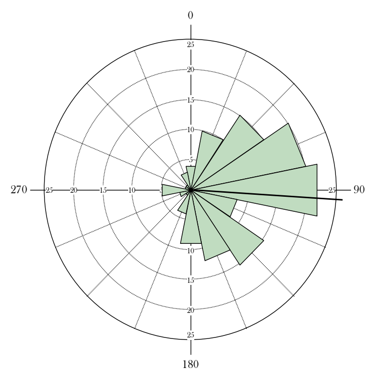

Section F-5: Site 6

Slab 2

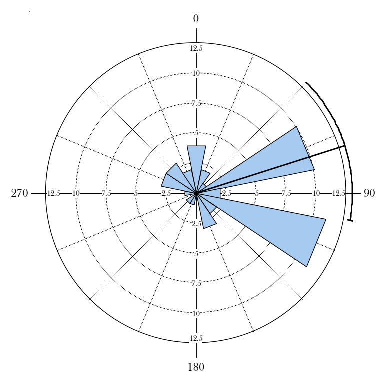

Slab 3

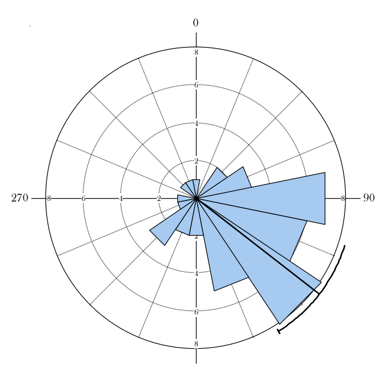

Uniaxial

Slab 4

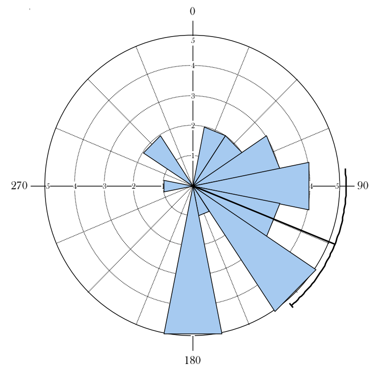

All Slabs

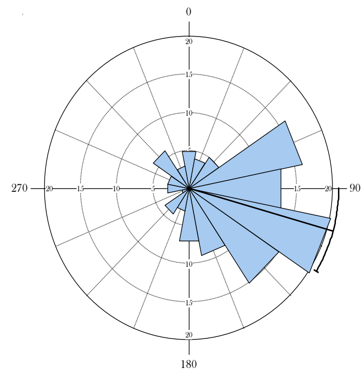

Section F-6: Site 12

Slab 2

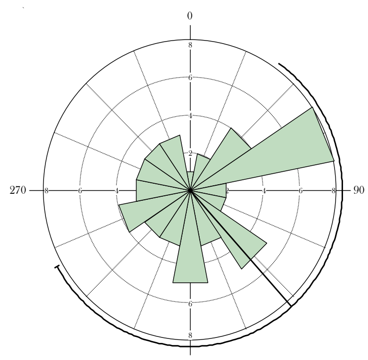

Slab 3

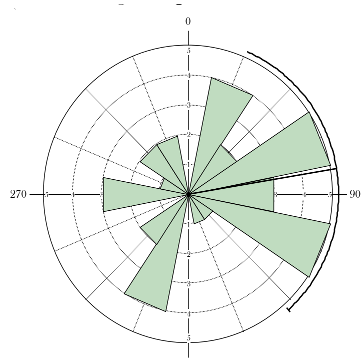

Uniaxial

Slab 4

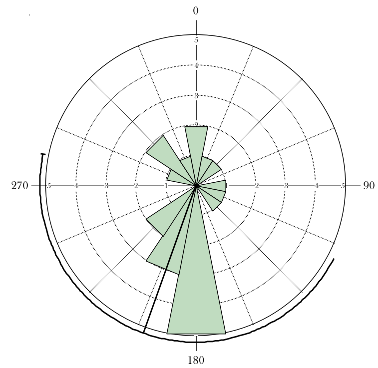

All Slabs

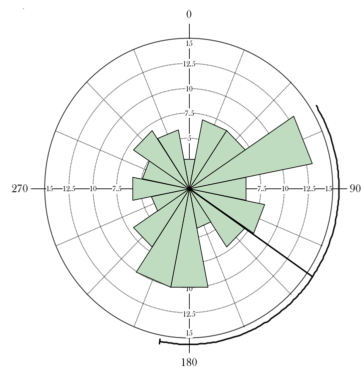

Section F-7: Site 13

Slab 2

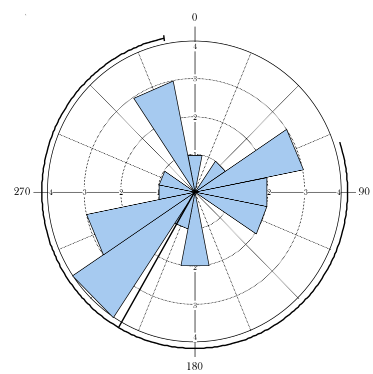

Slab 3

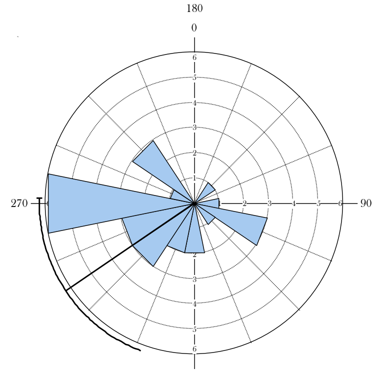

Uniaxial

Slab 4

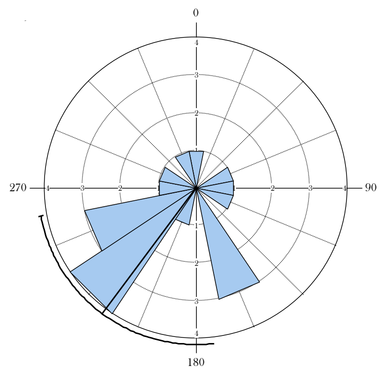

All Slabs

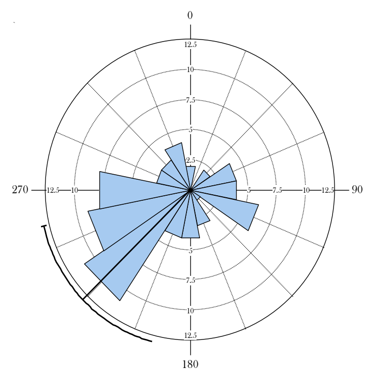

Section F-8: Site 14

Slab 2

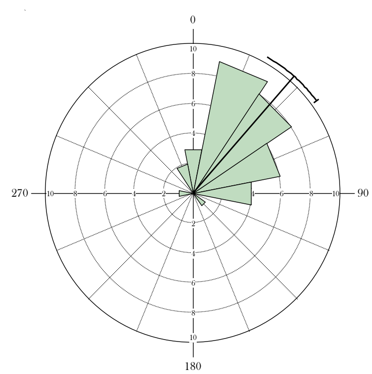

Slab 3

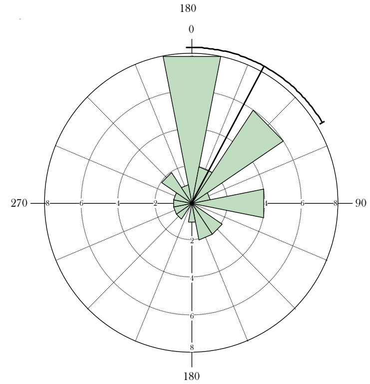

Uniaxial

Slab 4

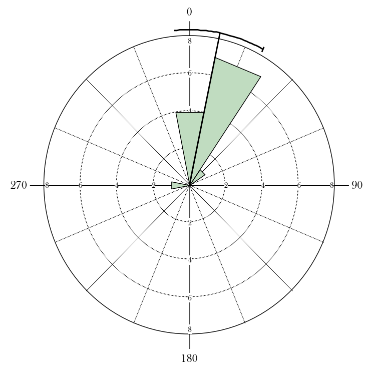

All Slab

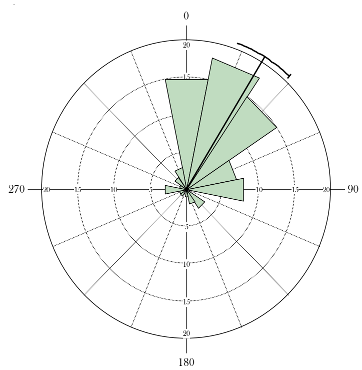

APPENDIX G: SENSOR RESULTS

Table G - 1: **Summary of acoustic emission hits.** This table sums all recorded hits per day. This was done daily for each individual AE sensor ("channel" or "ch") as well as totaled for all sensors ("SumOfall").

Date Value	SumOfch1	SumOfch2	SumOfch3	SumOfch4	SumOfch5	SumOfch6	SumOfall
04-Oct-14	17	230	1132	1354	123	126	2982
05-Oct-14	30	88	757	1087	79	85	2126
06-Oct-14	10	239	403	1045	39	52	1788
07-Oct-14	113	484	357	1369	115	90	2528
08-Oct-14	1076	1921	1421	3411	355	292	8476
09-Oct-14	41	106	306	1394	30	25	1902
10-Oct-14	25	22	251	1017	19	13	1347
11-Oct-14	59	24	155	879	34	14	1165
12-Oct-14	62	22	156	990	21	22	1273
13-Oct-14	2	9	158	8	2	8	187
14-Oct-14	1	9	139	4	8	8	169
15-Oct-14	27	28	50	24	9	1	139
16-Oct-14	0	0	43	3	3	4	53
17-Oct-14	3	8	487	18	16	23	555
18-Oct-14	7	72	1201	897	13	22	2212
19-Oct-14	7	24	825	751	13	20	1640
20-Oct-14	50	19	285	41	9	2	406
21-Oct-14	1	3	152	42	10	10	218
22-Oct-14	1	5	193	10	6	5	220
23-Oct-14	20	0	166	11	3	5	205
24-Oct-14	18	16	334	345	37	20	770
25-Oct-14	5546	23502	4624	4113	472	77	38334
26-Oct-14	14	15	136	73769	69	125	74128
27-Oct-14	9	1	24	587	25	4	650
28-Oct-14	1	0	66	39	6	11	123
29-Oct-14	0	0	54	42	4	8	108
30-Oct-14	0	0	41	10	6	6	63
31-Oct-14	25391	35928	20561	28291	2856	295	113322
01-Nov-14	87107	97244	61582	106705	15465	1236	369339
02-Nov-14	65	17	205	8851	8063	37	17238
03-Nov-14	7	6	205	10214	19468	11	29911
04-Nov-14	35	21	340	2777	4695	55	7923
05-Nov-14	16	1	125	376	18	60	596
06-Nov-14	7	1	94	254	8	6	370
07-Nov-14	1	2	80	193	1	7	284

08-Nov-14	0	1	78	139	6	1	225
09-Nov-14	12	0	6	4	1	135	158
10-Nov-14	3	1	59	82	4	133	282
11-Nov-14	8	0	18	28	8	6	68
12-Nov-14	4755	2479	3037	6477	879	5413	23040
13-Nov-14	20038	17561	10892	23020	2027	16743	90281
14-Nov-14	26	3570	40	2295	11	13	5955
15-Nov-14	25	8	9479	694	14	30	10250
16-Nov-14	545	3	1166	870	265	832	3681
17-Nov-14	2	1	207176	27	17	3	207226
18-Nov-14	0	0	183569	12	7	0	183588
19-Nov-14	4944	1212	7882	6720	1164	3172	25094
20-Nov-14	2371	625	51867	6052	454	1638	63007
21-Nov-14	39	5	67229	6300	6	15	73594
22-Nov-14	5261	25909	74719	16645	1348	7146	131028
23-Nov-14	30	73	18967	4558	27	1	23656
24-Nov-14	27	32	2332	784	4	54	3233
25-Nov-14	9	143	2508	732	3	3	3398
26-Nov-14	2	443	504	485	10	2	1446
27-Nov-14	1	71	1141	300	27	3	1543
28-Nov-14	0	114	859	176	20	52	1221
29-Nov-14	11694	20947	48225	55607	4869	15657	156999
30-Nov-14	4351	3184	21337	29201	2602	7734	68409
01-Dec-14	0	6789	107	5416	17	1	12330
02-Dec-14	4172	29403	27498	39237	3876	8987	113173
03-Dec-14	12124	82102	59104	96352	7916	17001	274600
04-Dec-14	2218	17711	10170	18276	1663	2793	52831
05-Dec-14	58	2493	1088	2314	124	252	6329
06-Dec-14	46	3251	1416	3235	212	327	8487
07-Dec-14	0	643	25	1022	38	5	1733
08-Dec-14	3	787	64	482	36	8	1380
09-Dec-14	95090	840	23	85	21	1	96060
10-Dec-14	19544	723	80	106	23	284	20760
11-Dec-14	2398	2248	25747	39200	3482	8145	81220
12-Dec-14	8422	4580	95605	145573	12893	18192	285265
13-Dec-14	121244	550	36	11543	9	4	133386
14-Dec-14	313775	331	44	8781	0	3	322934
15-Dec-14	148209	6687	10598	36643	1438	1657	205232
16-Dec-14	266309	14877	21960	73818	2851	3346	383161
17-Dec-14	733876	12333	17235	32408	2425	4149	802426
18-Dec-14	1492371	565	20	17725	5	0	1510686

19-Dec-14	1185862	8274	11808	10466	1704	683	1218797
20-Dec-14	1196905	6059	3712	9826	516	212	1217230
21-Dec-14	1978188	37	107	7885	35	0	1986252
22-Dec-14	2386139	2476	24	8470	29	0	2397138
23-Dec-14	42734	1102	22	98592	9	0	142459
24-Dec-14	227487	639	11143	204352	1042	362	445025
25-Dec-14	462959	253	99	112103	32	14	575460
26-Dec-14	316849	323	95	9232	74	4	326577
27-Dec-14	151963	603	59	0	5	1	152631
28-Dec-14	496400	7229	38	0	4624	34	508325
29-Dec-14	1092440	856	109	3	3184	2	1096594
30-Dec-14	734635	449	3327	43	933	1744	741131
31-Dec-14	8093	15861	139	0	15	2	24110
01-Jan-15	25551	1209	123	0	4	0	26887
02-Jan-15	379041	906	114	0	8	0	380069
03-Jan-15	6877	328	194	0	10	0	7409
04-Jan-15	4847	529	344	0	5	8	5733
05-Jan-15	18441	1498	257	0	30	0	20226
06-Jan-15	32102	1921	326	0	20	0	34369
07-Jan-15	26292	3514	208	0	14	0	30028
08-Jan-15	202606	5977	101	0	17	5	208706
09-Jan-15	192340	3955	80	0	4	0	196379
10-Jan-15	6667	4981	67	0	7	0	11722
11-Jan-15	1576	2861	37	0	3	0	4477
12-Jan-15	802	5489	27	0	5	1	6324
13-Jan-15	176310	10737	59	0	10	0	187116
14-Jan-15	1538086	25596	50	47	1	2	1563782
15-Jan-15	1047791	9974	33	155	2	0	1057955
16-Jan-15	1026541	79030	130	4	7	1	1105713
17-Jan-15	1024707	1122852	95	0	13	0	2147667
18-Jan-15	1751791	216585	26	0	3	0	1968405
19-Jan-15	818414	32	23	0	2	0	818471
20-Jan-15	1222192	1008	112	0	0	44	1223356
21-Jan-15	2480654	178255	86	0	11	0	2659006
22-Jan-15	1657244	32936	51	0	3	0	1690234
23-Jan-15	87151	75429	46	0	0	0	162626
24-Jan-15	300268	4217	45	0	0	1	304531
25-Jan-15	264943	228	68	0	1	13	265253
26-Jan-15	849776	145	22	0	0	22	849965
27-Jan-15	39	4365	1411	2	96	27	5940
28-Jan-15	12	27574	29	0	7	0	27622

29-Jan-15	5	408214	16	0	7	1	408243
30-Jan-15	10	26	22	0	42	0	100
31-Jan-15	29	6	23	0	8	0	66
01-Feb-15	5	30	19	0	8	0	62
02-Feb-15	6	13	34	0	7	0	60
03-Feb-15	17	12	21	0	4	0	54
04-Feb-15	70	306	31	0	3	1	411
05-Feb-15	188	143053	72	10	22	3	143348
06-Feb-15	7666	497273	46500	13680	3940	1468	570527
07-Feb-15	577	201823	8908	3745	615	86	215754
08-Feb-15	8577	477845	54050	11882	6064	2184	560602
09-Feb-15	10	851680	411	1	79	27	852208
10-Feb-15	0	1231575	59	1	25	120	1231780
11-Feb-15	0	270145	22	1	18	608	270794
12-Feb-15	0	284923	12	0	12	685	285632
13-Feb-15	0	260123	17	0	3	81	260224
14-Feb-15	0	66693	32	0	0	1646	68371
15-Feb-15	15298	222527	70	0	1	0	237896
16-Feb-15	5	167544	20	0	0	2	167571
17-Feb-15	10127	305955	34	0	0	1	316117
18-Feb-15	573165	406044	63	0	2	0	979274
19-Feb-15	511982	396021	37	0	0	0	908040
20-Feb-15	197197	510229	22	0	0	0	707448
21-Feb-15	32231	468319	33	0	0	272	500855
22-Feb-15	19007	159912	1924	12	217	198	181270
23-Feb-15	71601	41061	10	0	7	15	112694
24-Feb-15	491580	43030	36	0	1	1	534648
25-Feb-15	575155	52388	17	0	0	0	627560
26-Feb-15	257869	45754	31	0	1	4	303659
27-Feb-15	10157	113340	8664	530	1979	1880	136550
28-Feb-15	30904	333370	45163	1735	6584	4505	422261
01-Mar-15	63927	89005	15688	301	3543	2677	175141
02-Mar-15	353473	1292914	9337	68	1021	1171	1657984
03-Mar-15	26277	799039	18	0	12	4	825350
04-Mar-15	153610	210247	8	0	2	1	363868
05-Mar-15	493150	47995	289	839	24	0	542297
06-Mar-15	211414	2596	203	55	5	261	214534
07-Mar-15	650	0	16	0	3	0	669
08-Mar-15	1	0	19	0	4	0	24
09-Mar-15	147	0	21	0	2	0	170
10-Mar-15	417	0	77	0	7	0	501

11-Mar-15	935	0	3027	0	152	0	4114
12-Mar-15	3	0	22	0	28	0	53
13-Mar-15	5	0	45	0	21	0	71
14-Mar-15	8	0	36	0	1	0	45
15-Mar-15	69	0	57	0	23	0	149
16-Mar-15	0	0	53	0	46	0	99
17-Mar-15	2	0	8	0	136	0	146
18-Mar-15	3	0	43	0	104	0	150
19-Mar-15	7	0	25	0	756	0	788
20-Mar-15	3	0	21	0	578	0	602
21-Mar-15	7	0	107	0	896	0	1010
22-Mar-15	19402	0	8006	0	7747	0	35155
23-Mar-15	14599	0	687	0	153	0	15439
24-Mar-15	9773	0	28	0	221	0	10022
25-Mar-15	14461	0	16	0	89	0	14566

Table G - 2: **Summary of temperature readings.** These are the recorded average, maximum and minimum temperatures from the surface of Twain Harte Rock, in Farenheit.

DateValue	AvgOfTemp, °F (LGR S/N: 10012381, SEN S/N: 10012381)	MaxOfTemp, °F (LGR S/N: 10012381, SEN S/N: 10012381)	MinOfTemp, °F (LGR S/N: 10012381, SEN S/N: 10012381)
04-Oct-14	71.03135889	107.47	50.113
05-Oct-14	71.32472569	108.108	51.523
06-Oct-14	71.24098611	107.258	51.874
07-Oct-14	70.44694792	105.161	52.75
08-Oct-14	70.13122569	105.161	50.819
09-Oct-14	66.82523264	99.687	49.404
10-Oct-14	66.36887847	99.687	48.339
11-Oct-14	66.71703472	99.093	49.404
12-Oct-14	66.14577083	98.699	48.695
13-Oct-14	68.31644097	103.512	49.937
14-Oct-14	67.74668403	99.885	50.819
15-Oct-14	60.18759722	86.459	49.228
16-Oct-14	60.19995139	89.938	45.828
17-Oct-14	53.86634272	81.975	45.648
18-Oct-14	59.23335069	92.174	42.363
19-Oct-14	60.81601389	92.926	44.195
20-Oct-14	59.90078819	87.186	44.742
21-Oct-14	56.43151736	85.554	41.81
22-Oct-14	47.76034921	75.484	42.179

23-Oct-14	49.44059146	74.446	45.286
24-Oct-14	58.68171362	93.873	43.466
25-Oct-14	51.95616319	81.266	42.732
26-Oct-14	51.48366899	81.09	38.44
27-Oct-14	40.47263415	41.994	39.573
28-Oct-14			
29-Oct-14	54.40188235	81.442	47.088
30-Oct-14	45.35568493	46.908	44.379
31-Oct-14			
01-Nov-14	46.24534028	73.062	36.145
02-Nov-14	45.90041522	73.926	31.617
03-Nov-14	45.08605014	76.354	31.012
04-Nov-14	50.96120198	80.735	35.951
05-Nov-14	54.53820486	86.459	39.573
06-Nov-14	56.74580903	90.124	43.282
07-Nov-14	56.88991667	89.938	42.179
08-Nov-14	57.56501736	90.124	42.732
09-Nov-14	57.61921875	90.495	44.013
10-Nov-14	55.19547687	86.823	41.625
11-Nov-14	53.34552778	78.975	40.134
12-Nov-14	50.28561905	50.466	50.113
13-Nov-14	49.3005969	60.883	44.013
14-Nov-14	49.71778125	75.659	39.573
15-Nov-14	47.29268056	78.274	36.531
16-Nov-14	44.35735088	76.181	30.198
17-Nov-14	35.24671739	47.982	31.213
18-Nov-14	39.62724138	61.227	32.418
19-Nov-14	46.32620486	58.993	37.87
20-Nov-14	43.03679514	55.364	35.175
21-Nov-14	45.32976573	68.248	33.013
22-Nov-14	46.62926042	56.577	38.25
23-Nov-14	41.47895486	60.195	33.411
24-Nov-14	43.999875	75.139	31.816
25-Nov-14	47.28973611	80.911	34.002
26-Nov-14	51.30087153	86.277	37.297
27-Nov-14	53.20094444	88.833	40.509
28-Nov-14	50.07963889	84.654	37.297
29-Nov-14	43.24052778	47.266	39.573
30-Nov-14	42.91071528	50.819	37.87
01-Dec-14	48.58590625	77.749	38.818
02-Dec-14	46.67986806	50.995	39.76

03-Dec-14	49.81712153	57.785	48.16
04-Dec-14	50.27237778	65.167	41.994
05-Dec-14	48.46661111	56.057	41.439
06-Dec-14	50.63222222	74.098	41.625
07-Dec-14	46.31144097	64.481	38.25
08-Dec-14	46.64557986	75.139	36.338
09-Dec-14	46.39028819	69.964	38.25
10-Dec-14	47.39092708	67.735	38.818
11-Dec-14	49.98422028	54.322	43.648
12-Dec-14	41.67354514	45.466	35.951
13-Dec-14	39.92184028	63.968	32.218
14-Dec-14	38.37313889	57.441	31.816
15-Dec-14	41.52336806	53.1	36.338
16-Dec-14	45.14200694	69.278	39.76
17-Dec-14	41.28889236	48.517	37.107
18-Dec-14	41.88557986	63.282	33.411
19-Dec-14	40.90094792	44.922	36.531
20-Dec-14	45.09720139	49.582	41.994
21-Dec-14	50.18400694	67.392	41.994
22-Dec-14	47.5473871	73.58	37.679
23-Dec-14	45.99414236	69.449	35.564
24-Dec-14	41.92760764	51.874	34.002
25-Dec-14	36.50815278	56.923	27.93
26-Dec-14	34.21640278	55.884	24.96
27-Dec-14	35.45186111	58.131	25.819
28-Dec-14	37.44510764	61.569	28.555
29-Dec-14	37.12851042	59.68	26.245
30-Dec-14	35.43079167	53.1	22.552
31-Dec-14	31.79396875	58.476	20.529
01-Jan-15	32.54301042	57.614	21.209
02-Jan-15	34.11500694	59.68	24.093
03-Jan-15	36.53902778	61.741	26.245
04-Jan-15	40.48197222	67.906	28.969
05-Jan-15	43.93677431	72.372	33.411
06-Jan-15	47.57782292	76.876	36.531
07-Jan-15	49.37539583	79.678	37.87
08-Jan-15	47.51553472	77.05	37.107
09-Jan-15	48.28097569	62.769	41.994
10-Jan-15	49.17622917	73.407	39.76
11-Jan-15	46.88980556	68.934	37.107
12-Jan-15	45.44948958	68.592	35.564

13-Jan-15	41.64283681	68.421	30.607
14-Jan-15	43.11523843	69.793	30.808
15-Jan-15	44.49689931	72.545	30.403
16-Jan-15	46.66952431	68.763	33.607
17-Jan-15	49.67701736	78.624	39.573
18-Jan-15	50.24759028	79.151	38.44
19-Jan-15	50.15909375	77.05	39.007
20-Jan-15	45.36989583	72.028	33.411
21-Jan-15	43.29688889	71.168	29.174
22-Jan-15	44.03010417	72.891	32.617
23-Jan-15	46.35638889	75.312	32.815
24-Jan-15	47.90380903	78.098	33.213
25-Jan-15	51.33057986	84.474	36.145
26-Jan-15	48.98417361	82.864	37.87
27-Jan-15	46.65725	57.441	37.107
28-Jan-15	46.54218403	72.372	34.394
29-Jan-15	48.27638889	77.05	35.37
30-Jan-15	47.41577778	75.832	34.002
31-Jan-15	48.48930556	80.735	34.198
01-Feb-15	47.27273958	81.797	31.816
02-Feb-15	50.53851042	80.911	36.723
03-Feb-15	52.32549434	83.757	39.573
04-Feb-15	52.81042708	86.823	38.818
05-Feb-15	55.36363194	79.502	40.696
06-Feb-15	53.41841667	65.167	45.104
07-Feb-15	51.97539931	61.741	46.908
08-Feb-15	50.50413542	59.68	45.104
09-Feb-15	51.37840278	77.225	36.914
10-Feb-15	45.617	78.098	29.79
11-Feb-15	50.63655208	82.864	35.564
12-Feb-15	54.81457986	87.552	38.25
13-Feb-15	56.44996528	93.115	39.007
14-Feb-15	57.78726389	93.873	41.439
15-Feb-15	54.87874653	86.641	39.196
16-Feb-15	56.3705625	88.65	39.573
17-Feb-15	56.17170139	88.65	40.696
18-Feb-15	56.20250694	86.459	40.881
19-Feb-15	55.3345625	85.915	41.625
20-Feb-15	54.20032986	83.399	38.44
21-Feb-15	51.14736806	80.206	38.061
22-Feb-15	44.24889931	67.564	33.013

23-Feb-15	44.48880556	70.137	30.808
24-Feb-15	45.17508364	77.05	27.721
25-Feb-15	47.46335069	79.151	30.808
26-Feb-15	49.434375	78.975	33.607
27-Feb-15	45.86680903	64.652	38.061
28-Feb-15	41.82968403	66.022	33.213
01-Mar-15	43.39009028	72.199	30.607
02-Mar-15	43.71165278	74.098	33.411
03-Mar-15	43.83642361	74.964	30.198
04-Mar-15	45.54635417	77.923	29.995
05-Mar-15	51.15684698	87.552	32.018
06-Mar-15	51.3000669	87.186	31.213
07-Mar-15	55.23453125	89.755	36.145
08-Mar-15	57.45507639	89.384	39.384
09-Mar-15	57.73603819	90.68	38.25
10-Mar-15	58.67711111	90.68	40.509
11-Mar-15	52.74835764	75.312	43.466
12-Mar-15	56.44785764	89.017	38.44
13-Mar-15	61.72442014	96.748	41.067
14-Mar-15	64.39200694	97.916	46.908
15-Mar-15	65.36285764	95.4	49.937
16-Mar-15	61.335375	91.8	46.728
17-Mar-15	62.01815972	90.68	47.802
18-Mar-15	60.17121528	91.425	41.254
19-Mar-15	60.8413125	96.168	39.196
20-Mar-15	58.88536806	94.062	42.915
21-Mar-15	59.15528125	91.053	41.81
22-Mar-15	59.19770833	88.282	44.195
23-Mar-15	56.31105556	84.654	44.56
24-Mar-15	55.18661111	85.735	39.76
25-Mar-15	51.58316084	82.864	39.384

Table G - 3: **Summary of incoming light results.** Includes the average, maximum, and minimum daily light intensity.

DateValue	AvgOfIntensity, lum/ft² (LGR S/N: 10012381, SEN S/N: 10012381)	MaxOfIntensity, lum/ft² (LGR S/N: 10012381, SEN S/N: 10012381)	MinOfIntensity, lum/ft² (LGR S/N: 10012381, SEN S/N: 10012381)
04-Oct-14	4371.585366	18432	0
05-Oct-14	4287.284722	18432	0
06-Oct-14	4206.90625	17408	0
07-Oct-14	4076.614583	17408	0
08-Oct-14	4156.1875	17408	0
09-Oct-14	4111.21875	17408	0
10-Oct-14	4021.78125	17408	0
11-Oct-14	3741.715278	16384	0
12-Oct-14	3994.652778	17408	0
13-Oct-14	3928.076389	16384	0
14-Oct-14	3793.756944	16384	0
15-Oct-14	2129.0625	18432	0
16-Oct-14	3333.229167	17408	0
17-Oct-14	928.8685446	10752	0
18-Oct-14	3594.267361	15872	0
19-Oct-14	3525.944444	15872	0
20-Oct-14	3367.461806	14848	0
21-Oct-14	3358.197917	15360	0
22-Oct-14	149.8518519	2048	0
23-Oct-14	30.12804878	1152	0
24-Oct-14	1650.746479	14336	0
25-Oct-14	1556.489583	16384	0
26-Oct-14	3173.275261	15360	0
27-Oct-14	8.573170732	184	0
28-Oct-14			
29-Oct-14	176.3823529	3840	0
30-Oct-14	0	0	0
31-Oct-14			
01-Nov-14	2103.427083	18432	0
02-Nov-14	3114.785467	13824	0
03-Nov-14	2381.470752	13824	0
04-Nov-14	2940.312871	13312	0
05-Nov-14	2877.9375	13312	0
06-Nov-14	2303.065972	14848	0
07-Nov-14	2822.934028	13312	0
08-Nov-14	2693.756944	13312	0

09-Nov-14	2735.052083	12800	0
10-Nov-14	2619.47331	12800	0
11-Nov-14	1052.572917	6400	0
12-Nov-14	0	0	0
13-Nov-14	382.6627907	3840	0
14-Nov-14	1135.927083	8192	0
15-Nov-14	1175.611111	7936	0
16-Nov-14	1140.34386	7936	0
17-Nov-14	29.42934783	2816	0
18-Nov-14	78.57635468	1664	0
19-Nov-14	516.3333333	3072	0
20-Nov-14	594.65625	3712	0
21-Nov-14	2015.125874	21504	0
22-Nov-14	424.0451389	3840	0
23-Nov-14	975.4444444	7936	0
24-Nov-14	1454.552083	7168	0
25-Nov-14	1411.788194	6912	0
26-Nov-14	1417.364583	6912	0
27-Nov-14	1444.621528	8192	0
28-Nov-14	1331.357639	7168	0
29-Nov-14	271.6944444	2432	0
30-Nov-14	394.3194444	3584	0
01-Dec-14	1177.864583	8704	0
02-Dec-14	289.1666667	3968	0
03-Dec-14	272.3368056	4096	0
04-Dec-14	726.562963	8704	0
05-Dec-14	554.15625	3840	0
06-Dec-14	1049.065972	6144	0
07-Dec-14	892.4965278	5888	0
08-Dec-14	1150.03125	6912	0
09-Dec-14	798.5833333	6144	0
10-Dec-14	751.7534722	6656	0
11-Dec-14	66.54545455	480	0
12-Dec-14	412.6909722	2688	0
13-Dec-14	687.6909722	7680	0
14-Dec-14	681.7673611	6656	0
15-Dec-14	416.9097222	3584	0
16-Dec-14	925.2708333	7936	0
17-Dec-14	519.5694444	3840	0
18-Dec-14	1007.520833	6144	0
19-Dec-14	241.6701389	1536	0

20-Dec-14	234.2569444	1920	0
21-Dec-14	599.4340278	3712	0
22-Dec-14	729.0645161	3200	0
23-Dec-14	1100.243056	7680	0
24-Dec-14	455.4652778	3456	0
25-Dec-14	1201.034722	6656	0
26-Dec-14	1189.857639	6656	0
27-Dec-14	1215.0625	6656	0
28-Dec-14	1197.767361	6656	0
29-Dec-14	1196.128472	6912	0
30-Dec-14	1288.159722	6912	0
31-Dec-14	1256.357639	6912	0
01-Jan-15	1245.934028	6912	0
02-Jan-15	1243.979167	6912	0
03-Jan-15	1225.736111	6656	0
04-Jan-15	1276.572917	8704	0
05-Jan-15	1195.069444	7680	0
06-Jan-15	1262.170139	6912	0
07-Jan-15	1287.631944	6912	0
08-Jan-15	1155.576389	7680	0
09-Jan-15	661.7916667	3968	0
10-Jan-15	1263.291667	7936	0
11-Jan-15	1272.055556	6656	0
12-Jan-15	1253.038194	7680	0
13-Jan-15	1323.993056	7168	0
14-Jan-15	2848.427046	12800	0
15-Jan-15	2799.125	13312	0
16-Jan-15	1056.868056	8192	0
17-Jan-15	2021.381944	15872	0
18-Jan-15	2918.725694	15360	0
19-Jan-15	3051.434028	13824	0
20-Jan-15	2727.225694	15360	0
21-Jan-15	3070.517361	14848	0
22-Jan-15	1710.576389	14848	0
23-Jan-15	3244.90625	14336	0
24-Jan-15	3327.829861	14848	0
25-Jan-15	3327.21875	14848	0
26-Jan-15	1683.548611	16384	0
27-Jan-15	801.7777778	4608	0
28-Jan-15	3156.069444	14848	0
29-Jan-15	2929.309028	16384	0

30-Jan-15	3433.069444	14848	0
31-Jan-15	3565.069444	15872	0
01-Feb-15	2977.326389	16384	0
02-Feb-15	2762.982639	16384	0
03-Feb-15	3168.064151	15872	0
04-Feb-15	2680.256944	17408	0
05-Feb-15	2055.340278	16384	0
06-Feb-15	366.0173611	3456	0
07-Feb-15	563.0555556	9728	0
08-Feb-15	426.1284722	5376	0
09-Feb-15	3495.333333	23552	0
10-Feb-15	3863.975694	21504	0
11-Feb-15	3959.6875	19456	0
12-Feb-15	4553.958333	19456	0
13-Feb-15	4529.3125	19456	0
14-Feb-15	4645.708333	19456	0
15-Feb-15	3873	19456	0
16-Feb-15	4669.458333	19456	0
17-Feb-15	4629.125	19456	0
18-Feb-15	4605.25	19456	0
19-Feb-15	4092.361111	21504	0
20-Feb-15	4754.836806	19456	0
21-Feb-15	4548.3125	18432	0
22-Feb-15	1872.461806	25600	0
23-Feb-15	3311.149306	25600	0
24-Feb-15	5099.676364	20480	0
25-Feb-15	2363.21875	11776	0
26-Feb-15	2296.145833	12288	0
27-Feb-15	1058.642361	16384	0
28-Feb-15	1247.989583	14336	0
01-Mar-15	2256.940972	16384	0
02-Mar-15	1751.590278	18432	0
03-Mar-15	2233.871528	17408	0
04-Mar-15	2608.868056	15360	0
05-Mar-15	3249.017794	14848	0
06-Mar-15	2503.492958	11264	0
07-Mar-15	2845.173611	11776	0
08-Mar-15	2800.993056	12800	0
09-Mar-15	2936.104167	12288	0
10-Mar-15	2275.743056	12288	0
11-Mar-15	895.6631944	9216	0

12-Mar-15	3000.489583	12800	0
13-Mar-15	3028.111111	14848	0
14-Mar-15	2608.645833	13824	0
15-Mar-15	2776.645833	12800	0
16-Mar-15	2349.194444	13824	0
17-Mar-15	2718.201389	14336	0
18-Mar-15	3320.107639	13312	0
19-Mar-15	3373.354167	13824	0
20-Mar-15	2410.881944	12288	0
21-Mar-15	3165.017361	14336	0
22-Mar-15	3090.371528	14336	0
23-Mar-15	2592.472222	16384	0
24-Mar-15	2519.489583	13312	0
25-Mar-15	3039.412587	12800	0

APPENDIX H: WEATHERING INDEX MORPHOLOGY

ID	MORPHOLOGY
0 fresh crack, no signs of oxidation or weathering, extremely sharp edges and evidence of recent detachment	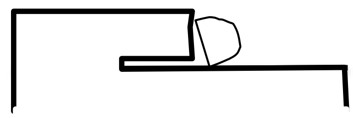
1 fresh crack with less than 50% of the face oxidized	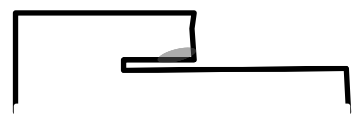
2 fresh crack with greater than 50% of the face oxidized	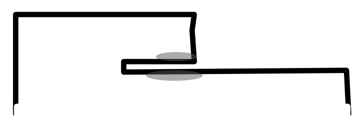
3 sharp-edged crack, fully oxidized	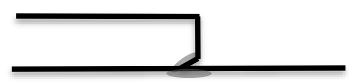
4 round-edged crack, fully oxidized	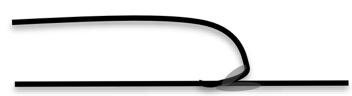
5 round-edged crack, sealed	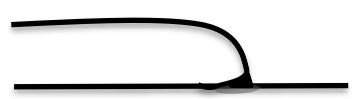
6 no void present, obvious paleo-crack location	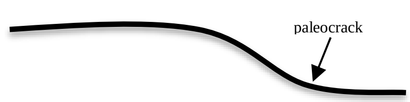

APPENDIX I: UNITLESS CRACK DENSITY RESULTS

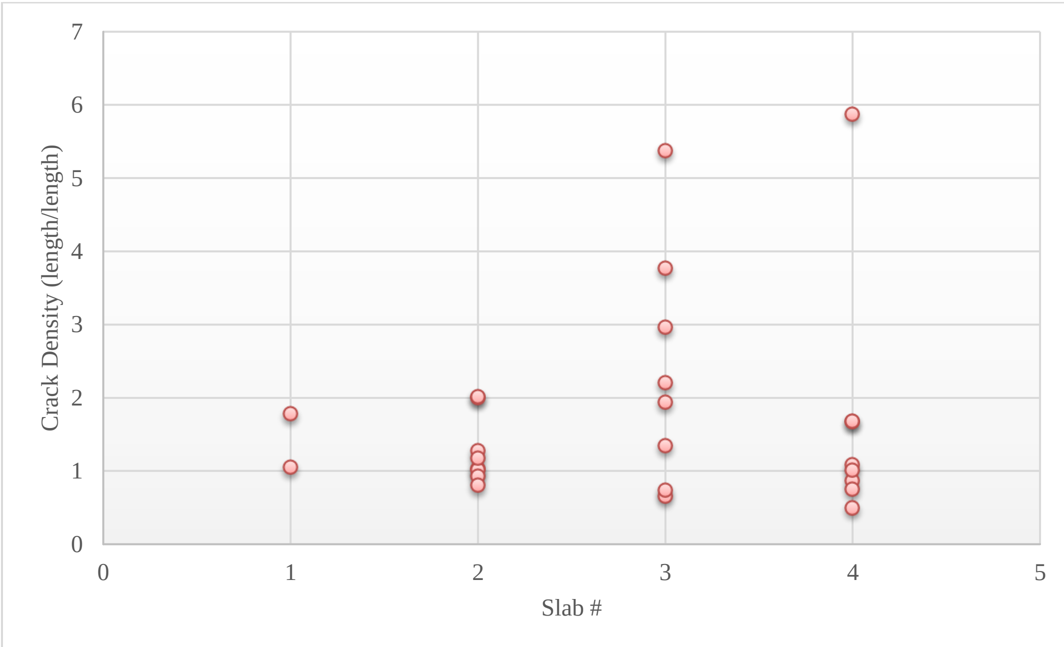

APPENDIX J: ADJUSTED TWAIN HARTE CLIMATE GRAPH

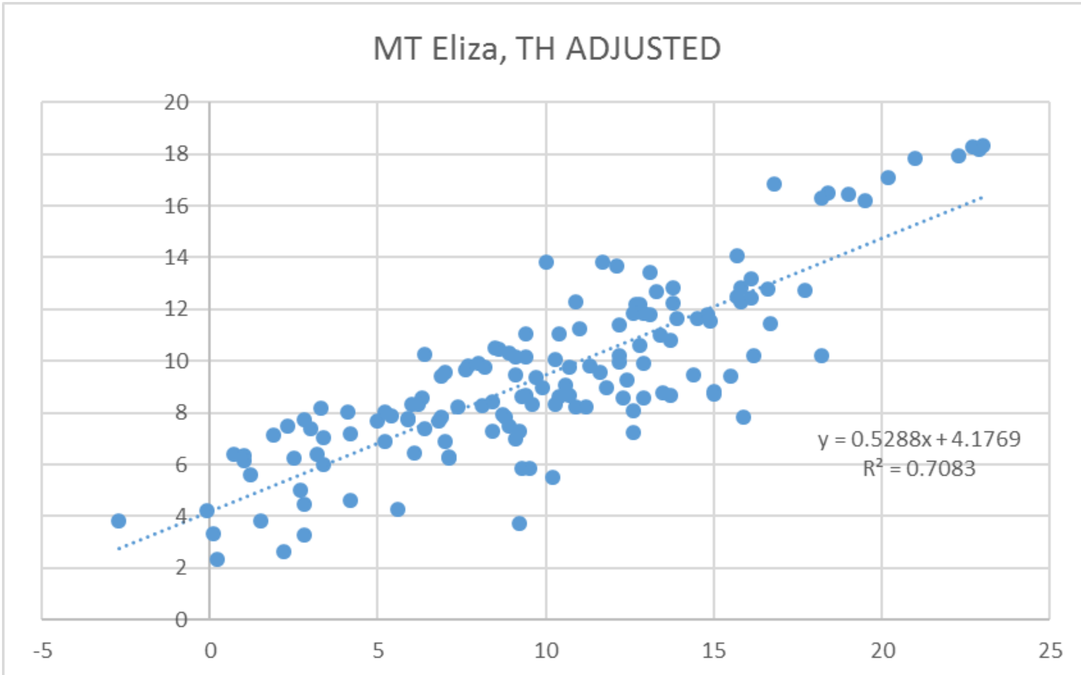

APPENDIX K: TRANSECT SURFACE SLOPES

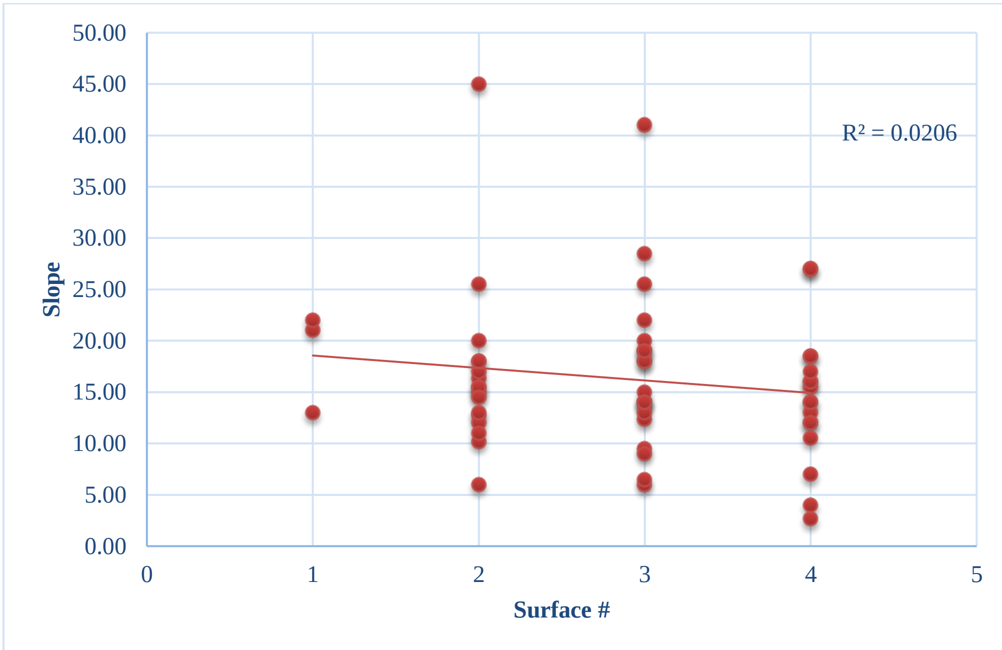

APPENDIX L: TRANSECT BEARINGS

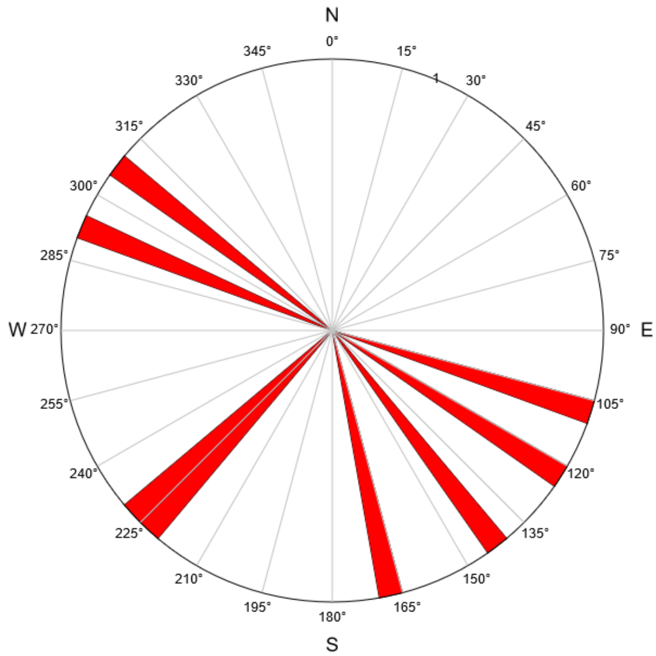

Figure L - 1: **Surface 2 Transect Bearings**

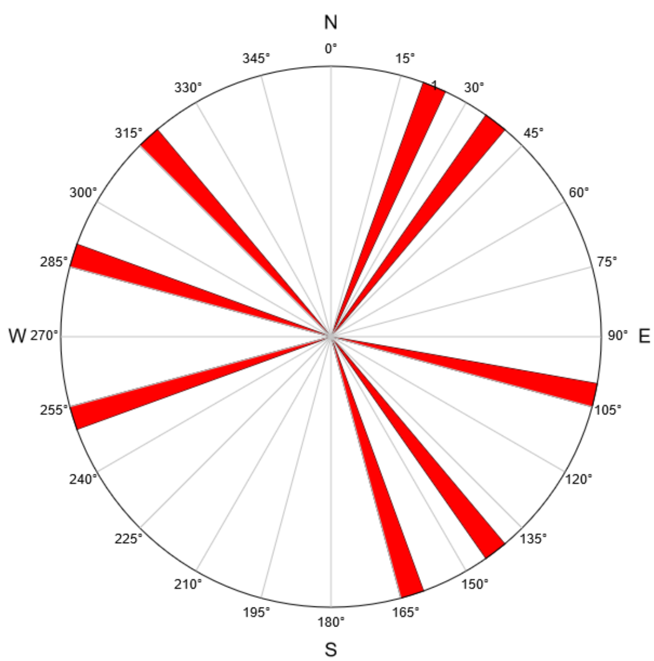

Figure L - 2: **Surface 3 Transect Bearings**

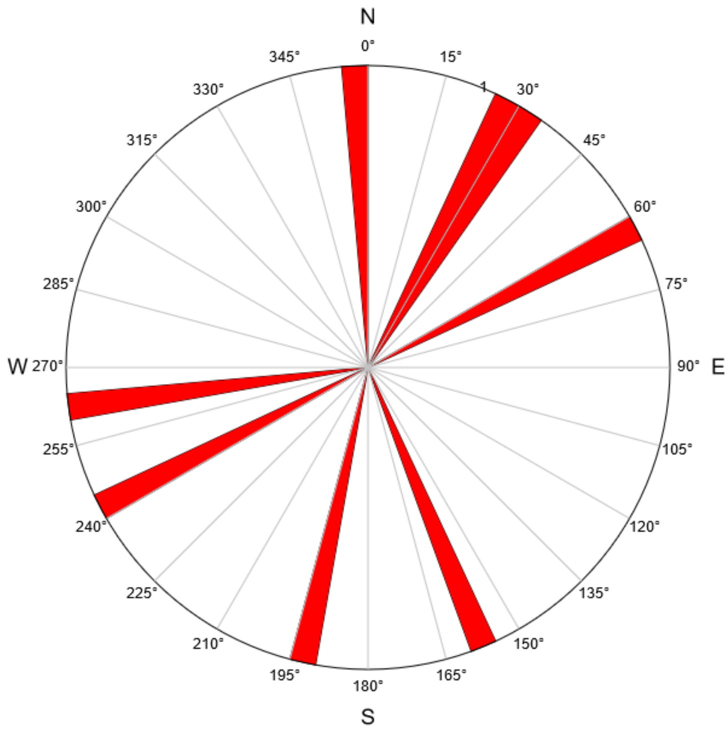

Figure L - 3: **Surface 4 Transect Bearings**